



The
University
Of
Sheffield.

Access to Electronic Thesis

Author: Kambiz Kalantari
Thesis title: Ti doped Bi_{1-x}NdxFeO₃ ceramics
Qualification: PhD

This electronic thesis is protected by the Copyright, Designs and Patents Act 1988. No reproduction is permitted without consent of the author. It is also protected by the Creative Commons Licence allowing Attributions-Non-commercial-No derivatives.

If this electronic thesis has been edited by the author it will be indicated as such on the title page and in the text.



Department of Material Science and Engineering
University of Sheffield

Ti doped $\text{Bi}_{1-x}\text{Nd}_x\text{FeO}_3$

A thesis submitted for the degree of
Doctor of Philosophy by

Kambiz Kalantari

Supervisors:

Prof. I. M. Reaney

Prof. D.C. Sinclair

Feb 2012

*They smell your mouth
to find out if you have told someone:
I love you
They smell your heart*

*Such a strange time it is, my dear;
And they punish Love
at thoroughfares
By flogging.*

*We must hide our Love in dark closets.
In this crooked dead end of a bitter cold
They keep their fire alive
By burning our songs and poems;
Do not place your life in peril by your thoughts!
Such a strange time it is, my dear!
He who knocks on your door in the middle of the night,
His mission is to break your Lamp!
We must hide our Lights in dark closets!
Behold! butchers are on guard at thoroughfares
With their bloodstained cleavers and chopping-boards;
Such a strange time it is, my dear!
They cut off the smiles from lips,
and the songs from throats!
We must hide our Emotions in dark closets!
They barbecue canaries
on a fire of jasmines and lilacs!
Such a strange time it is, my dear!
Intoxicated by victory,
Satan is enjoying a feast at our mourning table!
-Ahmad Shamloo-*

تقدیم به پدر و مادر عزیزتر از جانم

Publications from this Thesis:

Published:

Ti doping to reduce conductivity in $Bi_{0.85}Nd_{0.15}FeO_3$ ceramics , K. Kalantari, I. Sterianou, S. Karimi, M.C. Ferrarelli, S. Miao, D.C. Sinclair, and I.M. Reaney, , **2011**, Adv. Funct. Mater. 21, 3737.

In press:

Structural phase transitions in Ti-doped $Bi_{1-x}Nd_xFeO_3$ ceramics K. Kalantari, I. Sterianou, D. C. Sinclair, P.A. Bingham, J. Pokorný and I.M. Reaney, J. Appl. Phys.

In preparation:

The 3-dimensional atomic structure of unique nanoscale rod-shaped precipitates in neodymium and titanium codoped bismuth ferrite, I.MacLaren, L.Wang, B. Schaffer, Q.M. Ramasse, A.J. Craven, L. Houben, S. Miao, K. Kalantari, I. M. Reaney , for submission to Nature.

Defect chemistry of Ti-doped $Bi_{1-x}Nd_xFeO_3$, I.M. Reaney, I. Maclaren, S. Karimi, K. Kalantari, I. Sterianou and D.C. Sinclair, for submission to APL

AFE-FE switching in Ti doped $Bi_{0.825}Nd_{0.175}FeO_3$ thin films, K. Kalantari, D. Marincel, S.T. McKinstry, I.M. Reaney, for submission to APL

Acknowledgment

I would like to take this opportunity to express my sincerest gratitude to my Ph.D. research supervisor, Prof. I. M. Reaney, for his guidance, invaluable support, and encouragement during the course of this work. I was benefited by his profound insight, experience, and scientific thinking.

I would also like to express my deep gratitude for the continuous support and academic suggestion by my advisor, Prof. D. C. Sinclair, throughout this research.

Throughout this work, I am very fortunate in having opportunities to work with many great people. I would like to especially thank Dr. I. Sterianou for her insightful advice and a lot of support in this study and guidance in experiment. And of course, I would like to thank all members in our group for working and drinking hard together.

Most of all I would like to thank people who take care of me, my parents. I would never finish this study without their encouragement and full support. I owe everything I have and everything I have become to my family whose love and support cannot be overstated.

Finally, I would like to thank the EPSRC for funding and all those not explicitly mentioned who have helped in any way towards this thesis.

Summary

Bismuth ferrite (BiFeO_3) is an inorganic chemical compound with a distorted rhombohedral (R3c) perovskite structure. It is a base for promising PbO-free piezoelectric and ferroelectric materials and also exhibits multiferroic properties at room temperature. However, the major drawback of the material is its high leakage current particularly under high electric field. It is postulated that the high leakage currents arise from the presence of oxygen vacancies, V_{O} formed by the reduction of Fe^{3+} to Fe^{2+} during sintering.

Recently, RE doping has been shown by Karimi *et al.* (2009) to induce a transition from a ferroelectric (FE) to antiferroelectric (AFE) structure similar in character to that observed in $\text{Pb}(\text{Zr},\text{Ti})\text{O}_3$ (PZT). The main goal of this work therefore, was to fabricate compositions in the solid solution $\text{Bi}_{1-x}\text{Nd}_x\text{FeO}_3$ but additionally utilise Ti^{4+} doping on the B-site to control conductivity with the intention of achieving greater understanding of the intrinsic ferroelectric and dielectric properties.

Initially, $\text{Bi}_{0.85}\text{Nd}_{0.15}\text{Fe}_y\text{Ti}_{1-y}\text{O}_3$ $0 \leq y \leq 0.1$ compositions were fabricated. For $y = 0$, a mixture of FE (R3c) and AFE (Pbam) phases were present in XRD spectra. For $0.01 \leq y \leq 0.03$, all XRD peaks could be indexed according to the PbZrO_3 (PZ)-like AFE phase. For higher values of y , the absence of unique PZ-like reflections and broad rather than split peaks in XRD spectra suggested that long range antipolar order was destroyed. The substitution of 1% Ti for Fe resulted in a large decrease in the room temperature bulk conductivity from $\sim 1 \text{ mS cm}^{-1}$ to $< 1 \text{ }\mu\text{S cm}^{-1}$ and a large increase in activation energy (E_a) for conduction from 0.29 eV to $> 1.0 \text{ eV}$. Increasing the Ti concentration further had little effect on either conductivity or E_a . As a result of the decrease in conductivity, large fields (5kV/cm) could be applied to ceramic samples

which resulted in linear dielectric behaviour typical for an AFE structure below the field required to switch to the FE state.

Subsequently, phase transitions as a function of Nd concentration were investigated in 3% Ti doped $\text{Bi}_{1-x}\text{Nd}_x\text{FeO}_3$ ceramics. Paraelectric (PE) to FE transitions were observed for compositions with $x \leq 0.125$ which manifested themselves as peaks in permittivity. In contrast, PE to AFE transitions for $0.15 \leq x \leq 0.20$ gave rise to a step-like change in the permittivity, with $x = 0.25$ exhibiting no sharp anomalies and remaining PE until room temperature. The large volume changes at the PE to FE/AFE transitions reported by Levin and co-workers [Phys. Rev. B, **81**, 020103 (2011)] were also observed by dilatometry. It is proposed that the large volume change coupled with their 1st order character constrains the transitions in Nd-doped BiFeO_3 to occur uniformly throughout the material in an avalanche-like manner. Hence, anomalies in DSC, permittivity and thermal expansion were observed over commensurately narrow temperature intervals. Despite the large volume change and eye-catching anomalies in DSC, the latent heats for the transitions in Ti-doped $\text{Bi}_{1-x}\text{Nd}_x\text{FeO}_3$ are similar to $\text{Pb}(\text{Zr},\text{Ti})\text{O}_3$ (1-3 kJ/mol) with each an order of magnitude greater than BaTiO_3 (~0.2 kJ/mol).

Thin films of $\text{Bi}_{0.825}\text{Nd}_{0.175}\text{Fe}_{0.97}\text{Ti}_{0.03}\text{O}_3$, which in bulk ceramic has the PZ-like structure, were deposited by Pulsed Laser Deposition on Pt/Si substrates in collaboration with the group of Professor Trolier-Mckinstry at Pennsylvania State University, PA, USA. Thin films deposited at 625 °C and 650 °C were predominantly PZ-like but contained regions composed of the R3c phase. Polarisation *vs.* field measurements revealed large coercive fields (~400 kV/cm) and high remanent polarisation (100 $\mu\text{C}/\text{cm}^2$) which are speculated to at least in part arise from AFE-FE switching in the system.

Contents

Acknowledgment	5
Summary	6
Contents	8
Chapter 1: Introduction	11
References	13
Chapter 2: Literature Review	15
2.1 Piezoelectric Materials	15
2.1.1. Discovery of Piezoelectric effect	15
2.1.2. Piezoelectricity	15
2.1.3. Commercial piezoceramics	17
2.2. Multiferroic materials	20
2.2.1. Ferromagnets	20
2.2.2. Ferroelectrics	22
2.2.3. Magnetoelectrics and multiferroics	28
2.3. Perovskites	29
2.3.1. Basic structure	29
2.3.2. Tolerance factor	30
2.3.3. Distorted perovskite structure	30
2.4. BiFeO₃ (Bismuth Ferrite)	36
2.4.1. Structure	36
2.4.2. Properties	37
2.4.3. Critical issues with BiFeO ₃	37
2.4.4. A-site Doped BiFeO ₃	38
2.4.5. B-site doped BiFeO ₃	43
2.5. Focus of the Current Project	48
References	49
Chapter 3: Experimental Procedures	56
3.1. Ceramic Processing	56
3.1.1. Calcination	56
3.1.2. Particle Size Analysis (PSA)	57
3.1.3. Pelletisation	57
3.1.4. Density Measurement	57
3.2. Structural and Microstructural Characterisation	60
3.2.1. X-Ray Diffraction (XRD)	60
3.2.2. Differential Scanning Calorimetry (DSC)	60
3.2.3. Dilatometry	60
3.2.4. Scanning Electron Microscopy (SEM)	61

3.2.5. Transmission Electron Microscopy (TEM)	61
3.2.6. Raman Spectroscopy	62
3.3 Electrical Characterisation	62
3.3.1. Dielectric Measurement	62
3.3.2. Impedance Spectroscopy (IS)	63
3.3.3. Polarisation- Electric Field Measurement	64
3.3.4. Piezoresponse Force Microscopy (PFM)	64
References	65
Chapter 4: Raw Materials and Processing	66
4.1. Raw materials characterisation	66
4.1.1. Bismuth (III) Oxide, Bi ₂ O ₃	66
4.1.2. Iron (III) Oxide, Fe ₂ O ₃	68
4.1.3. Neodymium Oxide, Nd ₂ O ₃	70
4.1.4. Titanium (IV) Oxide, TiO ₂	72
4.1.5. Particle size of Raw Materials	74
4.2. Powder processing	76
References	81
Chapter 5: Ti doped Bi_{0.85}Nd_{0.15}FeO₃ ceramics	82
5.1. Introduction	82
5.2. Structure and Microstructure	83
5.2.1. X-Ray Diffraction	83
5.2.2 Scanning Electron Microscopy (SEM)	85
5.2.3. Transmission Electron Microscopy (TEM)	88
5.3. Differential Scanning Calorimetry (DSC)	90
5.4. Electrical Properties	92
5.5. Conclusions	101
References	102
Chapter 6: Structural phase transitions in 3% Ti-doped Bi_{1-x}Nd_xFeO₃ ceramics	104
6.1. Introduction	104
6.2. X-ray diffraction	105
6.3. Microstructure	108
6.4. Raman Spectroscopy	112
6.5. Thermal Analysis	114
6.5.1. Differential Scanning Calorimetry (DSC)	114
6.5.2. Dilatometry	118
6.6. Electrical Measurements	121
6.7. Conclusions	129
References	130
Chapter 7: Bi_{0.825}Nd_{0.175}Fe_{0.97}Ti_{0.03}O₃ thin films: a preliminary investigation	134

7.1. Introduction	134
7.2. Pulsed Laser Deposition (PLD)	135
7.3. X-Ray Diffraction (XRD)	139
7.4. Raman Spectroscopy	139
7.5. Scanning Electron Microscopy (SEM)	144
7.6. Piezoresponse Force Microscopy	145
7.7. Ferroelectric Characterisation	147
7.8. Conclusions	149
References	150
Chapter 8: Conclusions	153
Chapter 9: Future Work	156
References	158

Chapter 1: Introduction

BiFeO_3 (BFO) is a PbO free, perovskite-structured material which is currently gaining attention due to its purported multiferroic applications. A general study of magnetoelectricity was first given in 1994 by Schmid [1]. Later Fiebig (2005) [2] and Eerenstein (2006) [3] remarked on the revival of study of the magnetoelectric effect generated by Ramesh and co-workers whose contribution in Nature [4] on BiFeO_3 (BFO) thin films suggested its potential for magnetoelectric devices and pointed out its large remanent polarization.

In many respects, BFO is the only clear candidate for a single phase material suitable for magnetoelectric devices, since it is the only system in which ferroelectric and antiferromagnetic order coexist above room temperature [5]. However, perversely the first applications of BFO will most likely make use, not of its magnetoelectric properties, but rather the large remanent polarisation, $100 \mu\text{C cm}^{-2}$, along the polar [111] direction. This is approximately twice that of PZT, the most widely used material in ferroelectric memories [6]. In addition, BFO is considered less toxic than PbO-based materials.

BFO is also being investigated as the base for PbO-free piezoelectric ceramics. Pure BFO has a small piezoelectric coefficient (d_{33}) but compositions close to the antiferroelectric/ferroelectric boundary in RE-doped BFO have shown a significant enhancement in d_{33} [7]. RE doping has the additional advantage of improving the phase purity, lowering T_C and engendering a weak ferromagnetic response [8]. However, in bulk ceramic form, BFO has not been commercially exploited for one critical reason: its high leakage current leads to poor quality hysteresis and strain field loops, particularly at lower frequencies.

The source of conductivity in BFO based ceramics is a point of controversy but it is reasonable to suggest that a mixed oxidation state of Fe occurs ($\text{Fe}^{2+}/\text{Fe}^{3+}$) within the perovskite matrix which is compensated by oxygen vacancies (V_O). Consequently, a donor dopant strategy should reduce the number of charge carriers. This project therefore, focuses on co-doping BFO with isovalent A-site Nd^{3+} and aliovalent B-site Ti^{4+} . Karimi *et al.* (2009) [8] demonstrated that the structure of BFO can be forced from polar (R3c) to antipolar (Pbam) at $x \approx 0.15$ in the solid solution $\text{Bi}_{1-x}\text{Nd}_x\text{FeO}_3$ and thus a rich tapestry of displacive as well as magnetic transitions are known to occur. Nb^{5+} , V^{5+} and Ti^{4+} are all suitable for B-site donor doping in terms of charge and size. However, Nb^{5+} and V^{5+} are comparatively refractory in Bi-based compounds [9] and it is debatable whether good homogeneity of the dopant distribution can be achieved. Ti^{4+} was therefore chosen for this study because it is known to readily react with Bi_2O_3 to form a perovskite related, ferroelectric compound $\text{Bi}_4\text{Ti}_3\text{O}_{12}$ and thus is considered most likely to be incorporated homogeneously into the perovskite lattice.

The main goal therefore of the project (Chapter 5) was to use Ti^{4+} B-site donor ions to control the conductivity in Nd-doped BFO and then undertake an investigation into the weak field dielectric and high field polarisation/strain vs field behaviour [10]. Chapter 6 focuses on the $\text{Bi}_{1-x}\text{Nd}_x\text{FeO}_3$ solid solution in which the donor dopant concentration (3 at% on the Bi site) has been optimised. The phase assemblage and structural phase transitions are further explored, and comparisons drawn with better understood ferroelectric systems such as BT and PZT [11].

Finally, 3%Ti-doped $\text{Bi}_{0.825}\text{Nd}_{0.175}\text{FeO}_3$ thin films were fabricated by pulsed laser deposition in collaboration with the group of Professor Susan Mckinstry at Pennsylvania State University, USA. The phase assemblage, dielectric and ferroelectric properties of the films are compared to bulk ceramics.

References

1. H. Schmid, *Multiferroic Magnetolectrics*, **1994**, *Ferroelectrics*, 162, 317-338.
2. M. Fiebig, *Revival of the magnetoelectric effect*, **2005**, *J. Phys.*, 38, R123.
3. W. Eerenstein, N.D. Mathur, J.F. Scott, *Multiferroic and magnetoelectric materials*, **2006**, *Nature*, 442, 759-765.
4. J. Wang, J.B. Neaton, H. Zheng, V. Nagarajan, S.B. Ogale, B. Liu, D. Viehland, V. Vaithyanathan, D.G. Scholm, U.V. Waghmare, N.A. Spaldin, K.M. Rabe, M. Wuttig and R. Ramesh, *Epitaxial BiFeO₃ multiferroic thin film heterostructures*, **2003**, *Nature*, 299, 1719-1722.
5. G. Catalan, J. F. Scott, *Physics and Applications of Bismuth Ferrite*, **2009**, *Adv. Mater.*, 21, 2463.
6. H.W. Jang, S.H. Baek, D. Ortiz, C.M. Folkman, C.B. Eom, Y.H. Chu, P. Shafer, R. Ramesh, V. Vaithyanathan and D.G. Scholm, *Epitaxial (001) BiFeO₃ membranes with substantially reduced fatigue and leakage*, **2008**, *Appl. Phys. Lett.*, 92, 062910.
7. S. Fujino, M. Murakami, V. Anbusathaiah, S.H. Lim, V. Nagarajan, C.J. Fennie, M. Wuttig, L. Salamanca-Riba and I. Takeuchi, *Combined discovery of a lead-free morphotropic phase boundary in a thin-film piezoelectric perovskite*, **2008**, *Appl. Phys. Lett.*, 92, 202904.
8. S. Karimi, I. Reaney, Y. Han, J. Pokorny, and I. Sterianou, *Crystal chemistry and domain structure of rare-earth doped BiFeO₃ ceramics*, **2009**, *J. Mater. Sci.* 44, 5102.
9. B. Yu, M. Li, J. Wang, L. Pei, D. Guo, X. Zhao *Enhanced electrical properties in multiferroic BiFeO₃ ceramics co-doped by La³⁺ and V⁵⁺*, **2008**, *J. Appl. Phys.*, 41, 185401.
10. K. Kalantari, I. Sterianou, S. Karimi, M. C. Ferrarelli, S. Miao, D. C. Sinclair, and I. M. Reaney, *Ti Doping to reduce conductivity in Bi_{0.85}Nd_{0.15}FeO₃ ceramics*, **2011**, *Adv. Funct. Mater.* 21, 3737.

11. K. Kalantari, I. Sterianou, D. C. Sinclair, P.A. Bingham, J. Pokorný and I.M. Reaney *Structural phase transitions in Ti-doped $Bi_{1-x}Nd_xFeO_3$ ceramics* submitted to J.App. Phys.

Chapter 2: Literature Review

2.1 Piezoelectric Materials

Piezoelectric materials are a class of materials that exhibit electromechanical coupling. These materials are widely used in engineering devices and systems that either convert electrical energy into mechanical displacement such as actuators and micro-positioning systems or convert mechanical energy into electrical signals.

2.1.1. Discovery of Piezoelectric effect

The piezoelectric effect was discovered by Pierre and Jacques Curie in 1880s [1]. Since then piezoelectricity has been observed in many naturally occurring materials such as tourmaline, quartz, topaz, and Rochelle salt. The Curie brothers however, did not predict the converse piezoelectric effect which was proven mathematically by Gabriel Lipmann, Marie Curie's thesis advisor [2].

2.1.2. Piezoelectricity

The piezoelectric effect is mostly associated with a lack of charge symmetry about the centre of a unit cell. There are 21 classes of crystals that do not have a centre of symmetry, with 20 of those classes being piezoelectric. The non-centrosymmetric point group 432 does not show piezoelectricity because of combinations of other symmetry elements which cancel out the effect [3]. Commercial piezoelectrics are

mainly perovskite structured and are usually solid solutions of two or more cubic end members such as PbTiO_3 .

PbTiO_3 (PT) has a non-piezoelectric cubic unit cell above its Curie point. As the material is cooled past the Curie point, a spontaneous polarization occurs as the structure transforms from a centrosymmetric cubic to a non-centrosymmetric tetragonal phase. The displacement of the Ti ion away from the centrosymmetric cubic position is schematically demonstrated in Figure 2.1. The spontaneous polarization is accompanied by an elongation parallel to and a contraction perpendicular to the polarization direction.

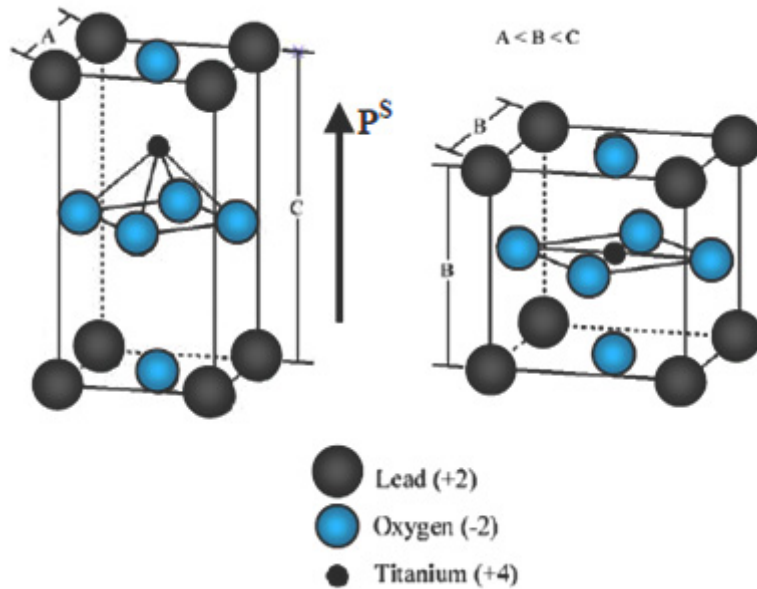


Figure 2.1: Schematic of high temperature paraelectric phase (left) and lower temperature piezoelectric phase (right) of PbTiO_3 .

2.1.3. Commercial piezoceramics

The majority of piezoelectric compositions have been developed to be exploited commercially in one of the following applications [4]: the generation of charge at high voltages, detection of mechanical vibrations and actuators, frequency control and the generation of acoustic and ultrasonic vibrations. The main materials currently used in these applications are described below.

2.1.3a. Barium titanate

BaTiO₃ (BT) was the first material to be developed as a piezoceramic and was utilized to detect mechanical and generate acoustic vibrations. Pure BT has a tetragonal structure at room temperature and when isovalently doped has high losses at the high field strengths (0.2 – 0.4 MVm⁻¹) required to make useful ultrasonic devices. The high losses in BT are attributed to the movement of domain walls. Therefore, controlling domain wall motion under applied field is critical when using BT in transducer applications.

Different dopants have been utilised in attempts to modify the properties of BT for various applications. For instance, the phase transition temperature can be altered by substituting Pb and Ca for Ba, thereby optimising piezoelectric properties around 0°C which is essential for underwater detection and echo sounding. Substitution of Ti by Zr and Sn raises the orthorhombic-tetragonal transition temperature and allows BT to be exploited as a bimorph for record-player pick-up cartridges.

2.1.3b. Lead Niobate

The ferroelectric polymorph of lead niobate (PbNb₂O₆) is metastable at room temperature [4] with the tetragonal tungsten bronze (TTB) structure above 1200°C. If doped with ZrTiO₄, rapid cooling to 700°C allows the TTB phase to persist at lower temperatures. On the other hand, slow cooling allows a transformation from TTB to a rhombohedral structure which is paraelectric at room temperature. The target market for

these materials is broadband applications and it can be heated up to 500°C without depoling

2.1.3c. Lithium niobate and lithium tantalate

Lithium niobate and tantalate have similar properties and possess the ilmenite crystal structure which consists of corner sharing MO_6 groups ($M = Nb$ or Ta) that share one face with a LiO_6 polyhedron and one with an empty O_6 octahedron [4]. Single crystal $LiNbO_3$ wafers are used as substrates for waveguide devices as well as in heat exchangers for nuclear reactors where vibration detectors make use of their high T_C .

2.1.3d. $Pb(Zr,Ti)O_3$

$Pb(Ti,Zr)O_3$ (PZT)-based materials are well-known for their distinctive combination of piezoelectric, pyroelectric, and electro-optical properties. PZT has been exploited in many different applications such as non volatile memories, optical devices, piezoelectric actuators and transducers [5]. The PZT phase diagram is illustrated in Figure 2.2. For piezoelectric applications, the most critical compositions lie close to the morphotropic phase boundary (MPB). The phrase MPB denotes an abrupt structure change with composition at constant temperature in a solid solution. In the PZT system, the MPB is at a Zr:Ti ratio of 52:48 between rhombohedral and tetragonal phases. An intermediate monoclinic structure is considered to exist at the MPB by many authors [6]. The change in structure across the MPB is associated with anomalous behaviour in physical properties such as dielectric constant and piezoelectric coupling factors [7].

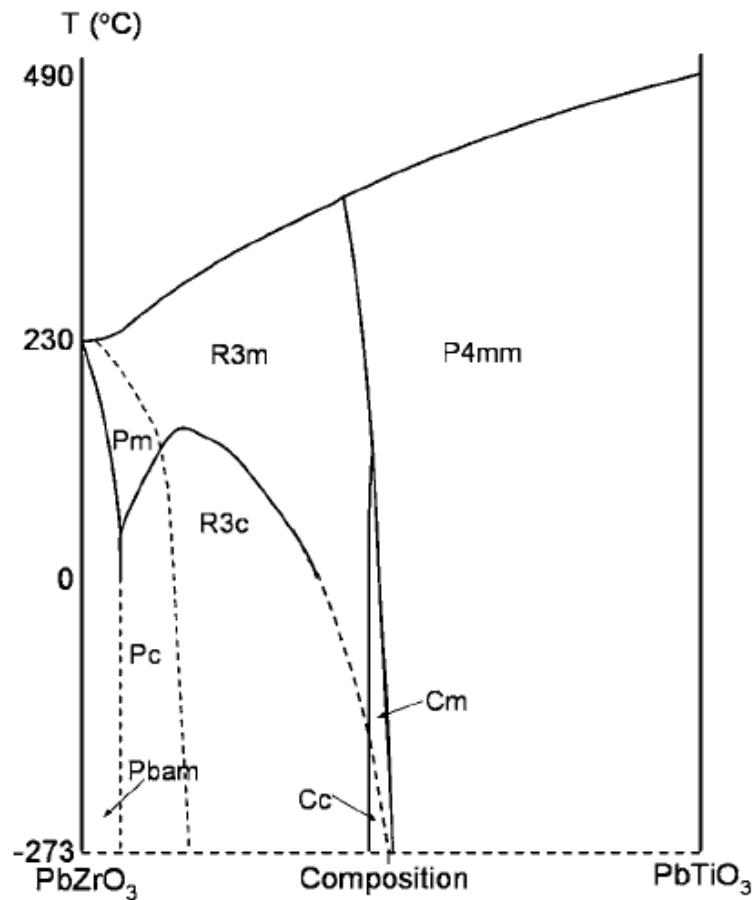


Figure 2.2: PZT phase diagram [8].

Another position in the PZT binary phase diagram that is potentially suitable for applications is at the antiferroelectric/ferroelectric (AFE/FE) phase boundary (Zr:Ti = 95:5) [9]. As ferroelectric domains carry a large spontaneous polarization and the AFE phase is centrosymmetric, the AFE phase close to the boundary may be switched to ferroelectric under high electrical field. The ease with which AFE/FE switching occurs is influenced by doping. For instance, doping PZT with Sn extends the AFE phase field, influences the phase transition characteristics, and changes the slope of AFE-FE phase boundary [10]. The transition from paraelectric (PE) to ferroelectric increases the volume of the prototype unit cell but the AFE phase has a smaller fundamental cell volume than the PE phase. Therefore, at the AFE-FE phase boundary, any decrease in volume favours the AFE phase under suitable hydrostatic or uniaxial stress [11].

2.2. Multiferroic materials

Any material which has at least two of the three properties, ferroelectricity, ferromagnetism or ferroelasticity, is by definition multiferroic. The ability to couple these properties make multiferroics potential candidates for tuneable multi-functional applications [12, 13].

2.2.1. Ferromagnets

Ferromagnets are materials which possess a magnetic moment in the absence of an applied magnetic field and which undergo a transition (T_C) to a high temperature paramagnetic phase that has no macroscopic magnetic moment. Ferromagnetic properties may be analysed from hysteresis diagrams, Figure 2.3, where H is the magnetic field and B is the flux density. Starting from the unmagnetised state, the magnetic induction increases by increasing the magnetic field up to the saturation induction, B_s . Subsequently, when the field is removed, induction decreases to B_r , the residual induction. The amount of field which is required to reduce induction to zero is called the coercive field, H_c .

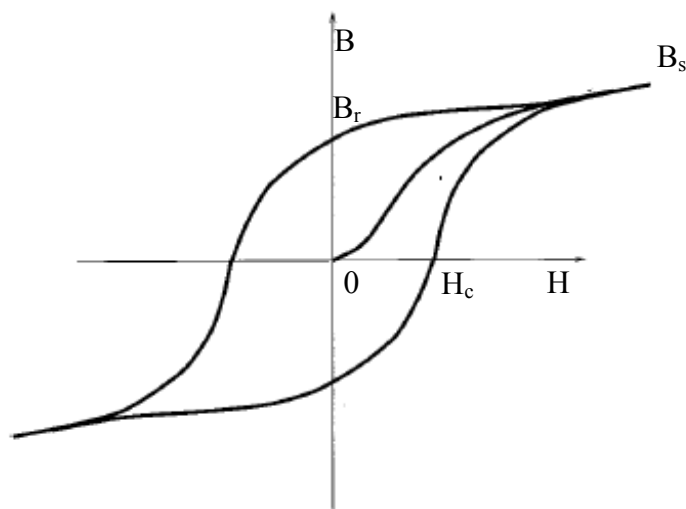


Figure 2.3: Schematic B-H hysteresis loop for a ferromagnet.

The target applications for magnetic materials largely depend on the shape and character of their hysteresis loop. Square shaped hysteresis loops are suitable for applications which require less fatigue over time, such as data storage. On the other hand, narrow hysteresis loops are suitable where rapid switching is required, for instance in transformer cores.

Another group of materials with a spontaneous magnetic moment are antiferromagnets, which have a zero net magnetisation derived from an antiparallel dipolar arrangement. Furthermore, the term ferrimagnet is used for materials with antiparallel dipoles in which some dipoles have higher intensities and cause weak net ferromagnetism [14].

Ferromagnetism in transition metals, according to the Stoner theory [15], derives from exchange between 3d and 4s orbitals. In the case that the Fermi level lies within the 3d and 4s bands, a spontaneous magnetic moment is expected. In Ni, for example, the overlap of 3d and 4s orbitals causes the valence electrons to partially occupy each band, Figure 2.4. On the other hand, Zn or Cu are not ferromagnetic since their Fermi levels lie above the 3d band.

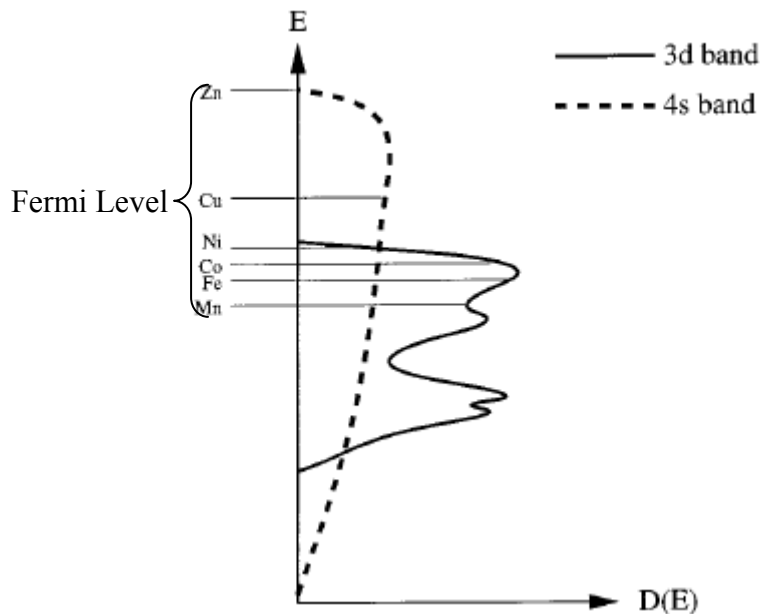


Figure 2.4: Schematic of 3d and 4s density of states for some transition metals [14].

2.2.2. Ferroelectrics

Ferroelectrics are materials with a spontaneous polarization which can be switched by an applied electric field. These materials undergo a phase transition at higher temperatures to a paraelectric phase. The temperature above which the material is no longer ferroelectric is called the Curie temperature (T_c). As with ferromagnets, ferroelectric properties can be analysed by considering their hysteresis loops in which polarization, P , corresponds to magnetisation, M , the electric field, E , corresponds to the magnetic field, H , and the electric displacement, D , corresponds to flux density, B , Figure 2.3.

There are many applications that utilise the switching behaviour of ferroelectrics. But the main application for this class of materials are in Multilayer Ceramic Capacitors (MLCCs) that make use of the high dielectric constant of BaTiO_3 based materials rather than its switching behaviour. All ferroelectrics are piezoelectric and the latter physical property gives rise to their use in actuator and transducer applications, e.g. $\text{PbZr}_x\text{Ti}_{1-x}\text{O}_3$.

From a physical perspective, the existence of point charges causes any lattice to be inherently unstable; however, short-range repulsions between adjacent electron clouds stabilize the lattice. The balance between these two forces determines the continuation of ferroelectricity. At higher temperatures, the short-range repulsions dominate the polarized state. On the other hand, as the temperature decreases, forces associated with the polarization of the ions become stronger, thereby stabilising the polarised state after removing the electric field [16]. Cohen and Krakauer [17] studied ferroelectricity in perovskites (ABO_3) and found that the hybridization between the 3d band of the B-site cation and the 2p band of the oxygen cation is essential for stabilizing ferroelectric distortion. In some cases such as PbTiO_3 , the effect is extended by hybridization of Pb (A-site) 6s orbitals and O 2p orbitals. Furthermore, B-site cation d orbitals are required to be empty in order to have lower energy to hybridise with the 2p band of oxygen.

2.2.2a. Ferroelectric Domains

The regions of the crystal with uniformly oriented spontaneous polarization are called ferroelectric domains. PbTiO_3 has been chosen as an example in order to provide clarification of this phenomenon. PbTiO_3 (PT) transforms from a non ferroelectric cubic to a ferroelectric tetragonal state at 490°C . The spontaneous polarization of PT lies along the c_T -axes of the tetragonal unit cell. The unit cell dimensions are a_T (0.390 nm) and c_T (0.415 nm) where the subscript T indicates the tetragonal phase. However, the spontaneous polarization is not uniformly aligned throughout a ceramic. The six directions along the a_C -axes are equivalent in the cubic cell. Therefore, the spontaneous polarization along c_T may arise with the same probability along any a_C axis (where c denotes cubic) as the crystal cools through T_C . The electrical and mechanical boundaries in a material impose the direction along which the polarization will develop. The regions in which only one orientation of crystal exists are called ferroelectric domains [18]. The region between the two domains is called a domain wall. The wall in-between two oppositely oriented polarizations is called an 180° wall and those that separate regions with mutually perpendicular polarization are called 90° walls, Figure 2.5 [19, 20]. The width of domain walls in ferroelectric materials is typically of the order of 1-10 nm which is as little as 2-3 unit cells but widens in the vicinity of T_C [19-21].

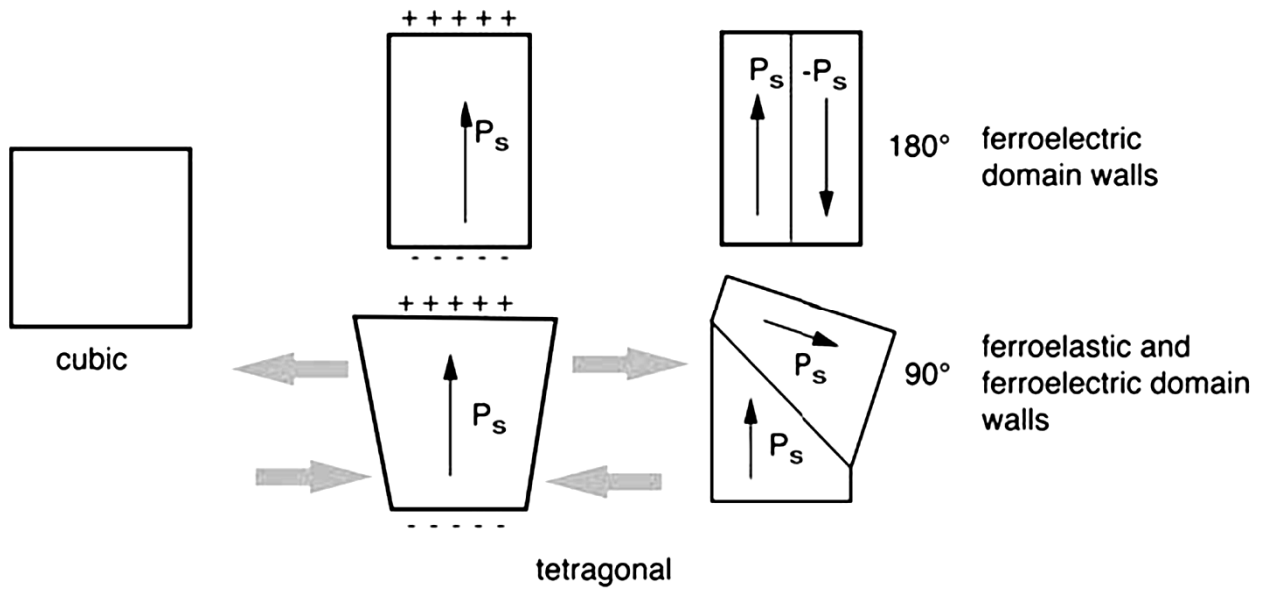


Figure 2.5: Illustration of the formation of 180° and 90° ferroelectric domain walls in a tetragonal ferroelectric material. [18].

2.2.2b. Ferroelectric hysteresis

The elastic and electric boundary conditions at each grain cause the ferroelectric grains in polycrystalline materials to split into many domains. If the spontaneous polarization of each domain aligns in a way that leads to cancelling out, the net polarization is zero and such a material does not exhibit the piezoelectric effect. Polycrystalline ferroelectric ceramics can be brought into a polar state by applying a high electric field (10-100 kV/cm). This process is called poling. Poling reorients domains within individual grains of a ceramic as close as possible to the direction of the electric field. Although many domain walls are present, a poled ferroelectric ceramic exhibits piezoelectricity. The poled state remains in the ceramic even after the removal of the poling field and is termed the remanent polarisation (P_R). P_R depends on electromechanical conditions at grain boundaries and sample surface, available domain states and imperfections such as elastic and charged defects in the material.

In terms of applications, the most significant factor of a ferroelectric ceramic is polarization reversal (or switching) by an electric field. Domain walls in polycrystalline materials will either be completely removed or decrease in number under electric field. The switching of domain walls creates hysteresis loop, Figure 2.6. The polarization increases with increase in field according to equation 2.1 at very low fields (segment AB in Figure 2.6):

$$P = \chi E \quad (2.1)$$

where P is the electric polarization, E is the applied electric field and χ is the dielectric susceptibility.

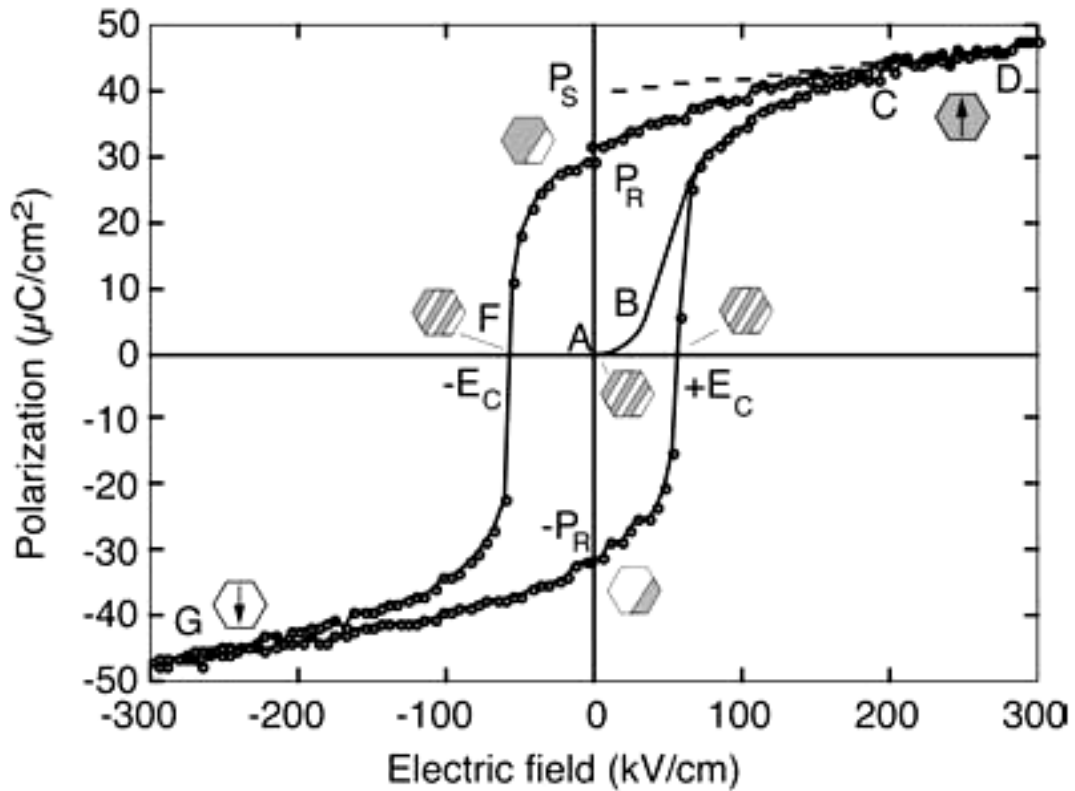


Figure 2.6: Ferroelectric hysteresis loop. The hexagonal shapes represent the domain state of the material throughout the hysteresis loop [18].

In segment AB (Figure 2.6); the field is not enough to switch domains with unfavourable directions of polarization. Increasing the field reorients the domains along directions that are crystallographically as close as possible to the direction of the field (segment BC, Figure 2.6). At this juncture, the polarization response is nonlinear and equation 2.1 is no longer valid. By point C, all domains are aligned and the ferroelectric ceramic behaves as a linear dielectric again (segment CD, Figure 2.6). When the applied electric field is removed, some domains switch back but remaining switched domains result in nonzero polarization at zero fields (P_R). To have a zero net polarization, the field must be reversed (point F, Figure 2.6). The same process may be carried out using a reverse field (point G, Figure 2.6). The typical value of P_R in ferroelectric ceramics is approximately in the range 0.001 to 1 C/m² [18, 22]. The minimum field that can bring polarization to zero is called the coercive field, E_c . The coercive field of ferroelectric ceramics is typically in the range 0.1-10 MV/m.

An ideal hysteresis loop is symmetrical with equal positive and negative coercive fields and remanent polarizations. Thermal treatment, sample thickness, mechanical stresses, preparation conditions and presence of charged defects are factors that may affect coercive field and remanent polarization.

Strain versus electric field hysteresis or “butterfly” loops, reveal further information about ferroelectric/piezoelectric materials, Figure 2.7a. Butterfly loops arise due to three key effects: i) the normal converse piezoelectric effect of the lattice, ii) switching and iii) movement of the domain walls.

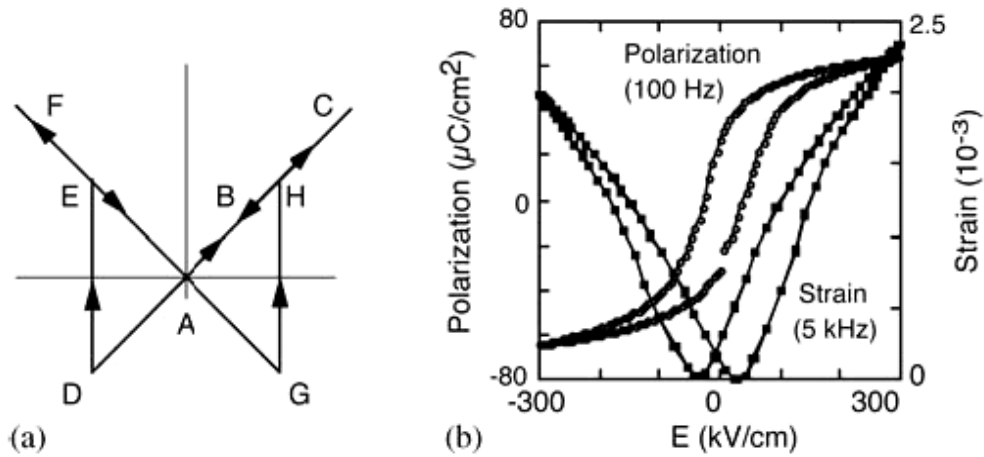


Figure 2.7: (a) schematic of an ideal butterfly loop (strain-electric field) and (b) the polarization and strain loops measured on a (111) oriented $\text{Pb}(\text{Zr}_{0.53}\text{Ti}_{0.47})\text{O}_3$ thin film [18].

To understand a strain-field curve, it is best to consider a monodomain single crystal and assume that polarization can be instantaneously switched by 180° reversal only [22]. In this case the strain of the crystal is assumed zero at point A, Figure 2.7. By increasing the electric field in the direction of spontaneous polarization, the crystal expands through piezoelectric effect (line ABC, Figure 2.7), according to equation 2.2:

$$x = d E \quad (2.2)$$

where x is strain and d is piezoelectric coefficient. The expansion continues until the maximum field is reached (point C, Figure 2.7). At this point, the field is still parallel to direction of spontaneous polarization decreases and thus the strain returns to zero (point A, Figure 2.7). The field then changes its direction and becomes antiparallel with the spontaneous polarization. According to equation 2.2, the crystal contracts with respect to point A. At point D, the field is large enough to switch the direction of polarization. After switching (point E, Figure 2.7), polarization and field have the same directions and strain is positive again. Further increase in field results in a condition defined by point F. Similar to point C, the decrease in field resets the strain to zero, according to

equation 2.2. Finally, reversal of polarization and an abrupt change in the strain occurs at point G.

A linear strain-field curve (except at the switching points) is ideal and indicates a purely piezoelectric strain. However, the strain-field relationship is more complicated due to the existence of non-180° domains. The movement and switching of these walls involves a significant change in dimensions and this effect adds to the purely piezoelectric response of the material within each domain.

2.2.3. Magnetoelectrics and multiferroics

Magnetoelectric/multiferroic materials have both ferromagnetic and ferroelectric order within the same phase. Coupling between these two properties has often been observed [23-25] but has never been strong enough to establish a clear case for their commercial application. There are few genuine magnetoelectric materials because ferroelectricity requires empty d shells to allow hopping of electrons from the filled oxygen shell but ferromagnetism requires partially filled d shells to participate in magnetic ordering [25]. In the 1950's some magnetoelectric mixed perovskites were discovered [26] in which d^0 B-site cations were replaced by magnetic d^n cations in order to induce ferromagnetism. Lone pair A-site ions such as Bi were used to induce ferroelectricity resulting in the compounds, BiMnO_3 and BFO [27]. Among these, only BFO has demonstrated the simultaneous existence of ferroelectric order ($T_C = 1123$ K) and antiferromagnetic order ($T_N = 643$ K) at room temperature [28].

2.3. Perovskites

2.3.1. Basic structure

Ideal perovskites have the general formula ABO_3 and are cubic with space group $Pm\bar{3}m$. The A-site cations are larger than the B-site cations and similar in size to the oxygen anions. The A site cations occupy the cubo-octahedral (CN12) interstice and the B site cations are in octahedral (CN6) sites. Two representations of the perovskite structure are commonly found in text books which differ only in whether the A- or B-site species are positioned at the apexes of the cube, Figure 2.8 [19, 29].

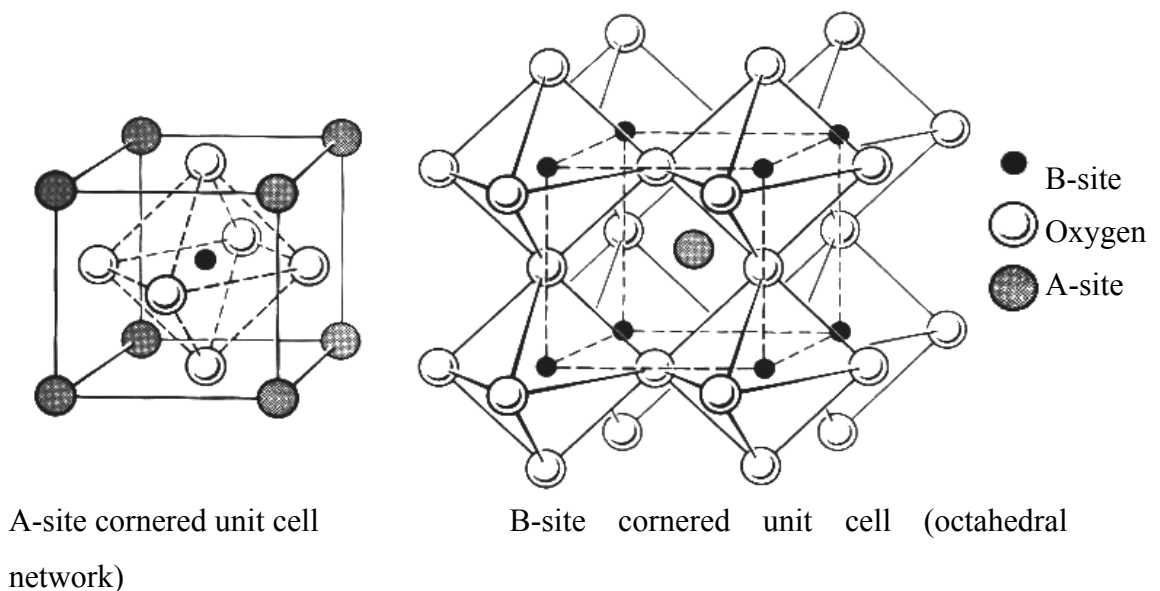


Figure 2.8: Two representations of the perovskite unit cell [19, 27 and 28].

The flexibility of composition of perovskites due to the A and B interstices having a large size difference gives rise to a wide array of functional properties, including high dielectric constant, piezoelectricity, ferroelectricity and pyroelectricity.

2.3.2. Tolerance factor

Equation 2.3 was first introduced by Goldshmit in 1926 to describe the ideal perovskite [30]:

$$R_A + R_O = \sqrt{2}(R_B + R_O) \quad (2.3)$$

where R_A , R_B and R_O are the ionic radii of the A, B and O ions, respectively. However, only a few compounds exist whose ionic radii satisfy this equation, e.g. SrTiO₃. It is more pertinent to consider the deviation from the ideal perovskite lattice which is commonly expressed using the tolerance factor, t :

$$R_A + R_O = t\sqrt{2}(R_B + R_O) \quad (2.4)$$

For $0.8 < t < 1.05$, the perovskite structure is generally stable but if $t > 1.02$ the structure distorts to a tetragonal, ferroelectric cell and if $t < 0.99$, the structure distorts due to rotations of the O-octahedra [7, 19].

2.3.3. Distorted perovskite structure

Three types of distortions are possible in the perovskite structure [19, 31 and 32]:

1. *When the A site cation is too small for the cubo-octahedral site, octahedra tilt relative to one another to reduce the size of A-site.*
2. *When the B site cation is fairly small for the octahedral site, the B site cation moves off center.* There are two possible displacements, one is parallel in which all ions displace in the same direction and the other one is antiparallel when the adjacent ions displace in opposite directions. For instance, Ti⁴⁺ parallel displacement in PbTiO₃ along $\langle 001 \rangle_p$ results in a tetragonal unit cell with one

formula unit, on the other hand, Pb^{2+} displaces in anti parallel in PbZrO_3 along $\langle 110 \rangle_p$ resulting in an orthorhombic unit cell with more than one formula unit.

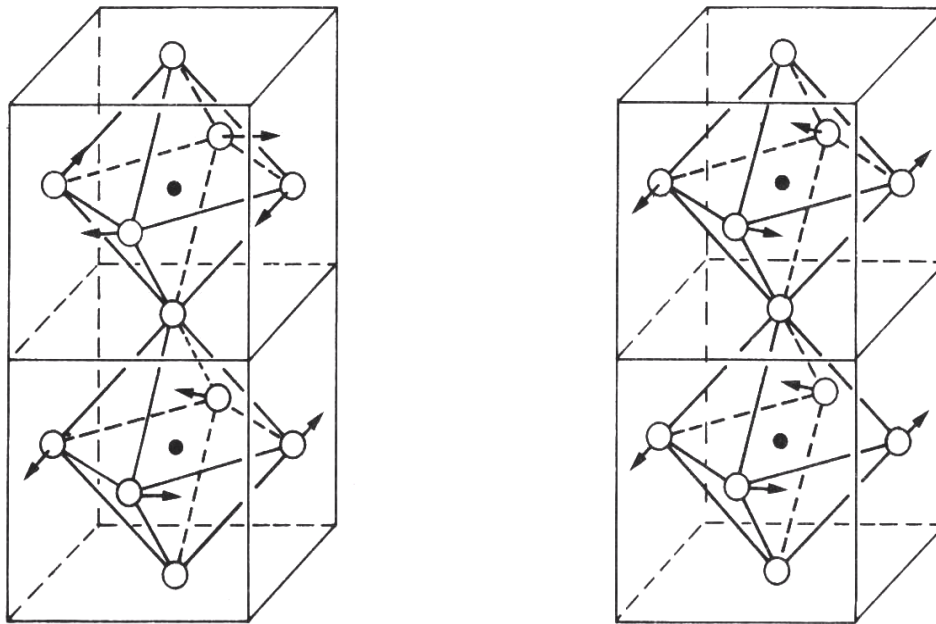
3. *Distortions of the octahedra derived from changes in A-O, B-O bonding nature.*

This occurs in perovskites with more than one type of cation in the A or B site, *i.e.* complex perovskites. In the case of cations with the same valence the long-range symmetry remains the same, however, the symmetry reduces when the mixed cations have different environmental preferences.

The structures of distorted perovskites are expressed in terms of ‘pseudo-cubic’ indices, subscript ‘p’, to simplify discussion or to draw direct comparison between perovskites.

2.3.3a. *Octahedral tilting*

Octahedral tilting is by far the most important factor when determining the overall symmetry of perovskites. This is best illustrated by substituting Ca (1.35 Å) for Sr (1.44 Å) in cubic SrTiO_3 . As the Ca concentration increases, the A-site no longer completely fills the cubo-octahedral site and the octahedra will try to reduce the volume of the site by tilting. As a result, the structure becomes orthorhombic [19]. Glazer (1972) proposed a methodology to explain and classify tilting of BO_6 octahedra in perovskites [33]. The methodology broke the octahedral tilting into components of tilt around the pseudo-cubic axes: a_p , b_p and c_p , where ‘a’ refers to the amplitude of the tilt about the [100] axis, ‘b’ about [010] axis and ‘c’ about [001] axis. The tilting of adjacent layers of octahedra along the three axes will be either in-phase, denoted by superscript ‘+’, or antiphase, denoted by superscript ‘-’ or no tilt is denoted by superscript ‘0’, Figure 2.9 [19, 33].



Anti phase Tilting

In-phase tilting

Figure 2.9: Tilting of neighbouring layers of octahedral along the tetrad axis [31].

For example, $a^-a^-c^0$ demonstrates an anti phase same magnitude tilt along a and b axes and no tilt along the c axis. Octahedral tilting not only reduces symmetry, but also causes multiplication of the unit cell. Glazer identified 23 tilt systems considering a unit cell containing 8 formula units. Some of them are described in Table 2.1 [19].

Table 2.1: Examples from Glazer tilt systems [19].

Tilt system	Symbol	Multiple cell	Relative pseudo-cubic unitcell parameters	Space group
Three-tilt	$a^-a^-a^-$	$2a_p \times 2b_p \times 2c_p$	$a_p = c_p = c_p$ $\alpha = \beta = \gamma \neq 90^\circ$	R3c
Two-tilt	$a^0b^+b^+$	$2a_p \times 2b_p \times 2c_p$	$a_p < b_p = c_p$	I4/mmm
One-tilt	$a^0a^0c^-$	$2a_p \times 2b_p \times 2c_p$	$a_p = b_p < c_p$	F4/mcm
Zero-tilt	$a^0a^0a^0$	$a_p \times b_p \times c_p$	$a_p = b_p = c_p$	Pm3m

The effect of tolerance factor on octahedral tilting in Sr- and Ba- based complex perovskites was studied by Reaney *et al.* [1994], leading to the following tilt regimes according to the tolerance factor [32, 34]:

1. Untilted structures at room temperature for $0.985 < t < 1.06$
2. Antiphase tilting at room temperature for $0.964 < t < 0.985$
3. Both antiphase and in-phase tilting at room temperature for $t < 0.964$

2.3.3b. Crystallography of Perovskites

In X-Ray Diffraction (XRD), perovskites give rise to a sequence of strong ($h + k + l = 2n$) and weak ($h + k + l \neq 2n$) lines, which are dominated by the cation sublattice. Typically, the strongest peak in the XRD is usually the $\{110\}$ reflection [21, 22] which has contributions to scattering from both the A and B-site cation sublattices. However, weak superlattice reflections, particularly if they relate to the O sublattice are difficult to detect and often distortions away from the prototype symmetry go undetected. Structural studies often therefore, exploit neutron diffraction to obtain more precise information of the anion positions, bond lengths and displacement parameters [35, 36]. As an illustration, neutron and x-ray diffraction patterns of SrTiO_3 and KMgF_3 are presented in Figure 2.10. SrTiO_3 has an ideal perovskite structure, $t = 1$, based on strong 110 and 220 reflections in XRD and strong 111 and 311 reflections in neutron diffraction. The perovskite structure of KMgF_3 can be detected by XRD but the deviation from the ideal perovskite structure can only be detected by weak 111 and 311 reflections in the neutron diffraction pattern.

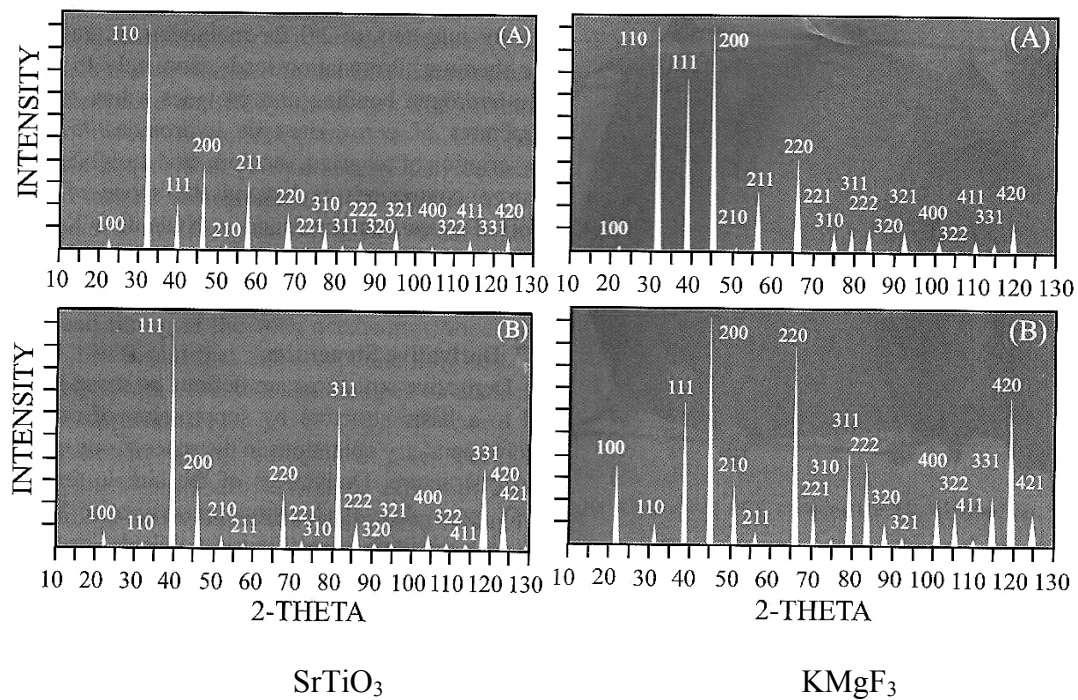


Figure 2.10: Comparison between, A. X-ray and B. neutron diffraction patterns of an ideal and distorted perovskite [35].

The dynamical nature of electron diffraction ensures that all superstructure reflections can be observed but the intensities of the reflections cannot be quantified. Despite this limitation, Reaney *et al.* [1994] and later Woodward *et al.* [2005] utilised electron diffraction to detect weak O-octahedral tilting invisible to XRD and difficult to resolve even by neutron diffraction [31, 34].

The methodology described by Woodward *et al.* [2005] illustrated how in single domain diffraction data, the major zone axes, $\langle 100 \rangle$, $\langle 110 \rangle$ and $\langle 111 \rangle$ could be used to distinguish between space groups [31]. Figure 2.11 shows fundamental reflections observed along the principal zone axes. Figure 2.12 shows additional spots of type $\frac{1}{2}(ooo)$, where ‘o’ refers to an odd number, in $\langle 110 \rangle_p$ zone axis, driven from anti-phase tilting of octahedra. Grey spots in Figure 2.13 are $\frac{1}{2}(ooe)$ type, where ‘e’ refers to an even number, in $\langle 100 \rangle_p$ zone axes, which correspond to in-phase tilting of octahedra. By carefully determining the distribution of these reflections in reciprocal space, subtle

difference in tilt systems may be determined which are difficult to resolve using ‘volume-averaged’ techniques such as neutron and X-ray diffraction.

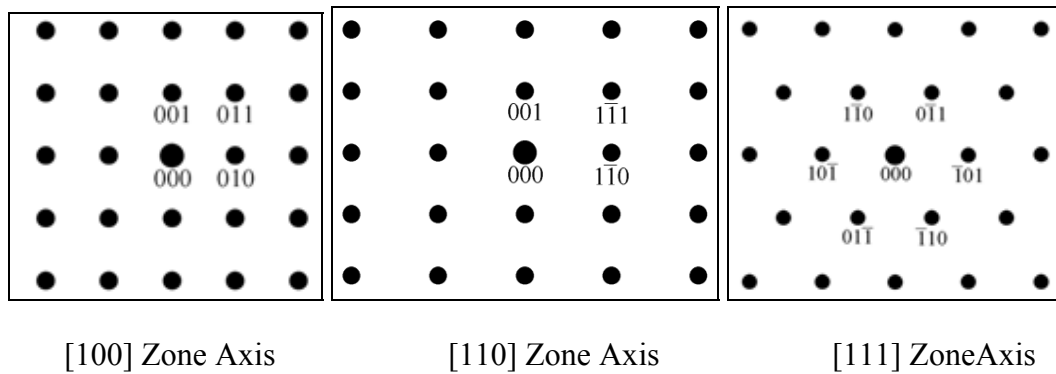


Figure 2.11: Fundamental reflections in electron diffraction patterns of the cubic perovskite [31].

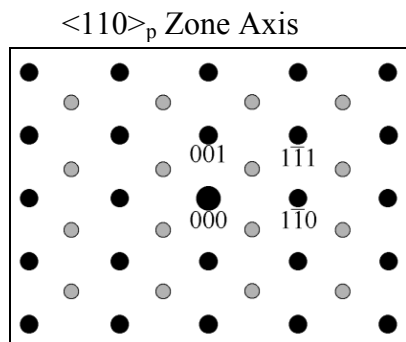
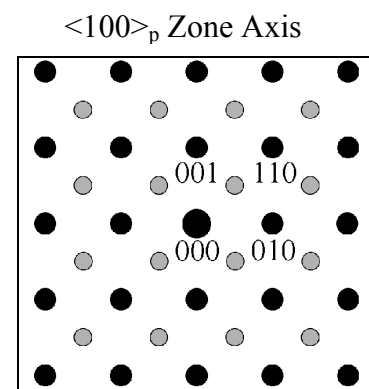


Figure 2.12: Anti phase tilt spots (grey coloured) in between fundamental reflections [30].

Figure 2.13: In-phase tilt spots (grey coloured) between fundamental reflections [30].



2.4. BiFeO₃ (Bismuth Ferrite)

2.4.1. Structure

BiFeO₃ (BFO) has a perovskite structure in which Bi³⁺ ions are in the 12 coordinated cubo-octahedral sites and Fe³⁺ ions are in the 6 coordinated octahedral sites. Mitchel *et al.* [27] describe the structure as a rhombohedrally distorted perovskite which belongs to the space group R3c [37]. The unit cell parameters are $a = 5.637\text{\AA}$ and $\alpha = 59.344^\circ$. The tilt system is $a\bar{a}a\bar{a}$ which is accompanied by parallel off-centre displacement of both cationic sublattices, resulting in a doubling of the unit cell. In other words, the FeO₆ octahedra rotate about the $\langle 111 \rangle_p$ direction in an anti phase manner. In an ideal perovskite, oxygen coordination number is 6, from which 4 are A site and the other 2 are B site cations. However, in BFO, the lone electron pair in Bi³⁺ results in displacement along the $[111]_p$, leaving the oxygen ions in 4 coordinated environments, Figure 2.14 [38, 39].

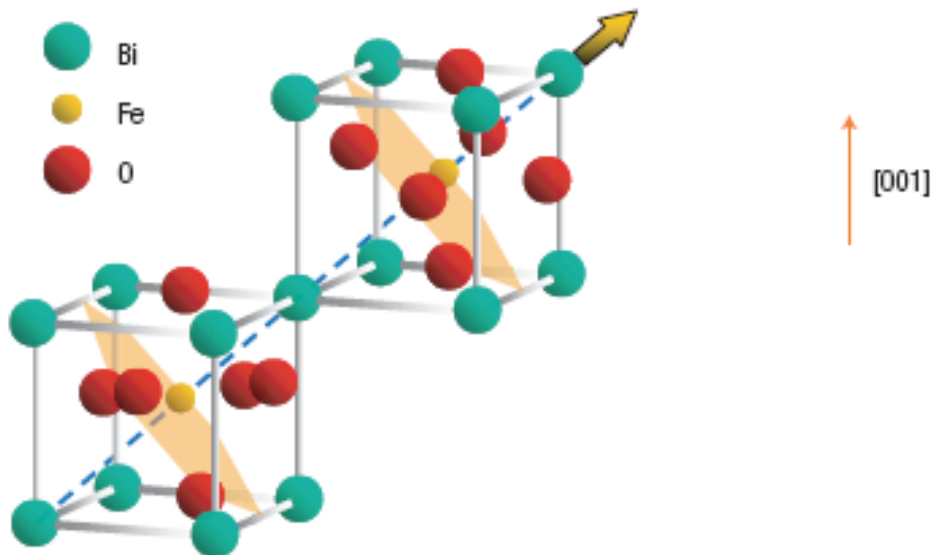


Figure 2.14: Schematic of unit Cell doubling in BFO driven from octahedral tilting along the $[111]_p$ direction [39].

2.4.2. Properties

BFO is so far the only known room temperature magnetoelectric material [32, 40 and 41]. Ferroelectric behaviour is present below T_C (≈ 1100 K). Above T_C the structure is orthorhombic with the $a^-a^+c^+$ tilt system and Pnma symmetry [40]. BFO exhibits antiferromagnetic ordering below $T_N \approx 640$ K above which it is paramagnetic.

The Bi^{3+} lone electron pair is responsible for ferroelectricity in BFO with two electrons in the 6s orbital (lone pair) displaced away from the centrosymmetric position relative to adjacent oxygens. A broad range of experimental values of polarization from $6.1 \mu\text{C cm}^{-2}$ by Teague *et al.* [42] for bulk single crystals to $158 \mu\text{C cm}^{-2}$ for polycrystalline films [43, 44] have been reported in the literature. The explanation for these diverse values is still a matter of scientific debate [45-47]. It is generally accepted however, that the displacement of cations in BFO is large relative to non-lone-pair perovskites and is consistent with other Bi based perovskites. This results in high spontaneous polarization but due to high leakage currents and the high T_C , the hysteresis loops of polarization vs. applied electric field are not saturated [48].

As discussed previously, magnetism requires transition metal ions with partially filled d-shells, since spins of completely filled shells add to zero. Accordingly, only the Fe^{3+} sublattice is responsible for magnetic behaviour, as reported by Smolenski and Yudin in 1965. Early neutron diffraction experiments have determined that BFO is antiferromagnetic with a G-type spin configuration in which the magnetic dipoles associated with the Fe^{3+} ions are each bordered by six antiparallel nearest neighbours [49]. However, in 1982, magnetic order in BFO was refined to include the presence of cycloidal spirals in the $[110]_h$ direction with a period of $\lambda = 620 \text{ \AA}$, of which their spin rotation is $(110)_h$ [50].

2.4.3. Critical issues with BiFeO_3

Currently, the magnetoelectric properties of BiFeO_3 (BFO) are not suitable for its use in memory applications. The leakage current is too high and therefore the ferroelectric behaviour is compromised [51, 52]. Moreover, BFO is essentially

antiferromagnetic rather than ferromagnetic which leads to cancelling of macroscopic magnetization and generally prohibits linear magnetoelectric effects.

Extrinsic issues such as the existence of secondary phases, $\text{Bi}_2\text{Fe}_4\text{O}_9$, $\text{Bi}_{12}(\text{Bi}_{0.5}\text{Fe}_{0.5})\text{O}_{19.5}$, $\text{Bi}_{25}\text{FeO}_{40}$ and $\text{Bi}_{46}\text{Fe}_2\text{O}_9$ and the volatilization of bismuth have largely been resolved by the use of suitable processing and dopants [53, 54]. Rapid liquid phase sintering [55] and leaching secondary phases with nitric acid [54] are the main methods that have improved phase purity in undoped BFO.

2.4.4. A-site Doped BiFeO_3

A-site isovalent, rare earth doping has also been used to reduce secondary phases [56-58]. ReFeO_3 , where Re = rare earth, compounds have a distorted orthorhombic structure which belongs to space group Pbnm. NdFeO_3 has two Néel temperatures (T_N): one at 1.5 K, below which C type antiferromagnetic ordering is exhibited, and another at 760 K, below which the magnetic order of Fe^{3+} ions is canted G-type [59, 60].

Substitution of Re for Bi in BFO eventually results in a transformation to the Pbnm cell but for La, Nd and Sm compounds an antipolar, PbZrO_3 structure is stabilised at >14 mol% Re concentration [53, 56]. Karimi *et al.* [53] suggested that the formation of a PbZrO_3 structured phase in Nd-doped BFO may be best explained by analogy with the PZT phase diagram, Figures 2.15 and 2.16. In the PZT phase diagram, substituting Zr^{4+} for Ti^{4+} decreases the tolerance factor and ionic polarisability of the perovskite phase. This is believed to encourage PZT to transform from ferroelectric rhombohedral to antiferroelectric orthorhombic [32, 35]. The same trend can be induced in BFO in which Nd and Sm decrease the tolerance factor and polarisability of a rhombohedral perovskite phase causing a transformation to an orthorhombic antipolar cell.

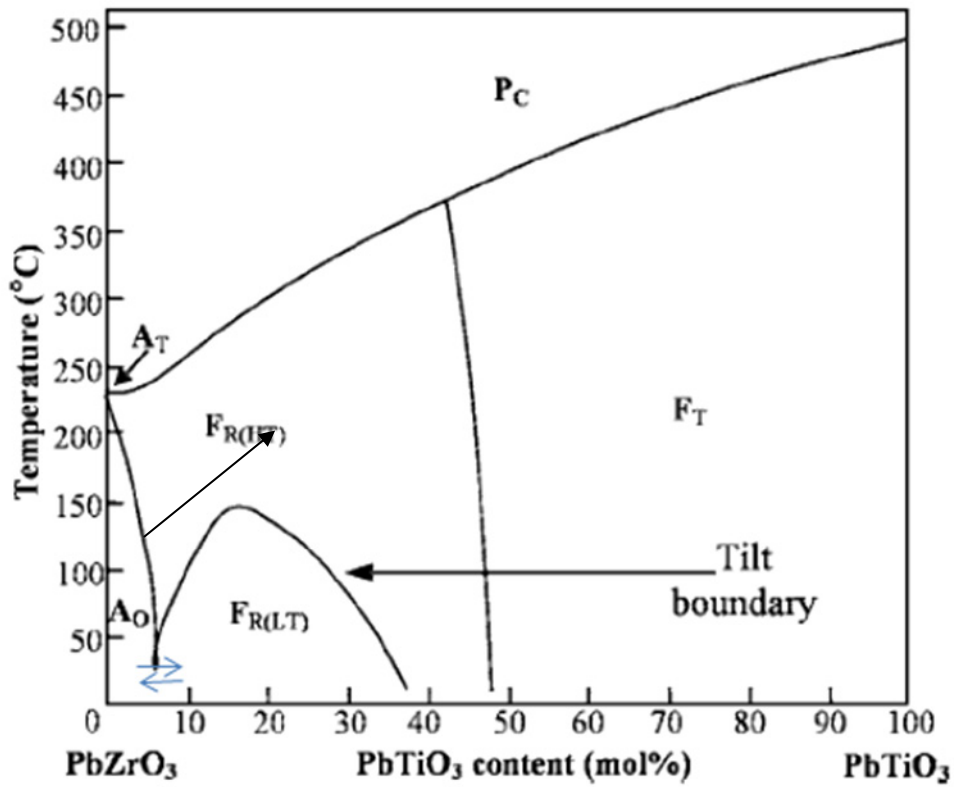


Figure 2.15: PZT phase diagram. Arrows indicate antiferroelectric-ferroelectric phase transition [8].

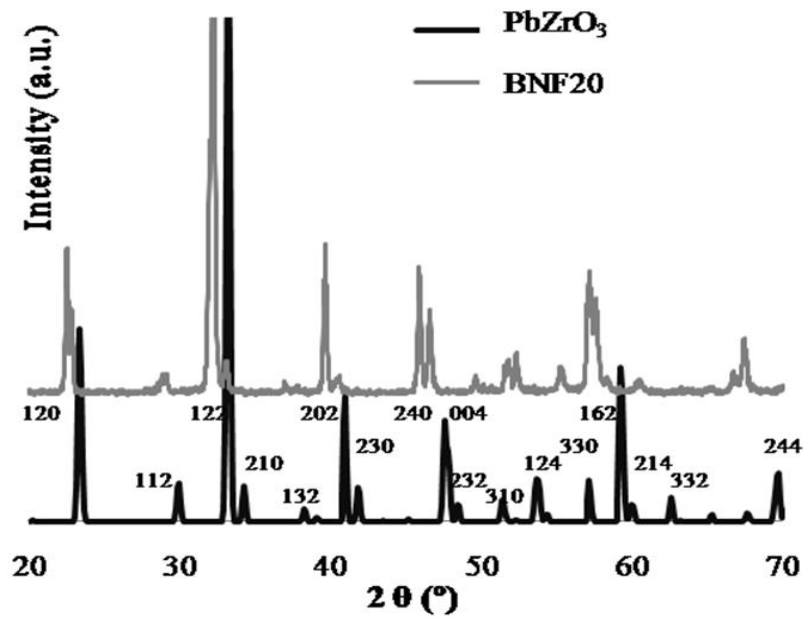


Figure 2.16: Comparison of experimental XRD traces from Bi_{0.8}Nd_{0.2}FeO₃ and PZ [56].

The analogy between PZ and the intermediate phase (PZ-like) was also confirmed by electron diffraction (ED), Figures 2.17 and 2.18. For $\text{Bi}_{1-x}\text{Nd}_x\text{FeO}_3$, $0.15 < x < 0.2$ samples, the fundamental perovskite unit cell is quadrupled along one of the $\langle 110 \rangle$ directions, Figure 2.17 (periodicity of $2\sqrt{2}a$), similar to PZ, with the appearance of $\frac{1}{4}\{hk0\}_p$. In addition however, a second quadrupled direction, not typical of PZ, was observed along the c-axis giving rise to an approximate $4c$ periodicity and the appearance of $\frac{1}{4}\{00l\}_p$ reflections [53]. For comparison, Figure 2.18 shows typical ED patterns from the major zones in PZ. [8].

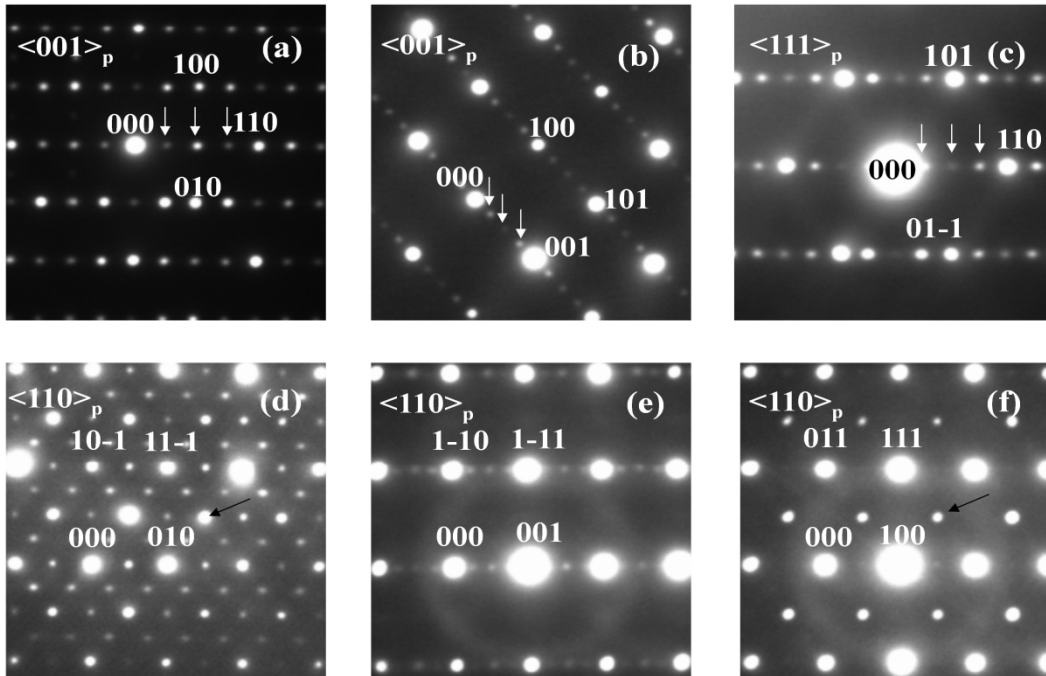


Figure 2.17: Electron diffraction patterns of $\text{Bi}_{0.8}\text{Nd}_{0.2}\text{FeO}_3$ ceramics. (a) and (b) are variants of the $\langle 001 \rangle_p$ zone axes. (c) is a variant of the $\langle 111 \rangle_p$ zone axes. (d), (e) and (f) are variants of $\langle 110 \rangle_p$ zone axes. Arrowed in (a), (b) and (c) are $\frac{1}{4}\{hk0\}$ and $\frac{1}{4}\{hk0\}$ reflections. Arrowed in (d), (e) and (f) are $\frac{1}{2}\{hkl\}$ reflections [53].

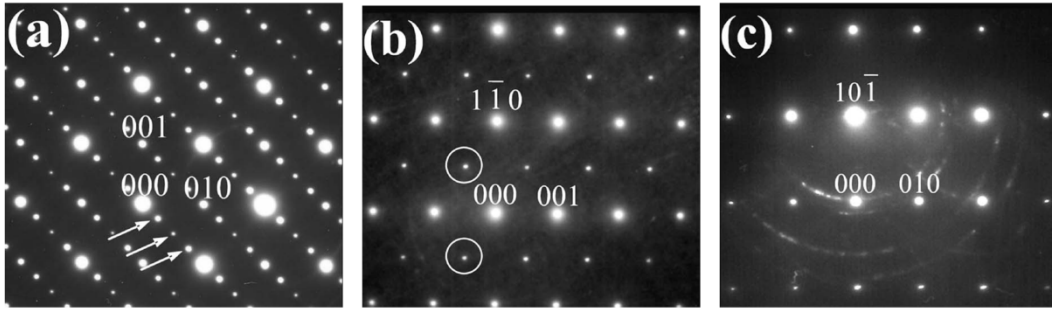


Figure 2.18: Zone axes diffraction patterns of PZ. (a) $\langle 100 \rangle_p$ zone axis with $\frac{1}{4}\{hkl\}_p$ superlattice reflections which are arrowed. (b) $\langle 110 \rangle_p$ zone axis with $\frac{1}{2}\{hkl\}_p$ reflections ringed. (c) $\langle 110 \rangle_p$ zone axis without $\frac{1}{2}\{hkl\}_p$ reflections [8].

Table 2.2 collates the effect of A-site, RE doping on BFO. Other than rare earths, up to 30 mol% Ca, Sr, Pb and Ba ions have been used to substitute for Bi. No structural phase transitions were induced and the dopants with larger ionic radius (Pb and Ba) suppressed the spiral spin structure of BFO [52]. Moreover, the band gap increased from 1.8 eV to 2.3 eV. The main benefit however, was the stabilisation of Fe^{3+} with respect to Fe^{2+} [52]. Stoichiometric $\text{BiFeO}_3\text{-PbZrO}_3$ solid solutions have also been fabricated in which the Néel temperature decreased with decreasing Fe concentration [61].

Table 2.2: The effect of various A-site dopants on BiFeO₃ properties.

Reference	Ion	General Modification	Structural Effect
55 and 61	La ³⁺	<ul style="list-style-type: none"> Eliminates the secondary phases Enhanced magneto-electric interactions derived from destruction of the cycloidal spin structure 	
55, 56 and 62	Sm ³⁺	<ul style="list-style-type: none"> Eliminates the secondary phases Enhanced piezoelectric properties Significantly higher remnant polarization and coercive field Canted anti ferromagnetic order 	
55, 57 and 63	Gd ³⁺	<ul style="list-style-type: none"> Decrease amount of secondary phase Decrease of Néel temperature Increase of magnetisation Both dielectric constant and loss decreased. 	
52 and 55	Nd ³⁺	<ul style="list-style-type: none"> Eliminate Secondary phases Collapse of spin structure in higher doping levels. Improve ferroelectric properties Possible significant magnetoelectric coupling 	

2.4.5. B-site doped BiFeO₃

Although rare earth A-site doping reduces the volume fraction of secondary phases in BFO, it does not significantly decrease the leakage current and the permittivity and loss show large anomalies that are attributed to space charge effects, Figure 2.19.

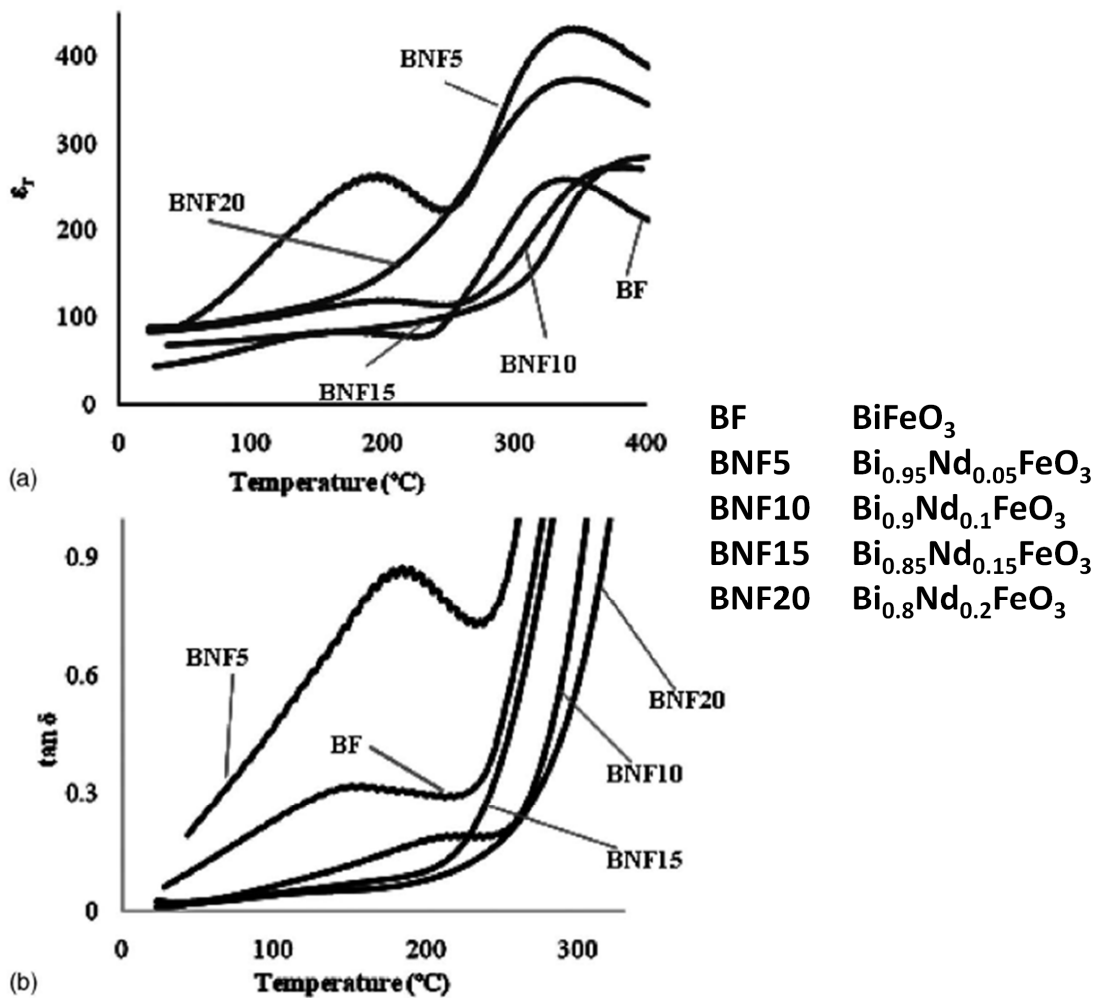


Figure 2.19: Permittivity and dielectric loss vs. temperature of Nd doped bismuth ferrite samples. The peaks in permittivity do not correspond to phase transitions but rather to space-charge effects [53].

Even though the source of conductivity in BFO-based ceramics is still a point of controversy, it is intuitively reasonable to suggest that reduction of Fe³⁺ to Fe²⁺ occurs

within the perovskite matrix, compensated by oxygen vacancies (V_O). As a result, donor doping should reduce the concentration of V_O by compensating for Fe^{2+} , thus reducing the number of charge carriers. A-site donor doping, unlike Pb-based compounds, is not possible in BFO-based ceramics. This is because there are no tetravalent ions large enough for the A-site.

B-site doping has to date only been sparsely investigated, although some efforts have been reported [65, 66]. For donor ions, compensation may be by the presence of native Fe^{2+} or its formation or by the creation of cation vacancies on the A or B-site.

Acceptor doping typically is compensated by the formation of anion vacancies (V_O) or an increase in valence (Fe^{3+} to Fe^{4+}) [52]. In particular, donor dopants have been shown to improve properties [65-67] in ceramics and thin films, resulting in a decrease in the leakage current due to removal of V_O , an improvement in the hysteresis with the maximum reported Pr value of $39.4 \mu C cm^{-2}$, and a high switching polarization after being subjected to 2×10^{10} read/write fatigue cycles. Nb^{5+} , V^{5+} and Ti^{4+} B-site donor dopants all appear suitable for donor doping in terms of charge and size. Despite the fact that smaller amounts of Nb^{5+} and V^{5+} compensate for more Fe^{2+} in BFO, they are highly refractory with respect to Bi-based compounds. In other words, it is doubtful whether Nb_2O_5 and V_2O_5 could attain a homogeneous distribution during ceramic fabrication [65]. Therefore, Ti^{4+} was chosen for this study not only because it is known to readily react with Bi_2O_3 , but also it is a highly polarisable ion which may couple to Bi displacements.

Yu *et. al* [65] co-doped $BiFeO_3$ according to the solid solution $Bi_{0.85}La_{0.15}Fe_{1-x}V_xO_3$ ($x = 0-0.1$) and prepared ceramics by a rapid liquid sintering technique. They reported a decrease in leakage current and dielectric loss but additionally observed residual Bi_2O_3 and an unknown impurity phase in samples with $x \leq 0.03$, Figure 2.20. However, the samples still demonstrated improved fatigue characteristics after 2×10^{10} read/write cycles, Figure 2.21.

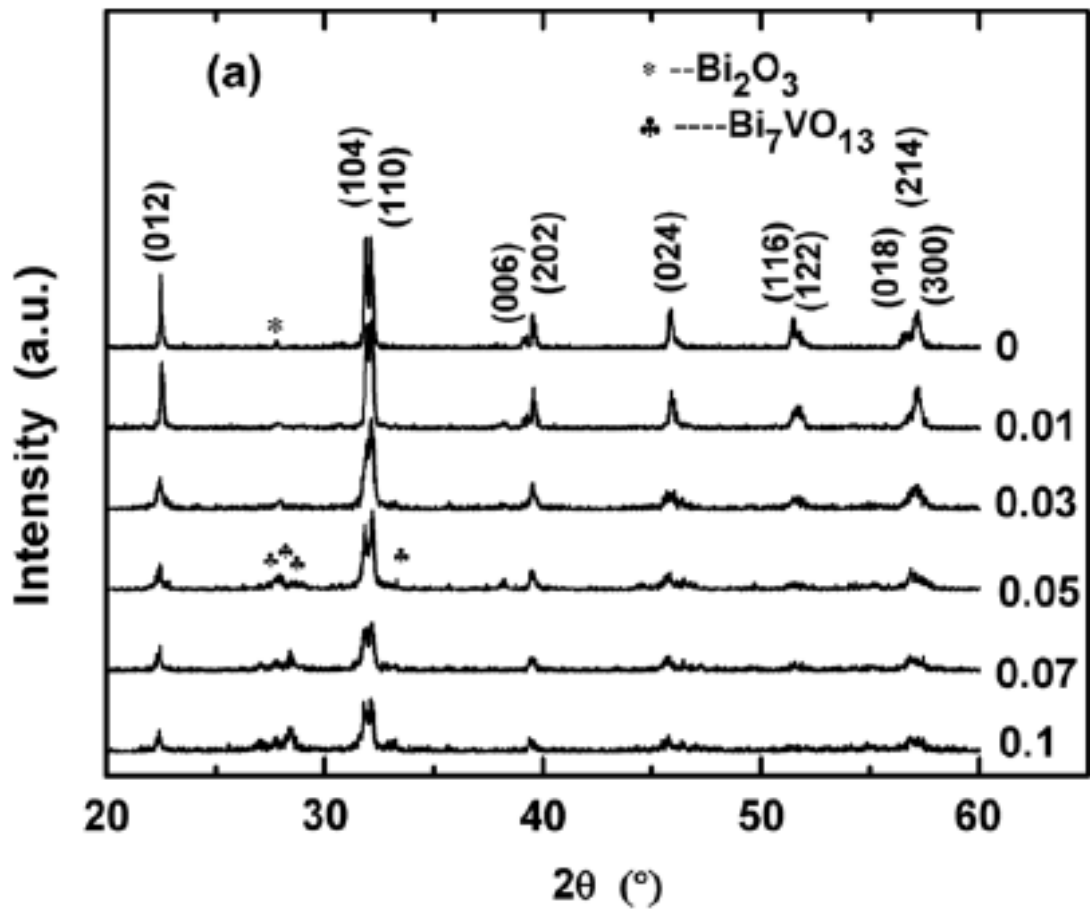


Figure 2.20: X-ray diffraction results of $\text{Bi}_{0.85}\text{La}_{0.15}\text{Fe}_{1-x}\text{V}_x\text{O}_3$ ceramics reported by Yu *et al.* [65].

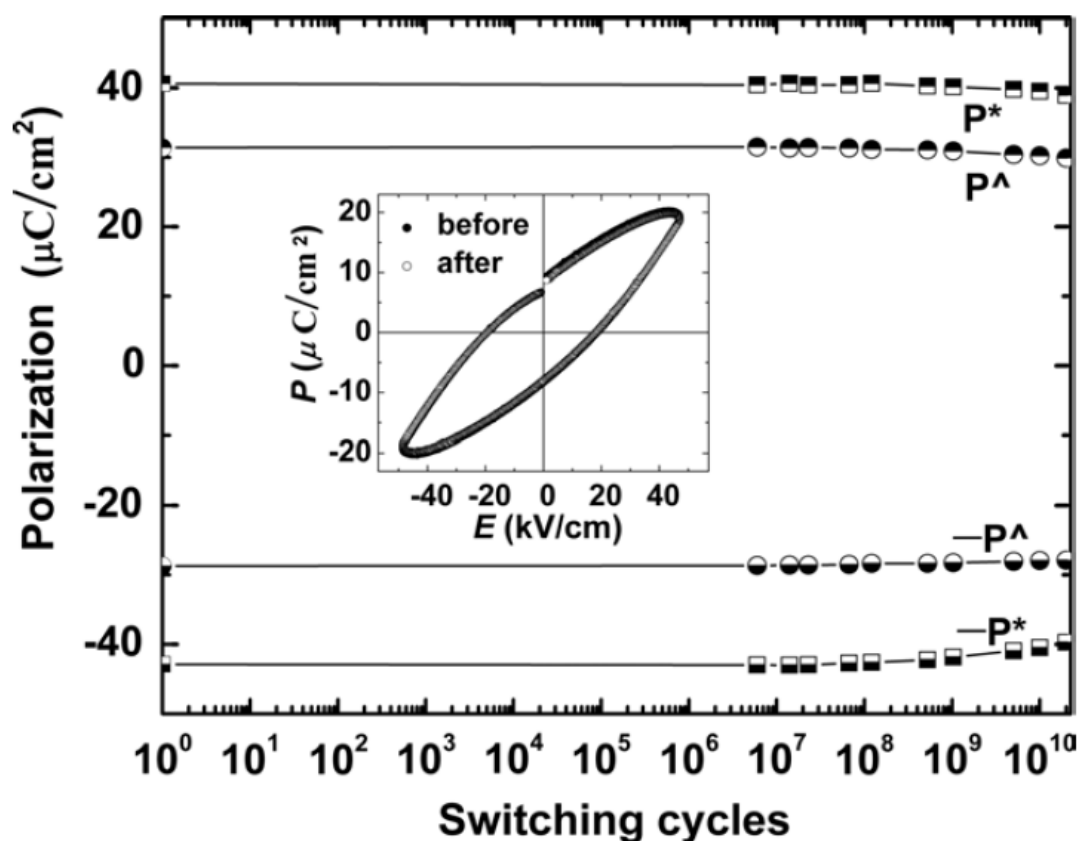


Figure 2.21: Fatigue of $\text{Bi}_{0.85}\text{La}_{0.15}\text{Fe}_{1-x}\text{V}_x\text{O}_3$ ($x=0.01$) at $E = \pm 50 \text{ kV cm}^{-1}$ and $f = 1 \text{ MHz}$, reported by Yu *et al.* Note that hysteresis loops for ‘before’ and ‘after’ coincide [65].

Nb doping in BiFeO_3 has also been reported by Jun *et al.* [66] but these authors did not experimentally indicate the phase purity of their samples but simply stated that Bi_2O_3 and $\text{Bi}_2\text{Fe}_4\text{O}_9$ phases were present. Despite the presence of second phase, Nb doping improved the electrical resistivity of the ceramics by six orders of magnitude, Figure 2.22.

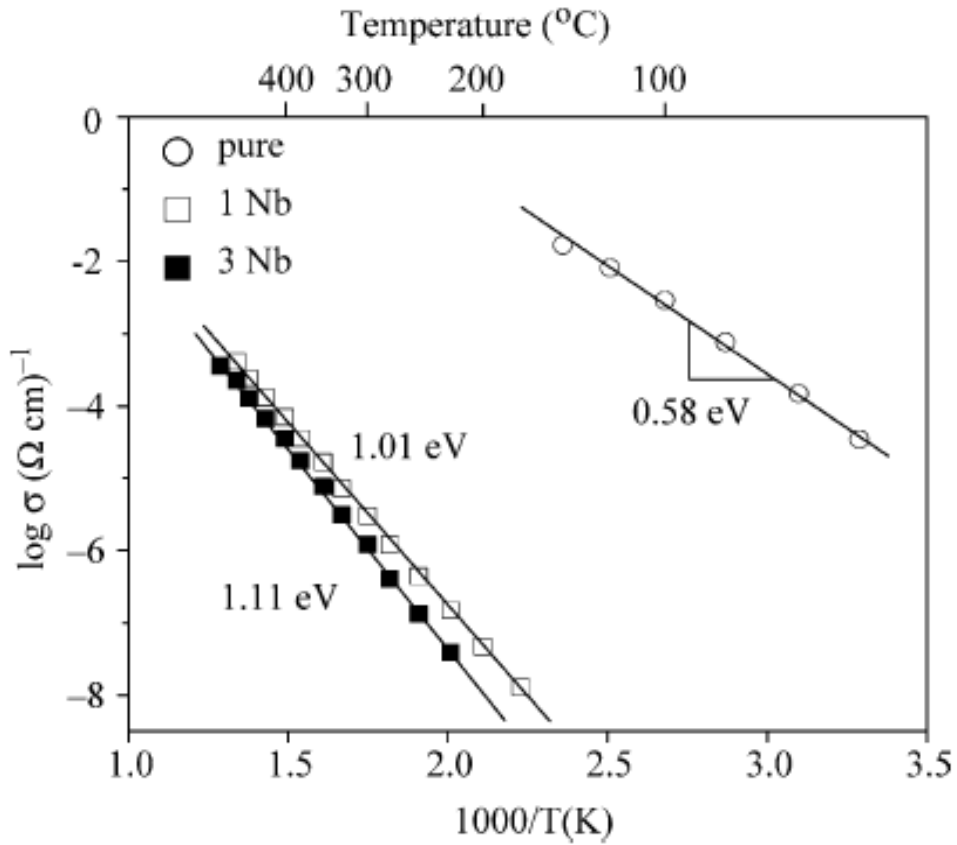


Figure 2.22: Temperature dependence of the electrical conductivity for Nb doped BiFeO₃, reported by Jun *et al.* [66].

Jun *et al.* [66] also described the multiferroic properties of Nb doped BiFeO₃, Figure 2.23, and suggested that coupling of magnetic and electric dipoles may be observed at room temperature.

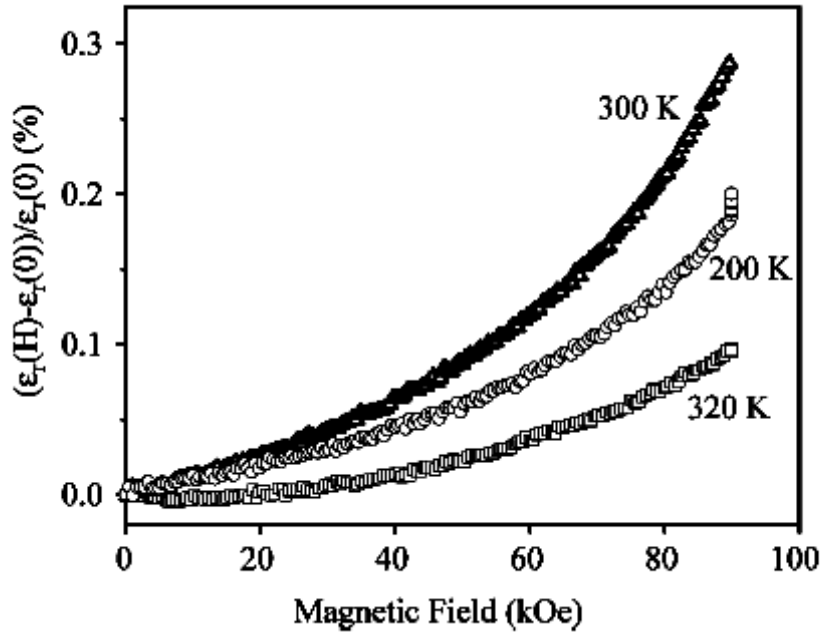


Figure 2.23: Magnetic field induced change in dielectric constant of Nb doped bismuth ferrite [66].

2.5. Focus of the Current Project

This project initially focused on Nd doped BiFeO₃ in which the antipolar state was induced in the manner described by Karimi *et al.* [53]. Nd-doped BFO ceramics were additionally donor doped on the B-site using Ti⁴⁺ and the resulting ceramics studied using a range of structural and electrical characterisation techniques. Particular attention was paid to how dopants affect the conductivity of the ceramics and whether the leakage current could be reduced sufficiently to record permittivity data representative of the intrinsic lattice and whether classic saturated hysteresis loops could be obtained.

References

1. J. Curie and P. Curie, *Development par compression de l'électricité polaire dans les cristaux hémédres à faces inclinées*, **1880**, Bulletin no. 4 de la Société Mineralogique de France, 91, 294.
2. Lippman, G., *Principe de la conservation de l'électricité*, **1881**, Annales de chimie et de physique, 24: p. 145.
3. J.F. Nye, *Physical properties of crystals: their representation by tensors and Matrices*, **1967**, London: Oxford University Press, Oxford.
4. Moulson, A.J. and J.M. Herbert, *Electroceramics: Materials, properties applications*, **2003**, 2nd ed., West Sussex, England: John Wiley & Sons.
5. T. Tanaka, *Piezoelectric devices in Japan*, **1992**, Piezoelectricity, American Institute of Physics, New York.
6. Noheda, B., J.A. Gonzalo, L.E. Cross, R. Guo, S.E. Park, D.E. Cox, and G. Shirane, *Tetragonal-to-monoclinic phase transition in a ferroelectric perovskite: The structure of $PbZr_{0.52}Ti_{0.48}O_3$* . Physical Review B, 2000. **61**(13): p. 8687-8695.
7. B. Jaffe, W.R.J. Cook, H. Jaffe *Piezoelectric ceramics*, **1971**, Academic Press, London.
8. D.I. Woodward, J. Knudsen, I.M. Reaney *Review of crystal structures in the $PbZr_xTi_{1-x}O_3$ solid solution*, **2005**, Phys. Review, B 72, 104110
9. Y. L. Wang, *Phase transition study of PZT 95/5 ceramics*, **1988**, Physica B150, 168-174.

10. Z. M. Chen, J. Y. Lian and Y.L. Wang, *Phase transition studies PSZT ceramics with vertical ferro-antiferroelectric phase boundary*, **1990**, *Ferroelectrics*, 101, 225-234.
11. D. Berlincourt, *Stability of phases in modified lead zirconate with variation in pressure, electric field, temperature and composition*, **1964**, *Phys. Chem. Solids*, 25, 659-74.
12. S. Dong, J.F. Li, D. Viehland *Ultrahigh magnetic field sensitivity in laminates of TERFENOL-D and $Pb(Mg_{1/3}Nb_{2/3})O_3$ - $PbTiO_3$ crystals*, **2003** *J. App. Phys.*, Vol 83, 11E.
13. A.S. Poghossian, H.V. Abovian, P.B. Avakian, S.H. Mkrtchian, V.M. Haroutunian *Bismuth ferrites: new materials for semiconductor gas sensors*, **1991** *Sensors and Actuators B*, 4, 545-549.
14. N.A. Hill *Why are there so few magnetic ferroelectrics*, **2000**, *J. Phys. Chem.*, B24, 6694.
15. E.C Stoner *Atomic moments in ferromagnetic metals and alloys with nonferromagnetic element*, **1933**, *Pilos. Mag.*, 15, 1080.
16. R. Cohen, B Brauer, E. Nir, L. Grace, *Resonance-enhanced multiphoton ionization spectroscopy of dipeptides*, **2000**, *Phys. Chem.*, A, Vol. 104, No. 27.
17. R.E. Cohen, H. Krakauer, *Origin of ferroelectricity in perovskite oxides*, **1992**, *ferroelectrics*, 136, 95.
18. D. Damjanovic, *Hysteresis in piezoelectric and ferroelectric materials*, **2006**, *The science of hysteresis*, Elsevier, Volume 3, Chapter 4.
19. I. Sterianou *Bismuth-based perovskites for high temperature piezoelectric applications* **2008**, Ph.D. Thesis, University of Sheffield.
20. S. Stemmer, S.K. Streiffer, F. Ernst and M.Ruhle, *Atomistic structure of 90° domain walls in ferroelectric $PbTiO_3$ thin films*, **1995**, *Phil. Mag.* A71, 713-724.
21. M. Foeth, A. Sfeta, P. Stadelmann and P.A. Buffat, *A comparison of HREM and weak beam transmission electron microscopy for the quantitative measurement*

- of the thickness of ferroelectric domain walls*, **1999**, J. Electron. Microsc., 48, 717-723.
22. M. E. Caspari and W. J. Merz, *The electromechanical behaviour of BaTiO₃ single-domain crystals*, **1950**, Phys. Rev., 80, 1082-1089.
23. B. Bhushan, A. Basumallick, S.K. Bandopadhyay, N.Y. Vasanthacharya, D. Das *Effect of alkaline earth metal doping on thermal, optical, magnetic and dielectric properties of BiFeO₃ nanoparticles*, **2009**, J. Appl. Phys., 42, 065004.
24. G.A. Smolensky, A. I. Arganovskaya, V.A. Isupov, *Raman scattering in ordered and disordered perovskite type crystals*, **1959** Sov. Phys. Solid State, 1, 149.
25. Y. Benfang, L. Meiya, J. Liu, D. Guo, L. Pei, X. Zhao, *Effects of ion doping at different sites on electrical properties of multiferroic BiFeO₃ ceramics* 2008 J. Appl. Phys. 41, 065003
26. C.F. Chung, J.P. Lin, J.M. Wu *Influence of Mn and Nb dopants on electric properties of chemical-solution-deposited BiFeO₃ films*, **2006** J. Appl. Phys., 88, 242909.
27. R.H. Mitchell *Perovskites: modern and ancient*, **2002**, Almaz Press, Ontario, Canada.
28. N.B. Gharb, *Dielectric and piezoelectric nonlinearities in Pb(Yb_{1/2}Nb_{1/2})O₃-PbTiO₃ thin films*, **2007**, PhD thesis, University of Pennsylvania.
29. J. Knudsen, *Structure-property relations at the antiferroelectric/ferroelectric phase boundary in undoped and la doped Pb(Zr,Ti)O*, **2004**, PhD thesis, University of Sheffiled.
30. V.M. Goldschmidt, *Geochemische verteilungsgesetze der elemente*, **1926**, Skrifter utg. Av det Norske Viedenskaps-akademi i Oslo, **2**, 1-117.
31. D.I. Woodward, *The crystal chemistry of bismuth-based perovskite solid solutions*, **2004**, Ph.D. Thesis, University of Sheffield.
32. I.M. Reaney, E.L. Colla, N. Setter, *Dielectric and structural characteristics of Ba-based and Sr-based complex perovskites as a function of tolerance factor*, **1994**, Japanese journal of App. Phys., 33, 7A, 3984.

33. A. M. Glazer, *The classification of tilted octahedral in perovskites*, **1972**, Acta. Cryst., B28, 3384.
34. I.M. Reaney, *Superlattices in perovskites and related materials*, **1996**, Proc. Electroceram. V, Portugal, 441-46.
35. P. Fischer, M. Polomska, I. Sosnowska, M Szymanski *Temperature dependence of the crystal and magnetic structures of BiFeO₃*, **1980**, J. Phys., 13, 1931-40.
36. F. Kubel, H. Schmid *Structure of a ferroelectric and ferroelastic monodomain crystal of the perovskite BiFeO₃*, **1990**, Acta crystaller., Sect B, 46, 698.
37. I. Sosnowska, T. Peterlin-Neumaier, E. Steichele *Spiral magnetic ordering in bismuth ferrite*, **1982**, J. Phys. C: Solid State Phys., 15, 4835-46.
38. B.J. Neaton, C. Ederer, U.V. Waghmare, N.A. Spaldin, K.M. Rabe *First principle study of spontaneous polarization in multiferroic BiFeO₃*, **2005**, Phys. Rev. B: Condensed Matt. Mat. Phys., 71, 014113-8.
39. T. Zhao, A. Scholl, F. Zavaliche, K. Lee, M. Barry, A. Doran, M. P. Cruz, Y.H. Chu, C. Ederer, N.A. Spaldin, R.R. Das, D.M. Kim, S.H.Baek, C.B.Eom, R. Ramesh *Electrical control of antiferromagnetic domains in multiferroic BiFeO₃ films at room temperature*, **2006**, nature material, Vol 5, 823-829.
40. D.C. Arnold, K.S. Knight, F.D. Morrison, *Ferroelectric-paraelectric transition in BiFeO₃: crystal structure of the orthorhombic beta phase*, **2009**, Phys. Rev. B., 102, 027602.
41. F. Kubel, H. Schmid, *Structure of a ferroelectric and ferroelastic monodomain crystal of the perovskite BiFeO₃*, **1990**, Acta crystaller., Sect B, 46, 698.
42. J. R. Teague, R. Gerson and W. J. James, *Dielectric hysteresis in single crystal BiFeO₃*, **1970**, Solid State Commu., 8, 13, 1073.
43. R.D. King-smith, D. Vanderbilt *Theory of polarization of crystalline solids*, **1993**, Physical review, B, 47, 1651-54.
44. R.D. King-Smith, D. Vanderbilt, *First-principles investigation of ferroelectricity in perovskite compounds*, **1994**, Physical review, B, 49, 5828-44.

45. R. Resta, *Piezoelectricity: Evolution and future of a technology*, **1994**, Mod. Phys., 66, 899.
46. P. Fischer, M. Polomska, I. Sosnowska, M. Szymanski, *Temperature dependence of the crystal and magnetic structures of BiFeO₃*, **1980**, J. Phys. C: Solid State Phys., 13, 1931-40.
47. I. Sosnowska, R. Prezenioslo, P. Fischer, V.A. Murashov, *Neutron diffraction studies of the crystal and magnetic structure of BiFeO₃ and Bi_{0.93}La_{0.07}FeO₃*, **1996**, J. Magn. Magn. Mat., 160, 384-5.
48. B.J. Neaton, C. Ederer, U.V. Waghmare, N.A. Spaldin, K.M. Rabe, *First principle study of spontaneous polarization in multiferroic BiFeO₃*, **2005**, Phys. Rev. B: Condensed Matt. Mat. Phys., 71, 014113-8.
49. G. A. Smolenski and V. M. Yudin, *Weak ferromagnetism of some BiFeO₃-PB(Fe_{0.5}Nb_{0.5})O₃ Perovskites*, **1965**, Soviet Phys. Solid State, 6, 12, 2936.
50. I. Sosnowska, T. Peterlinneumaier, E. Steichele, *Spiral magnetic-ordering in bismuth ferrite*, **1982**, Journal of Phys. C-solid State phys., 15, 23, 4835-4846.
51. M. Fiebig *Revival of the magnetoelectric effect*, **2005**, J. Phys. D, **38**, R123.
52. V.A. Khomchenko, D.A. Kiselev, J.M. Vieira, L. Jian, A.L. Kholkin, A.M.L. Lopes, Y.G. Pogorelov, J.P. Araujo, M. Maglione *Effect of diamagnetic Ca, Sr, Pb, and Ba substitution on the crystal structure and multiferroic properties of the BiFeO₃ perovskite*, **2008**, J. App. Phys., 103, 024105.
53. S. Karimi, I.M Reaney, I. Levin, I. Sterianou *Nd-doped BiFeO₃ ceramics with antipolar order*, **2009**, App. Phys. Lett., 94, 112903(52).
54. M.M. Kumar, V.R. Palkar, K. Srinivas, S.V. Suryanarayana, *Ferroelectricity in pure BiFeO₃ ceramic*, **2000**, Appl. Phys. Lett., 76(19), 2764-66.
55. A.K. Pradhan, K. Zhang, D. Hunter, J.B. Dadson, G.B. Loutts, P. Bhattacharya, R. Katiyar, J. Zhang, D.J. Sellmyer, *Magnetic and electrical properties of single-phase multiferroic BiFeO₃*, **2005**, J. Appl. Phys., 97, 093903.

56. S. Karimi, I.M. Reaney, Y. Han, J. Pokorny, I. Sterianou, *Crystal chemistry and domain structure of rare-earth doped BiFeO₃ ceramics*, **2009**, J. Mater Sci, 10853-009-3545-1.
57. D. Maurya, H. Thota, A. Garg, B. Panday, P. Chand, H.C., *Verma magnetic studies of multiferroic Bi_{1-x}Sm_xFeO₃ ceramics synthesized by mechanical activation assisted processes* **2009**, J.Phys: Condens, Matter 21, 026007.
58. C. Fanggo, S. Guilin, F. Kun, Q. Ping, Z. Qijun, *Effect of Gadolinium substitution on dielectric properties of bismuth ferrite*, **2006**, Journal of rare earths, Vol 24, 273.
59. W. Slawinski, R. Przenioslo, I. Sosnowska and E. Suard, *Spin reorientation and structural changes in NdFeO₃*, **2005**, J. Phys. Condens. Matter., 17, 2605.
60. M.K. Singh, H.M. Jang, H.C. Gupta, R.S. Katiyar, *Polarized raman scattering and lattice eigenmodes of antiferromagnetic NdFeO₃*, **2008**, J. Raman Spectrosc., 39, 842-48.
61. S.A. Ivanov, P. Nordblad, R. Tellgren, T. Ericsson, S.K. Korchagina, L.F. Rybakova, A. Hewat, *Influence of PbZrO₃ doping on the structural and magnetic properties of BiFeO₃*, **2008**, solid state sciences, 10, 1875-85.
62. B. Yu, M. Li, J. Wang, L. Pei, D. Guo, X. Zhao, *Enhanced electrical properties in multiferroic BiFeO₃ ceramics co-doped by La³⁺ and V⁵⁺*, **2008**, J. Appl. Phys., 41, 185401.
63. C. J. Cheng, D.Kan, S. H. Lim, W. R. McKenzie, P. R. Munroe, L. G. Salamanca-Riba, R. L. Withers, I. Takeuchi and V. Nagarajan, *Structural transitions and complex domain structures across a ferroelectric-to-antiferroelectric phase boundary in epitaxial Sm-doped BiFeO₃ thin films*, **2009**, Phys Rev B., 80, 014109.
64. G.D. Hu, X. Cheng, W.B. Wu, C.H. Yang, *Effects of Gd substitution on structure and ferroelectric properties of BiFeO₃ thin films prepared using metal organic decomposition*, **2007**, App. Phys. Lett., 91, 232909.

65. B. Yu, M. Li, J. Wang, L. Pei, D. Guo, X. Zhao, *Enhanced electrical properties in multiferroic BiFeO₃ ceramics co-doped by La³⁺ and V⁵⁺*, **2008**, *J. Appl. Phys.*, 41, 185401.
66. Y. K. Jun, W. T. Moon, C. M. Chang, H. S. Kim, H. S. Ryu, J. W. Kim, S. H. Hong, *Effects of Nb-doping on electric and magnetic properties in multi-ferroic BiFeO₃ ceramics*, **2005**, 135, 133-137.
67. K. Abe, N. Sakai, J. Takahashi, H. Itoh, N. Adachi, and T. Ota, *Leakage current properties of cation-substituted BiFeO₃ ceramics*, **2010**, *Jpn. J. Appl. Phys.*, 49, 09MB01.

Chapter 3: Experimental Procedures

3.1. Ceramic Processing

3.1.1 Calcination

Compositions of $\text{Bi}_{0.85}\text{Nd}_{0.15}\text{Fe}_{1-y}\text{Ti}_y\text{O}_3$ ($y = 0, 0.01, 0.03, 0.05$ and 0.1) and $\text{Bi}_{1-x}\text{Nd}_x\text{Fe}_{0.97}\text{Ti}_{0.03}\text{O}_3$ ($x = 0, 0.1, 0.115, 0.125, 0.15, 0.175, 0.2, 0.25$) were produced using Bi_2O_3 (99.9 %, Acros Organics), Fe_2O_3 (99.8 %, Alfa Aesar), TiO_2 (99.99 %, Sigma Aldrich) and Nd_2O_3 (99.90 %, Sigma Aldrich) as the starting materials. Stoichiometric amounts of dry raw materials based on the compositions in Table 3.1 were weighed and attrition milled for 1 hour with yttria-stabilised zirconia (YSZ) media in iso-propanol. Mixed powders were calcined at the optimum reaction temperature, Table 3.1, for 3 hours in an alumina crucible. The optimum reaction temperature was determined as the lowest temperature at which only the perovskite phase was present by X-ray diffraction or when the least amount of secondary phase was present. The reacted powder was sieved through a 355 μm sieve and then attrition milled as above.

For compositions which did not give perovskite phase or which showed evidence of broad peaks typical of poorly reacted powders, two different approaches were followed, namely, double calcination and premilling of Nd_2O_3 . For double calcined compositions, further heat treatment at the reaction temperature was carried out followed by attrition milling to improve homogeneity and promote a greater volume fraction of the desired phase [1]. Upon examination of the Nd_2O_3 raw powder using a particle sizer and scanning electron microscope, it was noted that its average particle size was greater than that of other precursor materials. In addition, Nd_2O_3 is the most refractory raw material to be used in these reactions. To encourage a more homogeneous distribution,

the Nd_2O_3 raw material was pre-milled for 1h prior to batching. The relative benefits of these two approaches will be discussed in chapter 4.

3.1.2. Particle Size Analysis (PSA)

Particle Size Analysis (PSA) was performed on the raw materials, mixed precursors and calcined powders immediately prior to pellet formation. Size distribution profiles for each sample were determined by a Coulter LS130 laser particle size analyser (Beckman Coulter Ltd., High Wycombe, Bucks, UK).

Less than a gram of sample was placed on a watch glass and then an aqueous solution containing 5% by volume of Dispex N40 (Allied Colloids Group PLC, Bradford, UK) was added and stirred. The mixture was placed in an ultrasonic bath for a few minutes. The sample was added to the particle size analyser with a pipette until the particle concentration was deemed appropriate by the automatic control. Each 90 second run was followed by addition of 20 ml deflocculant (containing 5% by volume Dispex N40). Deflocculant breaks up the agglomerates and a more accurate distribution is achieved.

3.1.3. Pelletisation

Powder was pressed into pellets of 10 mm diameter and ~2.5 mm thickness by uniaxial pressing at an applied load of 1 tonne for 1 minute. Pellets were then placed in an alumina boat covered with Pt foil to avoid reaction and sintered in air at an optimum sintering temperature for 3 hours. The optimum sintering temperature was judged to be that at which the proportion of secondary phases was minimal and density > 95% theoretical.

3.1.4. Density Measurement

Pellets were weighed on a Salter A&D ER-120A electronic balance (Tokyo, Japan) to an accuracy of 0.0001 g (W_1). A thin piece of string was tied around the pellet. This was then suspended from an Oertling R20 (London, UK) mechanical balance and reweighed (W_2) to the same accuracy. The tied sample was then immersed into a beaker

containing water and the reading of the balance was taken, W_3 . The decrease in weight is the upthrust due to the water displaced. The water temperature was recorded. The bulk density of the sintered pellets was measured based on the Archimedes principle using the equation below:

$$\rho_{\text{bulk}} = \rho_{\text{H}_2\text{O}} \times W_1 / (W_2 - W_3) \quad (3.1)$$

The principle of this method is that the difference between weights W_2 and W_3 is equal to the mass of water displaced by the pellet. Water density may be determined from its temperature and consequently the volume of the pellet is accurately determined.

Table 3.1: Starting compositions along with their processing conditions. (NB. No attempt was made to adjust the Bi concentration to compensate for donor doping).

General Formula: $\text{Bi}_{1-x}\text{Nd}_x\text{Fe}_{1-y}\text{Ti}_y\text{O}_3$				x = 0.15 y = 0 880 °C(double) 920 °C			
				x = 0.15 y = 0.01 900 °C(double) 940 °C			
x = 0 y = 0.03 900 °C 940 °C Nd ₂ O ₃ - premilled	x = 0.1 y = 0.03 960 °C 990 °C Nd ₂ O ₃ - premilled	x = 0.115 y = 0.03 960 °C 990 °C Nd ₂ O ₃ - premilled	x = 0.125 y = 0.03 960 °C(both) 990 °C Nd ₂ O ₃ - premilled	x = 0.15 y = 0.03 960 °C 990 °C Both	x = 0.175 y = 0.03 960 °C 990 °C Nd ₂ O ₃ - premilled	x = 0.2 y = 0.03 960 °C 990 °C Nd ₂ O ₃ - premilled	x = 0.25 y = 0.03 960 °C 990 °C Nd ₂ O ₃ - premilled
Nd doping level Ti doping level Calcination Temperature Sintering Temperature				x = 0.15 y = 0.05 990 °C(double) 1020 °C			
				x = 0.15 y = 0.1 1020 °C(double) 1050 °C			

3.2. Structural and Microstructural Characterisation

3.2.1. X-Ray Diffraction (XRD)

XRD was performed on raw materials, calcined powders and crushed pellets. Either calcined powder or crushed and ground pellets were placed on an aluminium holder and flattened using a glass slide.

A Siemens D500 diffractometer was utilised with $\text{CuK}\alpha$ ($\lambda = 1.5418\text{\AA}$) radiation. Diffractograms were collected in the range 10 to 70 degrees 2θ with a step size of 0.02° , at $1^\circ/\text{min}$. For crushed pellets longer scans were also performed (at $0.1^\circ/\text{min}$). The subsequent data were formatted and analysed using the 'WinXPow' software.

3.2.2. Differential Scanning Calorimetry (DSC)

Differential Scanning Calorimetry (DSC) is a thermoanalytical technique in which the difference in the amount of heat required to raise the temperature of a sample and reference is measured as a function of temperature. Note that both sample and reference are kept at a same temperature during the experiment. The technique was developed by E.S. Watson and M. J. O'Neil in 1962 [3].

Differential scanning calorimetry was performed using a Netzch DSC 404 C Pegasus which was controlled by Netzsh Proteus software. Each measurement was carried out twice with the second considered as accurate so as to avoid anomalies associated with adsorbed volatiles. Heating and cooling were carried out at $10^\circ\text{C min}^{-1}$ rate.

3.2.3. Dilatometry

A Dilatometer is a scientific instrument that measures volume changes caused by a physical or/and chemical transformation. The pellets prepared for dilatometry were cylindrical with a thickness more than 5 mm. The samples were then inserted in the furnace of a connecting rod (push rod) dilatometer (NETZSCH DIL 402 C). A

connecting rod transfers the thermal expansion to a strain gauge, which measures the shift. The data were then stored in the controller (TASC 414/4). Dilatometry was performed from 20 °C to 700°C with a heating rate of 10 °C min⁻¹.

3.2.4. Scanning Electron Microscopy (SEM)

Scanning electron microscopy (SEM) was performed on the raw materials and the final sintered pellets. The raw materials were prepared for SEM by scattering a small amount of powder over a sticky carbon pad, fixed to an aluminium stub. Excess powder was knocked off and the stub was carbon coated.

Backscattered and secondary electron images were also obtained from the fracture surface of pellets. Samples were mounted on Al stubs and were carbon coated to prevent charging. The microscope (Camscan, 20 kV and JEOL JSM-6400, 15 kV) was equipped with a Link analytical energy dispersive spectroscopy (EDS) X-ray detector (Link Analytical Ltd., High Wycombe, Bucks, UK), which was used to collect spectra. An accelerating voltage of 20 kV and a spot size of 6 Å was used in this procedure. To obtain qualitative chemical analysis of the sample, spectra were processed using LINK ISIS software. No attempt was made to use standards other than within the link ISIS software. The estimated error on all data was ±2% which arose due to errors in counting statistics and profile fitting.

3.2.5. Transmission Electron Microscopy (TEM)

Transmission Electron Microscopy (TEM) was utilized to study grain and domain morphologies as well as to obtain electron diffraction patterns along principal zone axes to aid in the determination of symmetry. In TEM, a beam of electrons is transmitted through an ultra thin specimen. The resulting image is then magnified and focused onto a Charge Channel Display (CCD) camera. The first TEM was built by Max Knoll and Ernst Ruska in 1931 [4].

Specimens were prepared by mounting on a Gatan Disc Grinder and grinding the samples using silicon carbide paper to a thickness of < 40 µm. The samples were then glued (Epoxy resin, Wellingbrough, UK) to a 3 mm copper support ring. The samples

were milled to perforation by a GATAN dual ion mill 600 model (Pleasanton, California, USA). The ion mill was operated using a 6 kV accelerating voltage, at a combined gun current of 0.6 mA, with an incidence angle of between 10° to 15°. The samples were carbon coated with an Edwards 'Speedivac' model 12E6/1598 coating unit (Crawley, UK) prior to examination using a Philips EM420T (Eindhoven, Netherlands) microscope operating at 120 kV.

3.2.6. Raman Spectroscopy

Raman spectroscopy (Raman) is a spectroscopic technique that relies on inelastic scattering or Raman scattering of monochromatic light, usually from a laser in the visible range. The laser light interacts with molecular vibrations or other excitations in the system such as phonons, resulting in the energy of the laser photons being shifted up or down. The shift in the energy gives information about the vibrational modes in the system [5].

Unpolarised Raman spectra were excited with the 514.5 nm line of an Ar laser and recorded in back scattering geometry using a Renishaw InVia micro-Raman spectrometer. Laser power of 15 mW was focused on a $\sim 2 \mu\text{m}$ spot. The spectral resolution was $\sim 1 \text{ cm}^{-1}$. Raman spectra were obtained from various samples fabricated under different sintering conditions. In addition, spectra were recorded from several points on the ceramic surface to ensure maximum precision possible.

3.3 Electrical Characterisation

3.3.1. Dielectric Measurement

The surfaces of the disc-shaped pellets were coated with gold paste (T-10112, Metalor Technologies UK Ltd., Birmingham, UK) and sintered at 800 °C for 2 hours. An inductance/capacitance/resistance (LCR) meter (Model 4284A, Hewlett Packard) linked to a computer via a GP-IB interface was used for measurements of capacitance and $\tan \delta$, at different fixed frequencies with an ac signal amplitude of 100 mV. Pellets were heated at 1 °C/min up to 650 °C in a tube furnace with the temperature, $\tan \delta$ and

capacitance measured every 60 seconds. The following formula was used to convert capacitance to permittivity:

$$\varepsilon_r = \frac{C}{\varepsilon_0} \cdot \frac{t}{A} \quad (3.2)$$

C : capacitance (F)

t : thickness of the sample (m)

A : area of face of the pellet (m²)

ε_0 : permittivity of free space, 8.854×10^{-12} (F/m)

ε_r : relative permittivity

3.3.2. Impedance Spectroscopy (IS)

In this technique, variable frequency measurement investigates the electrical properties of materials. The main advantage is the ability to identify the electrical homogeneity of sample since different frequency ranges can highlight different regions of the sample. The general method of IS involves the application of a known alternating potential (ac) difference across the material and observing the response. The frequency range is typically 10^0 to 10^7 Hz. Controllable variables such as temperature and oxygen partial pressure can be altered during an experiment to help determine the physical origin(s) of the electrical properties. Finally an equivalent circuit can be constructed in order to interpret and analyse the data.

A resistor (R) and a capacitor (C) linked in parallel is the most common equivalent circuit for each electrically distinct region of an electroceramic [2]. Additional RC elements are added in series to model two or more electrically distinct regions.

The samples were prepared in the same manner as for LCR measurements. They were loaded in a conductivity jig and placed into a tube furnace. A Solartron SI

1260 Impedance analyser and a SI 1296 Dielectric Interface (Farnborough, UK) were used to take measurements in the frequency range 0.01 to 1 MHz. The amplitude of the applied signal was 100 mV and data were corrected for sample geometry and analysed using ZView software (Scribner Associates Inc, USA).

3.3.3. Polarisation- Electric Field Measurement

Room temperature polarisation-field (P-E) hysteresis loops were generated using an RT66A standardized ferroelectric test system (Radiant Technologies) operated in virtual ground mode coupled to a TREK high voltage amplifier (Model 609E-6). Since the voltage amplifier has a limitation of 4 kV, the pellets were thinned down to less than 1 mm, to achieve a sufficiently high electric field. Partial electrodes (diameter of 5mm) were applied on one side in order to discourage short circuiting. Electrodes were applied in the same manner as for LCR measurements. The samples were placed in a holder and immersed in silicone oil. The specimen was subjected to a cyclic electric field using a triangular waveform with a frequency of 6 Hz. The area of partial electrode was considered in P-E measurements. Consequently, the non-linear field would not be measured. The error would be negligible since the samples are thin (less than 1 mm).

3.3.4. Piezoresponse Force Microscopy (PFM)

Piezoresponse force microscopy (PFM) is a variant of atomic force microscopy that allows imaging and manipulation of ferroelectric domains by bringing a sharp conductive probe into contact with a ferroelectric or piezoelectric surface and applying alternating current (AC) bias to the probe tip in order to excite deformation of the sample through the converse piezoelectric effect. The resulting deflection of the probe cantilever is detected through standard split photodiode detector methods and then demodulated by use of a lock-in amplifier (LiA). In this way topography and ferroelectric domains can be imaged simultaneously with high resolution [6, 7]. In addition to imaging domains, application of a high voltage bias through the tip may result in switching of the local polarisation and thus in the ideal case domain wall dynamics may be studied. There

are two possible modes of imaging in PFM, one analyses the in-plane and the other the out-of-plane piezoresponse [8].

References

1. V.V. Shvartsman, W. Kleemann, R. Haumont and J. Kreisel, *Large bulk polarization and regular domain structure in ceramic BiFeO₃*, **2007**, App. Phys. Lett., 90, 172115.
2. J.T.S. Irvine, D.C. Sinclair and A.R. West, *Electroceramics: characterization by impedance spectroscopy*, **1990**, Adv. Mater., 2, 132-138
3. E. S. Watson, R. J. O'Neil and M. J. O'Neil, *Differential Microcalorimeter*, **1966**, United States patent office, Ser. No. 185,499.
4. E. Ruska, *The early development of electron lenses and electron microscopy*, **1931**, ISBN 3-7776-0364-3.
5. D. J. Gardiner, *Practical raman spectroscopy*, **1989**, Springer-Verlag, ISBN 978-0387502540.
6. A. Gruverman, *Domain structure and polarisation reversal in ferroelectrics studied by atomic force microscopy*, **1995**, J. Vac. Sci. Tech. B., 13, 1095.
7. S.V. Kalinin, A.N. Morozovska, L. Chen, B.J. Rodriguez, *Local polarization dynamics in ferroelectric materials*, **2010**, Reports on progress in Physics, 73, 056502.
8. S.V. Kalinin, B.J. Rodriguez, S. Jesse, J. Shin, A.P. Baddorf, P. Gupta, H. Jain, D. Williams, *Vector piezoresponse of microscopy*, **2006**, Microscopy society of America, 12, 206-220.

Chapter 4: Raw Materials and Processing

4.1. Raw materials characterisation

4.1.1. Bismuth (III) Oxide, Bi_2O_3

Arcos Organics (Geel, Belgium) supplied the bismuth oxide, purity 99.9%. Bismuth oxide is the most industrially important compound of bismuth and may be extracted from the natural mineral 'bismite'. It is also obtained as a by-product of smelting copper and lead ores. The XRD trace is indexed according to $\alpha\text{-Bi}_2\text{O}_3$ (ICDD card [41- 1449]), Figure 4.1. No secondary phases were observed in SEM images, Figure 4.2.

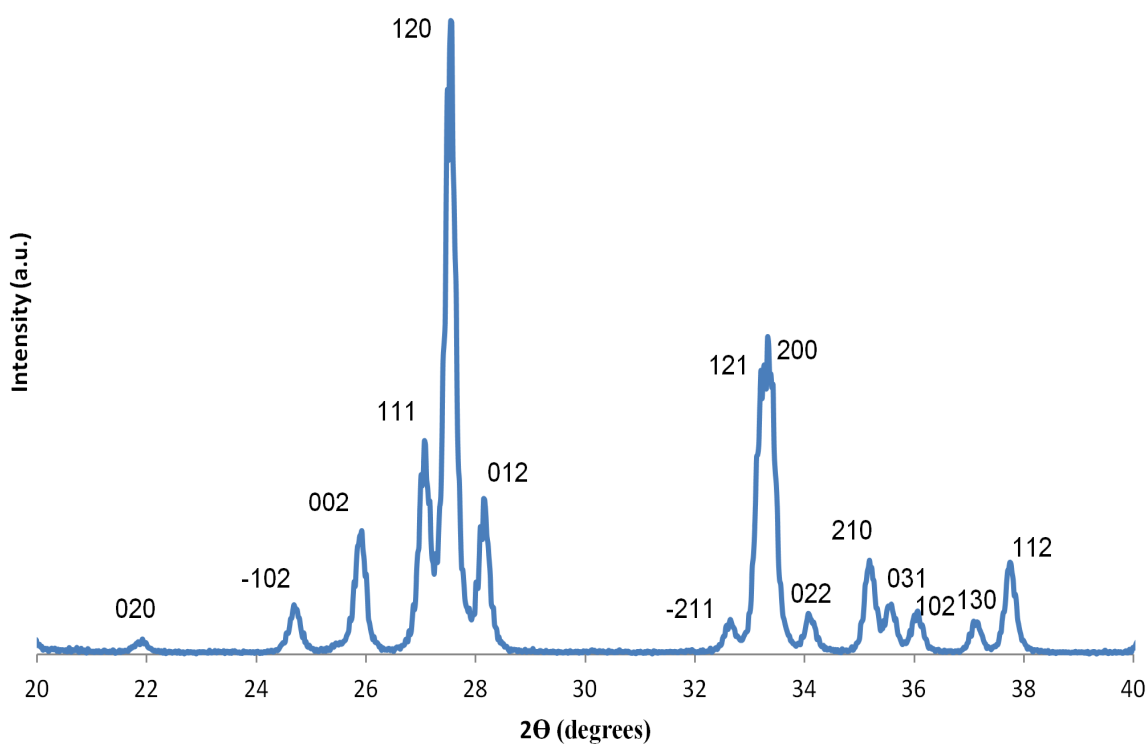


Figure 4.1: XRD trace of Bi_2O_3 .

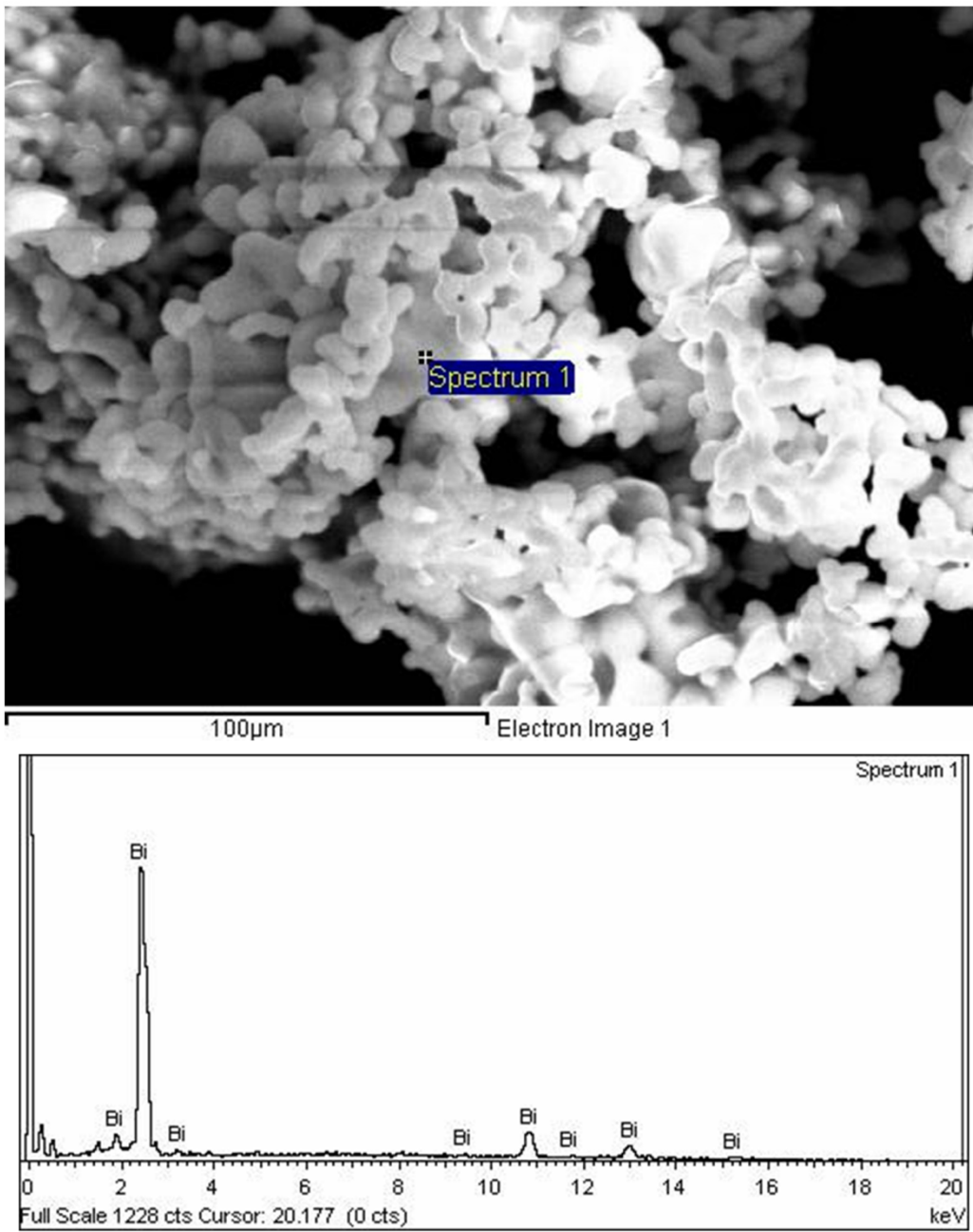


Figure 4.2: SEM image and EDS trace of Bi_2O_3 .

4.1.2. Iron (III) Oxide, Fe₂O₃

Alfa Aesar (Massachusetts, USA) supplied iron oxide with +99% purity. There are three hundred known iron oxides and hydroxides [1]. Fe₂O₃ is one of the three main oxides and is known as ‘hematite’. XRD peaks are indexed according to rhombohedral Fe₂O₃ (ICDD card [33- 664]), Figure 4.3. No secondary phases were observed in SEM images, Figure 4.4.

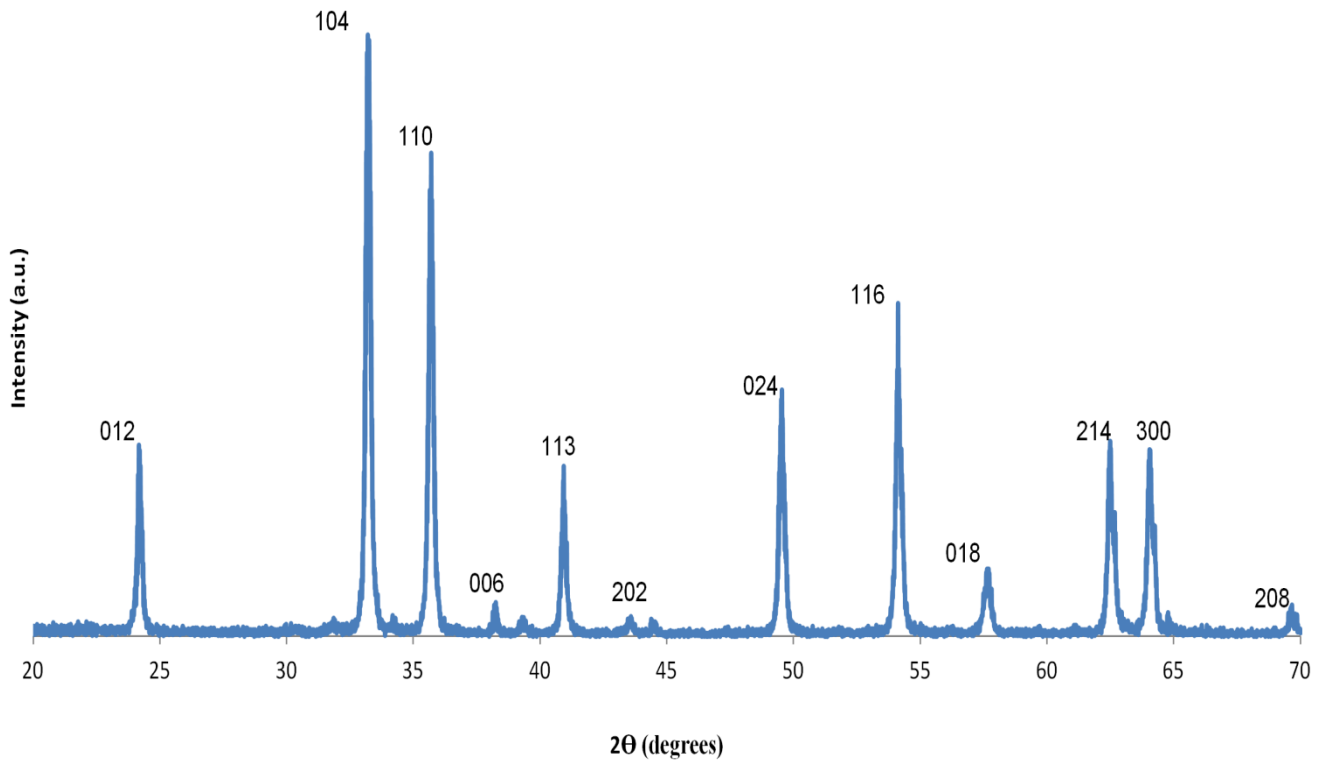


Figure 4.3: XRD trace of Fe₂O₃.

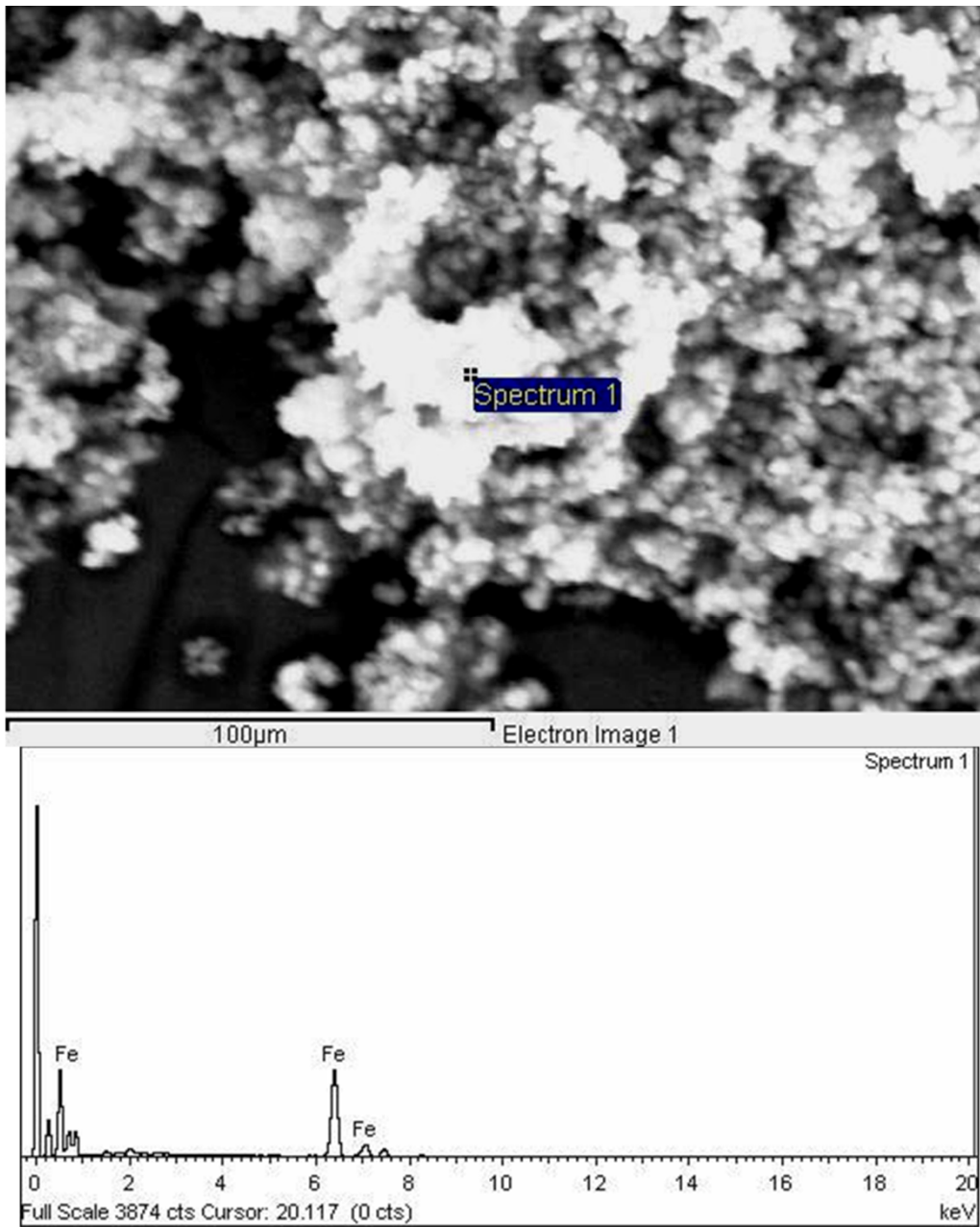


Figure 4.4: SEM image and EDS trace of Fe_2O_3 .

4.1.3. Neodymium Oxide, Nd_2O_3

Sigma-Aldrich Company Ltd (Dorset, UK) supplied Nd_2O_3 with purity 99.90%. Nd_2O_3 appears as light blue hexagonal shaped crystals. XRD peaks are indexed according to hexagonal Nd_2O_3 (ICDD card [65- 3184]), Figure 4.5. No secondary phases were observed in SEM images, Figure 4.6.

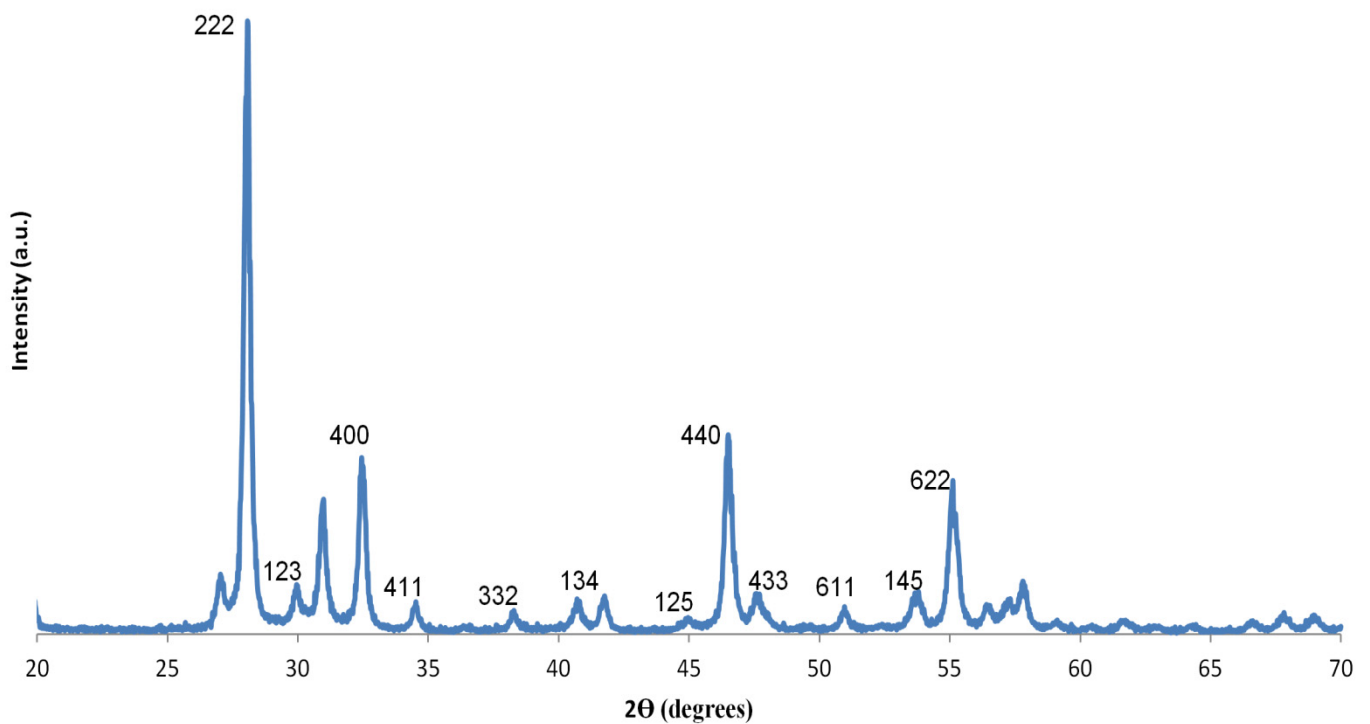


Figure 4.5: XRD trace of Nd_2O_3 .

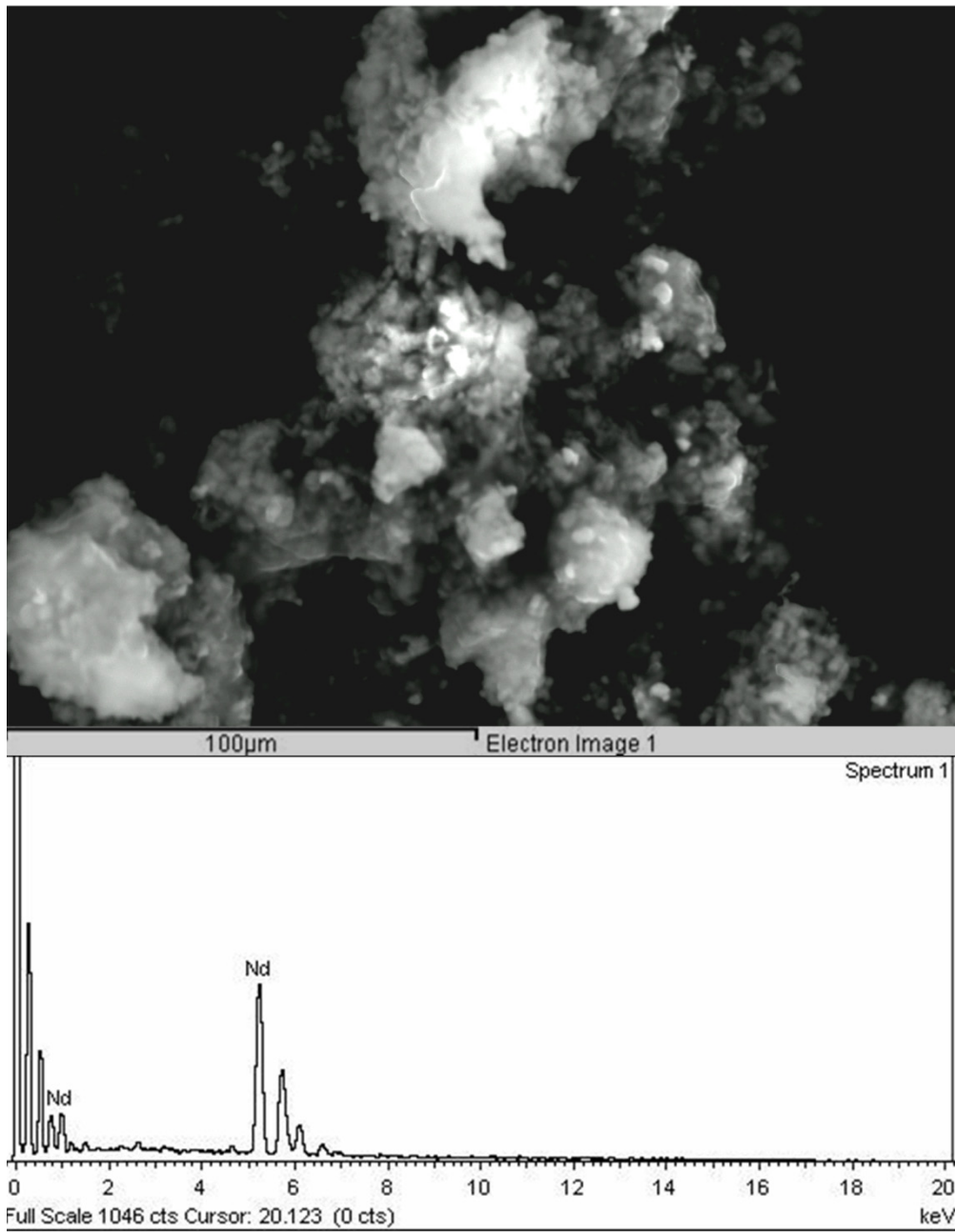


Figure 4.6: SEM image and EDS trace of Nd_2O_3 .

4.1.4. Titanium (IV) Oxide, TiO₂

Titanium oxide in the form of anatase with purity >99.9% was obtained from Sigma-Aldrich Company Ltd (Dorset, UK). XRD peaks are indexed according to TiO₂-anatase (ICDD card [21- 1272]), Figure 4.7. No secondary phases were observed in SEM images, Figure 4.8.

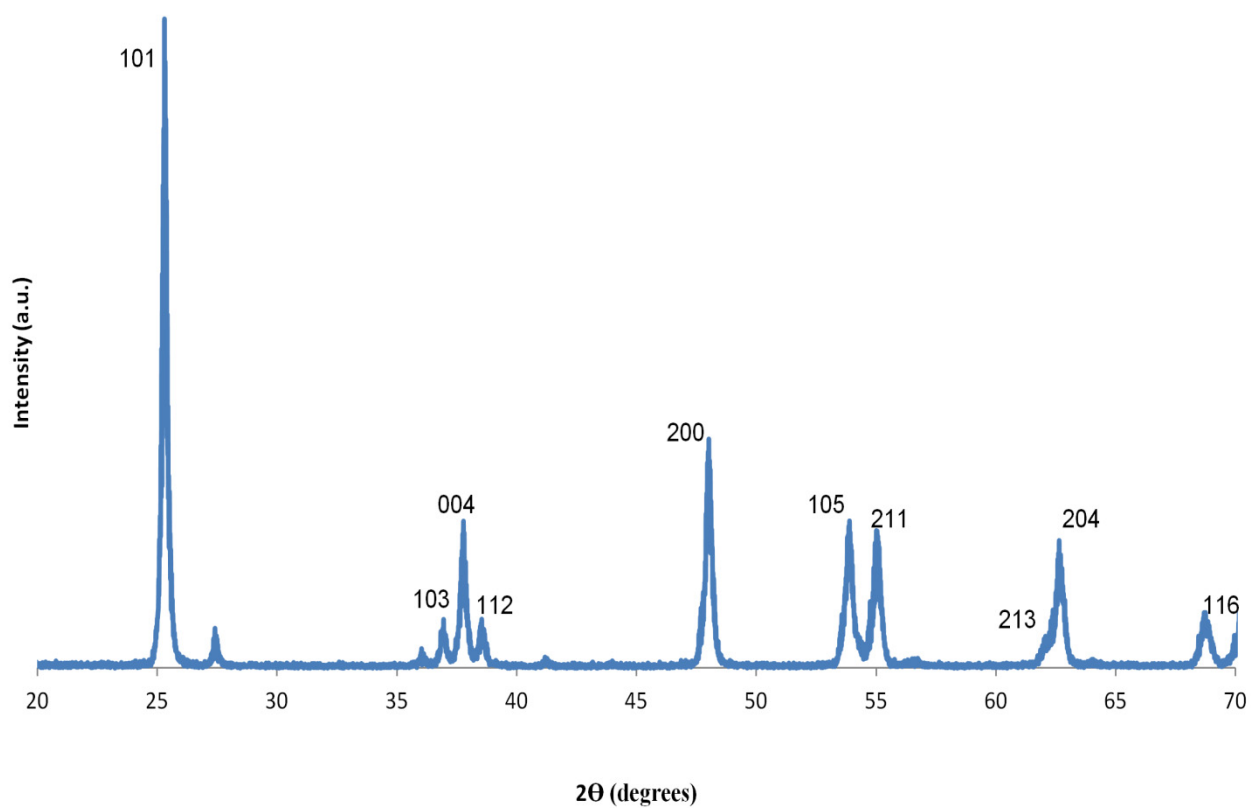


Figure 4.7: XRD trace of anatase, TiO₂.

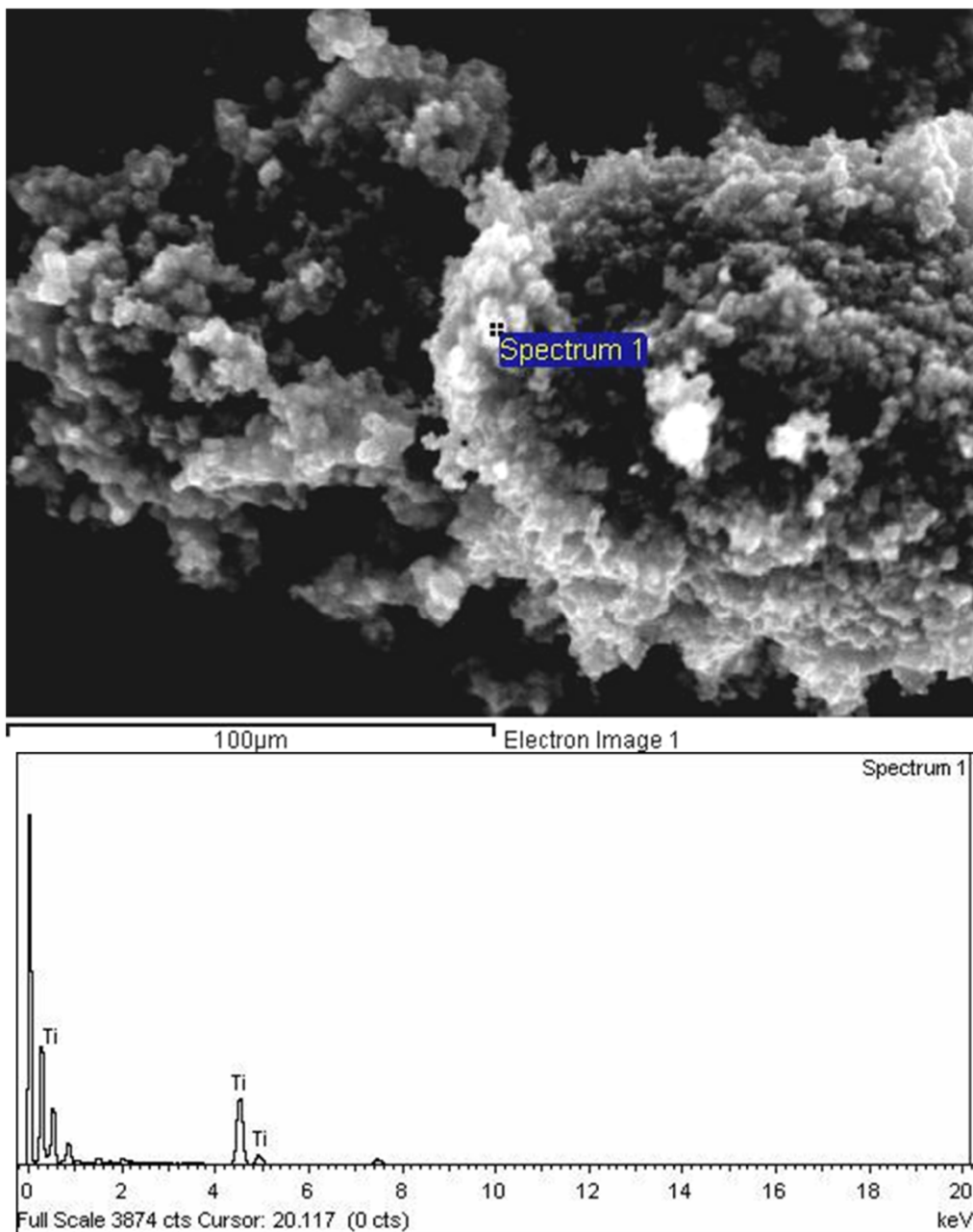


Figure 4.8: SEM image and EDS trace of anatase structured TiO_2 .

4.1.5. Particle size of Raw Materials

Plots of the particle size distributions of raw materials are shown in Figure 4.9. The mean particle size of bismuth oxide, titanium oxide and iron oxide is smaller ($< 3\mu\text{m}$) than Nd_2O_3 ($6\mu\text{m}$). All raw materials have agglomerates greater than the mean particle size but it is anticipated that agglomerates will break up during milling of the raw materials prior to calcination. Nd_2O_3 is also the most refractory of the oxides used in this study and hence it is critical for homogeneity that milling of the raw materials results in a smaller mean size. Figure 4.10 and Table 4.1 compare the mean particle sizes of the raw materials after pre-milling the Nd_2O_3 . The d_{50} value of Nd_2O_3 has been reduced to $< 2\mu\text{m}$.

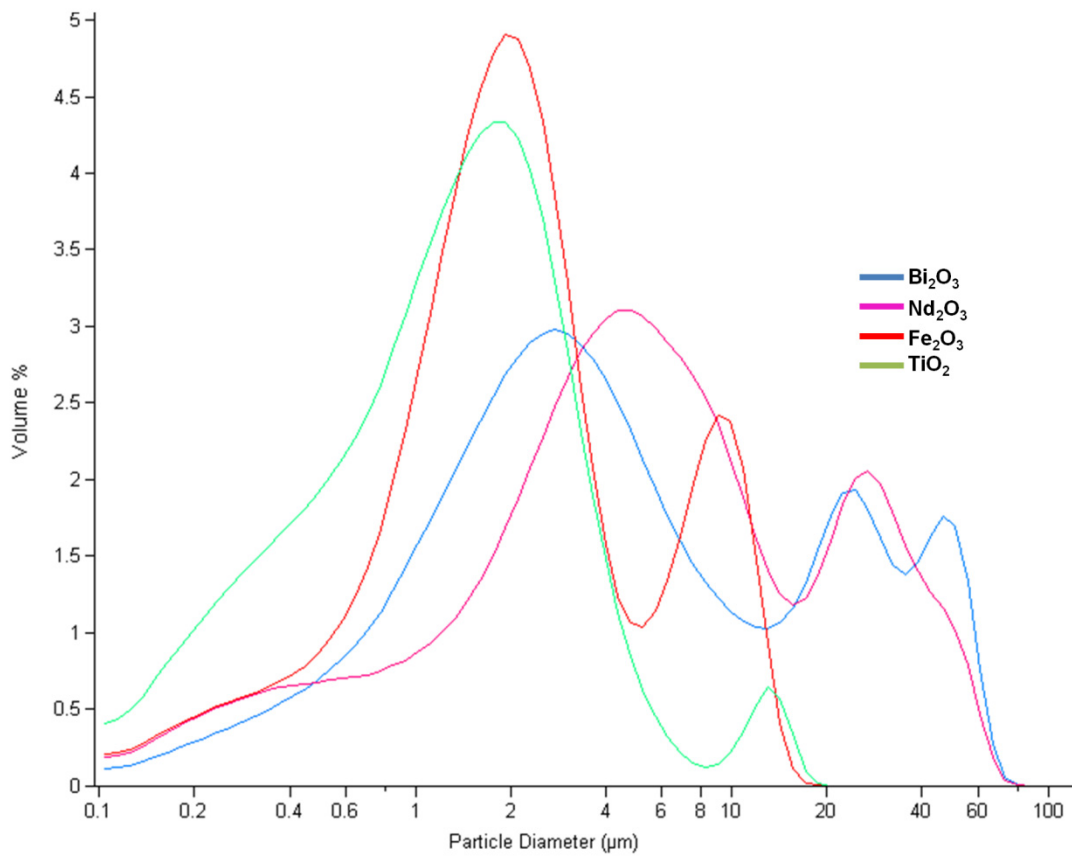


Figure 4.9: Particle size distribution curves of the raw materials.

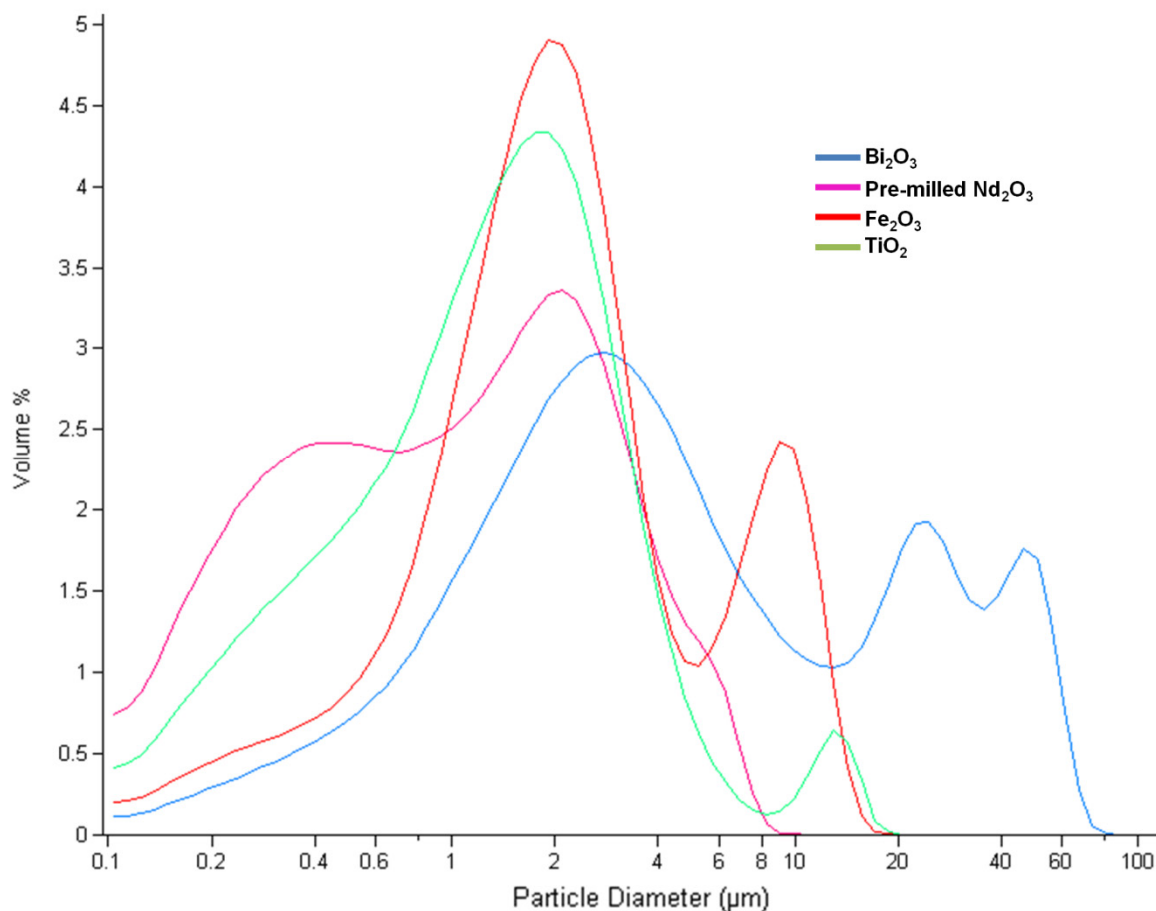


Figure 4.10: Precursor raw materials particle size of $\text{Bi}_{1-x}\text{Nd}_x\text{Fe}_{0.97}\text{Ti}_{0.03}\text{O}_3$ ($x = 0, 0.1, 0.115, 0.125, 0.15, 0.175, 0.2, \text{ and } 0.25$) powders.

Table 4.1: Various mean diameters of raw materials. The errors estimated at $\pm 0.01 \mu\text{m}$ which arose from inaccuracies in the calculation of the mean. These inaccuracies are considered to be far smaller than any sample to sample variation.

	Bi ₂ O ₃	Nd ₂ O ₃	Nd ₂ O ₃ (pre-milled)	Fe ₂ O ₃	TiO ₂
d ₁₀ (μm)	0.75	0.64	0.21	0.57	0.29
d ₂₅ (μm)	1.65	2.21	0.39	1.17	0.62
d ₅₀ (μm)	3.70	5.10	1.02	2.00	1.32
d ₇₅ (μm)	14.71	12.95	2.19	3.66	2.27
d ₉₀ (μm)	34.69	30.52	3.56	8.67	3.49

4.2. Powder processing

Figure 4.11 shows the particle sizes of mixed precursors measured after attrition milling (1h) the batched raw materials but before calcination. The particle size distributions are ideal for reaction with almost all particles (d₉₀) typically below 8 μm with no large agglomerates, Table 4.2.

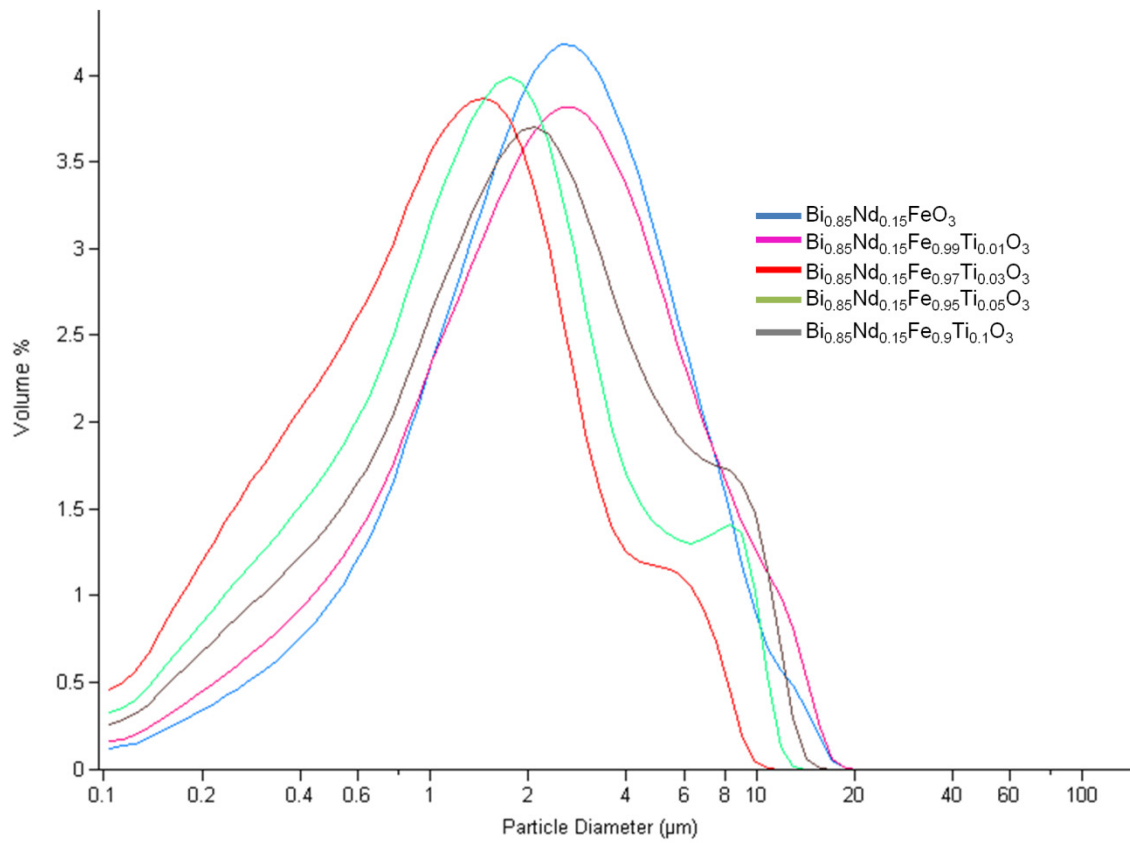


Figure 4.11: Examples of mixed precursor's particle size distributions after attrition milling for 1 hour.

Table 4.2: Particle diameters of mixed precursors after milling. Errors are estimated at $\pm 0.01 \mu\text{m}$, considerable less than batch to batch variation.

	$\text{Bi}_{0.85}\text{Nd}_{0.15}\text{FeO}_3$	$\text{Bi}_{0.85}\text{Nd}_{0.15}\text{Fe}_{0.99}\text{Ti}_{0.01}\text{O}_3$	$\text{Bi}_{0.85}\text{Nd}_{0.15}\text{Fe}_{0.97}\text{Ti}_{0.03}\text{O}_3$	$\text{Bi}_{0.85}\text{Nd}_{0.15}\text{Fe}_{0.95}\text{Ti}_{0.05}\text{O}_3$	$\text{Bi}_{0.85}\text{Nd}_{0.15}\text{Fe}_{0.9}\text{Ti}_{0.1}\text{O}_3$
$d_{10} (\mu\text{m})$	0.61	0.51	0.26	0.33	0.38
$d_{25} (\mu\text{m})$	1.22	1.11	0.52	0.71	0.88
$d_{50} (\mu\text{m})$	2.32	2.27	1.11	1.47	1.85
$d_{75} (\mu\text{m})$	4.09	4.22	2.04	2.70	3.62
$d_{90} (\mu\text{m})$	6.53	7.17	3.65	5.41	6.79

Prior to sintering all compositions were reacted to form the perovskite phase. In this study, the particle size of milled reacted powder depends on the calcination temperature, Figure 4.12. Reaction temperatures for the compositions are close to the melting temperature of the base material, BiFeO_3 , and consequently partial melting during reaction results in hard particulates difficult to break up during milling. The problem is best exemplified by comparing, e.g., $\text{Bi}_{0.85}\text{Nd}_{0.15}\text{FeO}_3$ (calcined at $880\text{ }^\circ\text{C}$) with $\text{Bi}_{0.85}\text{Nd}_{0.15}\text{Fe}_{0.97}\text{Ti}_{0.03}\text{O}_3$ (calcined at $960\text{ }^\circ\text{C}$), Figure 4.12 and Table 4.3.

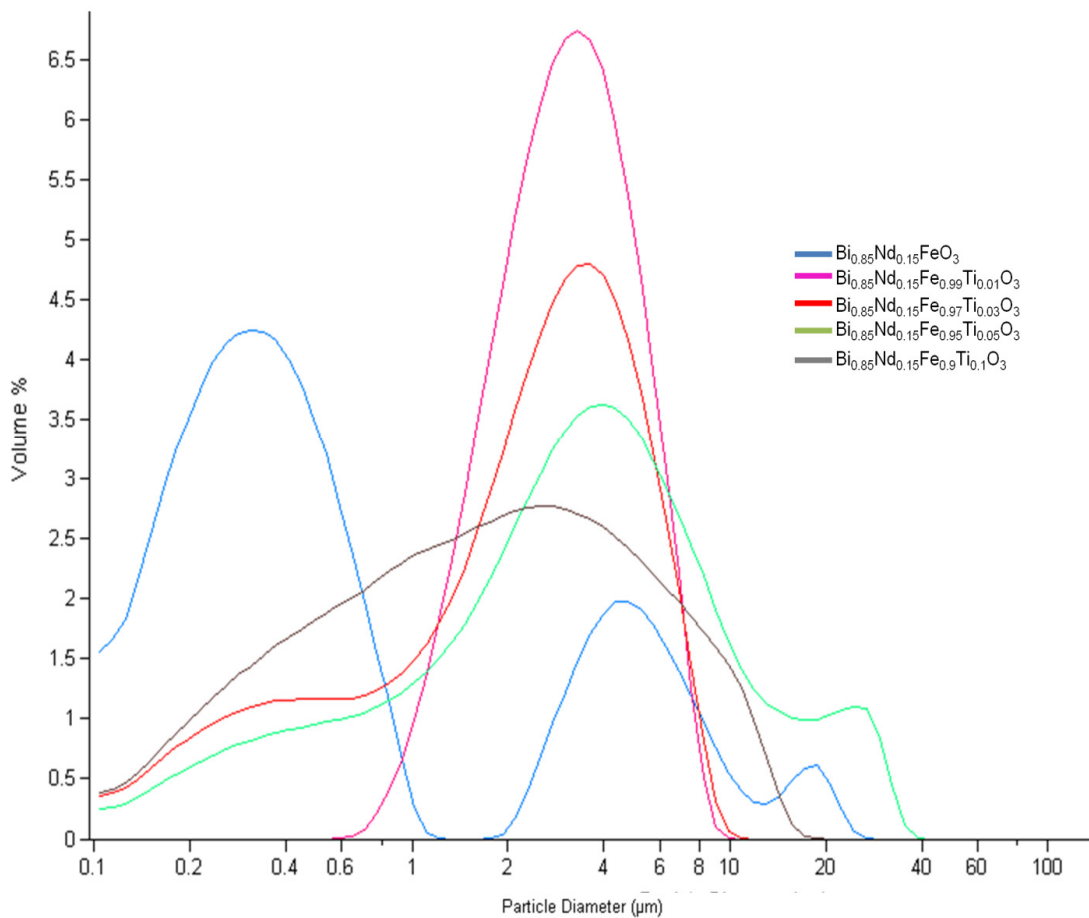


Figure 4.12: Particle size distribution curves of milled reacted powders prior to sintering.

Table 4.3: Particle diameters of reacted powders after milling. Errors in measurement are estimated at $\pm 0.01 \mu\text{m}$, less than the batch to batch variation.

	$\text{Bi}_{0.85}\text{Nd}_{0.15}\text{FeO}_3$	$\text{Bi}_{0.85}\text{Nd}_{0.15}\text{Fe}_{0.99}\text{Ti}_{0.01}\text{O}_3$	$\text{Bi}_{0.85}\text{Nd}_{0.15}\text{Fe}_{0.97}\text{Ti}_{0.03}\text{O}_3$	$\text{Bi}_{0.85}\text{Nd}_{0.15}\text{Fe}_{0.95}\text{Ti}_{0.05}\text{O}_3$	$\text{Bi}_{0.85}\text{Nd}_{0.15}\text{Fe}_{0.9}\text{Ti}_{0.1}\text{O}_3$
$d_{10} (\mu\text{m})$	0.15	1.49	0.33	0.45	0.29
$d_{25} (\mu\text{m})$	0.22	2.09	1.03	1.41	0.65
$d_{50} (\mu\text{m})$	0.36	3.05	2.45	3.33	1.72
$d_{75} (\mu\text{m})$	0.79	4.31	4.02	6.48	3.98
$d_{90} (\mu\text{m})$	5.76	5.63	5.59	13.41	7.24

Most compositions could be indexed as a single perovskite phase (Figure 4.14) however, some exhibited peaks which indicated that two perovskite phases were present. Such compositions were invariably close to the phase boundaries defined by the phase diagram reported by Karimi *et al.* [2], Figure 4.13. Sintering temperatures were chosen based on the optimum density of the samples and the phase assemblage of the calcined powders and sintered pellets remained essentially the same. The XRD traces of crushed ceramics are presented in the corresponding results chapter.

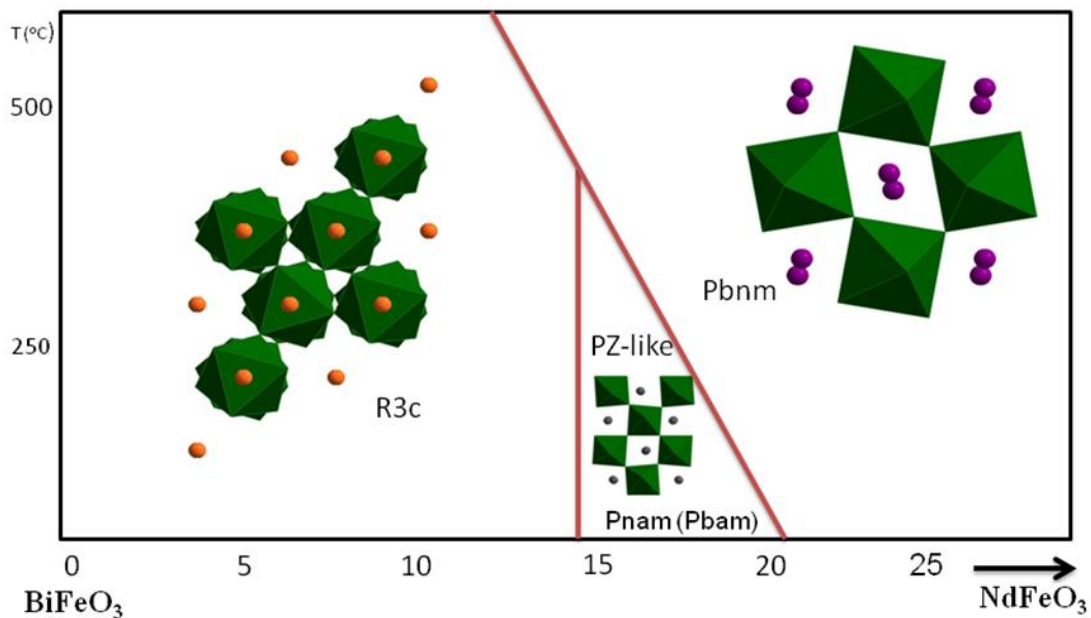


Figure 4.13: BiFeO_3 - NdFeO_3 phase diagram [2].

$\text{Bi}_{0.75}\text{Nd}_{0.25}\text{Fe}_{0.97}\text{Ti}_{0.03}\text{O}_3$	Perovskite- Pbnm	25%Nd, 3%Ti
$\text{Bi}_{0.85}\text{Nd}_{0.15}\text{Fe}_{0.97}\text{Ti}_{0.03}\text{O}_3$	Perovskite- Pbam	15%Nd, 3%Ti (pre-milled Nd_2O_3)
$\text{Bi}_{0.9}\text{Nd}_{0.1}\text{Fe}_{0.97}\text{Ti}_{0.03}\text{O}_3$	Perovskite- R3c	10%Nd, 3%Ti
$\text{Bi}_{0.85}\text{Nd}_{0.15}\text{FeO}_3$	Perovskite- R3c & Pbam	15%Nd, 0%Ti

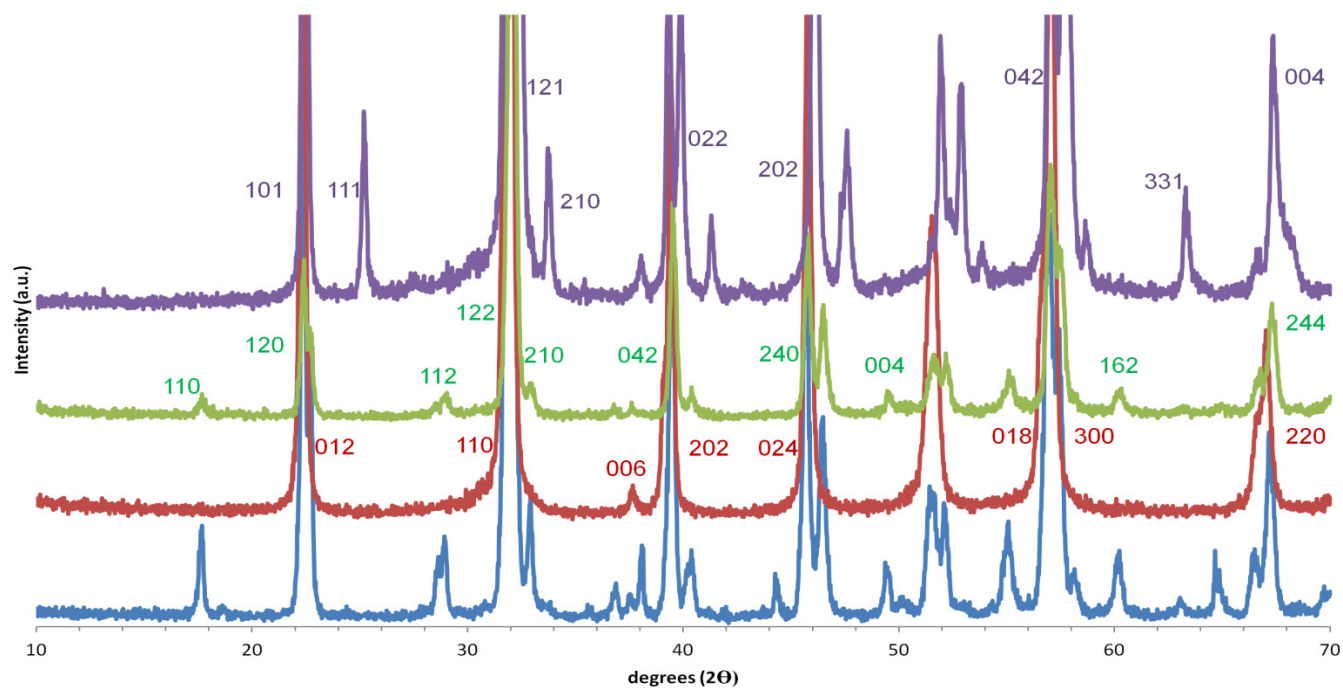


Figure 4.14: X-ray diffraction from calcined powders. The red, green and purple indices, respectively, correspond to R3c, PZ-like and orthoferrite phase. The table above indicates the structure of each sample along with the dopant concentration

References

1. R.M. Cornell, U. Schwertmann, *The iron oxides: structure, properties, reactions, occurrences and uses*, **2003**, Wiley VCH, ISBN 3-527-30274-3.
2. S. Karimi, I.M Reaney, I. Levin, I. Sterianou *Nd-doped BiFeO₃ ceramics with antipolar order*, **2009**, App. Phys. Lett., 94, 112903(52).

Chapter 5: Ti doped $\text{Bi}_{0.85}\text{Nd}_{0.15}\text{FeO}_3$ ceramics

5.1. Introduction

BiFeO_3 (BFO) is a PbO-free, perovskite-structured material which is currently gaining attention due to its purported multiferroic applications. The potential for magnetoelectric coupling between spin and polarisation has instigated research into the use of BFO in multiple state memory elements, electric field controlled ferromagnetic resonance devices and transducers with magnetically modulated piezoelectricity. However, it has not yet been commercially exploited because its high leakage current leads to poor quality polarisation-electric field (P-E) hysteresis loops, particularly at lower frequencies. Among all the extensive research performed to overcome this problem, A-site doping has been the most successful method to date and has resulted in more saturated hysteresis loops and lower leakage currents. This success is limited however and there are still considerable barriers to overcome if BFO is to be put into production.

Recently, Karimi *et al.* (2009) [1] demonstrated that the structure of BFO can be forced from polar (R3c) to antipolar (Pbam) at $x \cong 0.15$ in the solid solution $\text{Bi}_{1-x}\text{Nd}_x\text{FeO}_3$. The work described here focuses on co-doping BFO to improve the ferroelectric properties using, in addition to Nd^{3+} on the A-site, aliovalent Ti-doping on the B-site to reduce conductivity and leakage currents.

5.2. Structure and Microstructure

5.2.1. X-Ray Diffraction

XRD traces obtained from $\text{Bi}_{0.85}\text{Nd}_{0.15}\text{Fe}_{1-y}\text{Ti}_y\text{O}_3$ for all values of y are shown in Figure 5.1. For compositions with $y = 0$, peaks could be indexed according to a mixture of the orthorhombic, PZ-like, reported by Karimi *et al.* [1], and the rhombohedral BFO structure. As the Ti (y) concentration increased, the rhombohedral peaks disappeared and all intensities were attributed to the PZ-like phase. For $y > 0.05$, the peaks associated with the PZ-like structure were broad suggesting a decrease in the effective diffracting volume, possibly relating to a reduction in the correlation length of antipolar order.

Karimi *et al.* [1] reported that equivalent samples to $y = 0$ were single-phase and PbZrO_3 structured, Figure 4.13. At lower Nd concentrations, the same authors reported that the rhombohedral phase was stable at room temperature. The appearance of a mixture of rhombohedral and PbZrO_3 structured phases, contradicts this initial report, suggesting that the samples of Karimi *et al.* were either more homogeneous or that the PbZrO_3 phase field is shifted to higher Nd concentration.

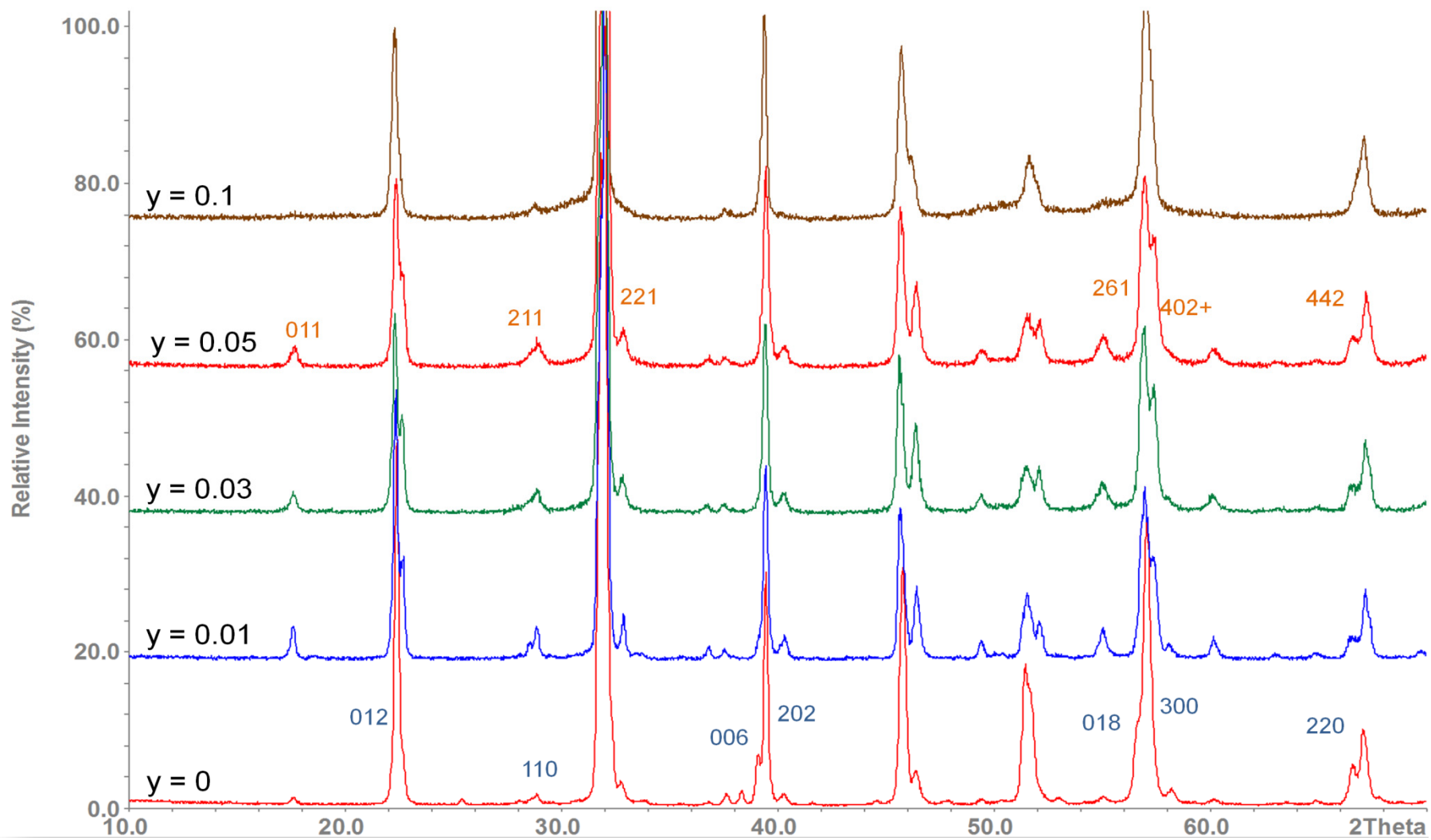


Figure 5.1: XRD patterns of $\text{Bi}_{0.85}\text{Nd}_{0.15}\text{Fe}_y\text{Ti}_{1-y}\text{O}_3$. (Blue indices correspond to R3c and red indices correspond to the PZ-like phase.)

5.2.2 Scanning Electron Microscopy (SEM)

Secondary electron images of the fractured surfaces of all samples are presented in Figure 5.2. The grain size increases from 2 μm to 5 μm for samples $y = 0$ and $y = 0.01$ but then decreases to less than 1 μm for samples with higher Ti concentrations.

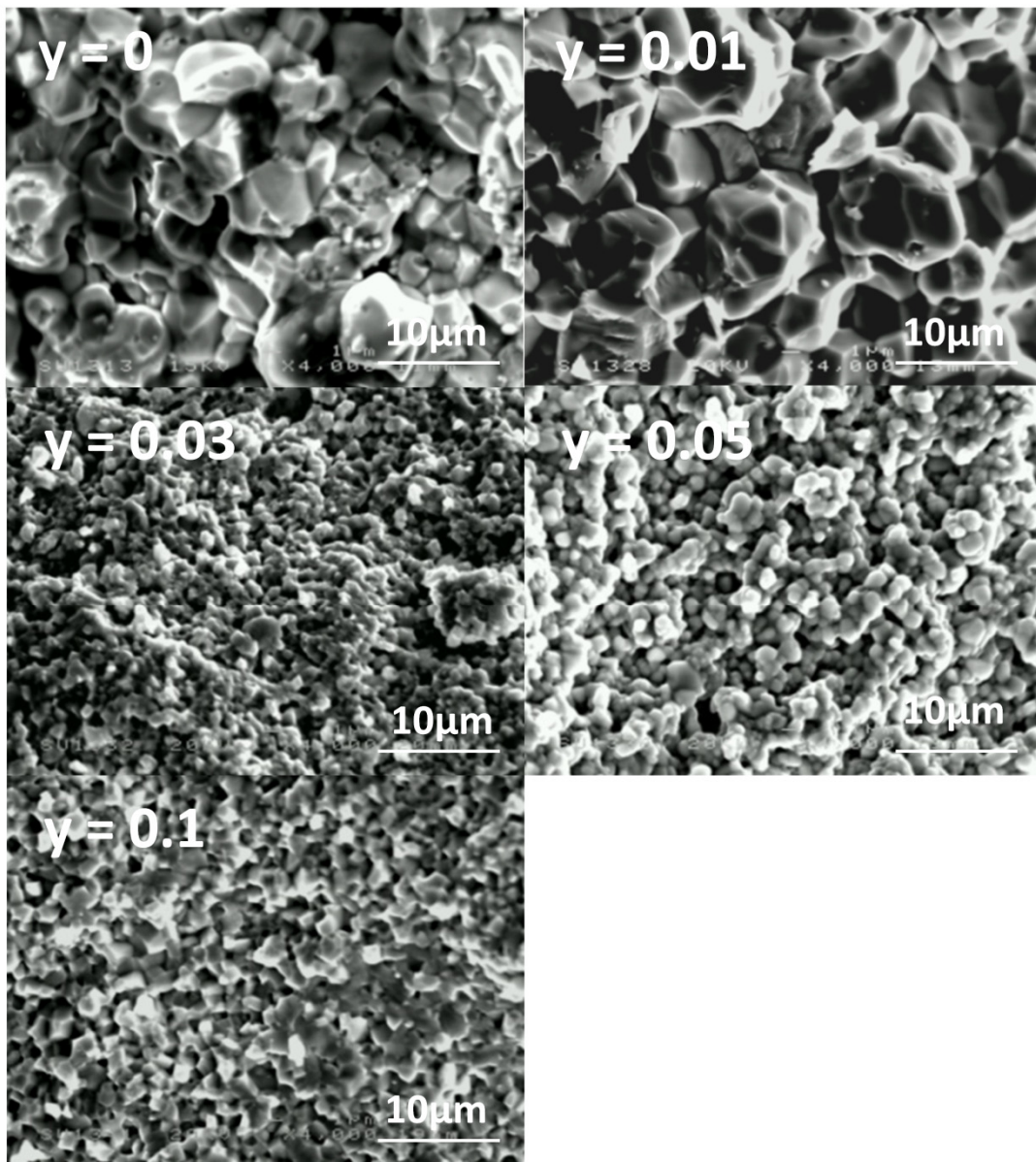


Figure 5.2: Secondary electron images of Ti-doped Bi_{0.85}Nd_{0.15}FeO₃ ceramics.

Energy dispersive x-ray spectroscopy (EDS) of Ti doped Bi_{0.85}Nd_{0.15}FeO₃ samples along with backscattered images are shown in Figure 5.3. Quantitative EDS confirmed that Ti was homogeneously dispersed throughout the samples and also that the Ti concentration increased with increase in y . Despite considerable potential error due to strong overlap of the NdL and TiK peaks, the ratios of the constituent ions were close to the batched values, particularly at higher values of y .

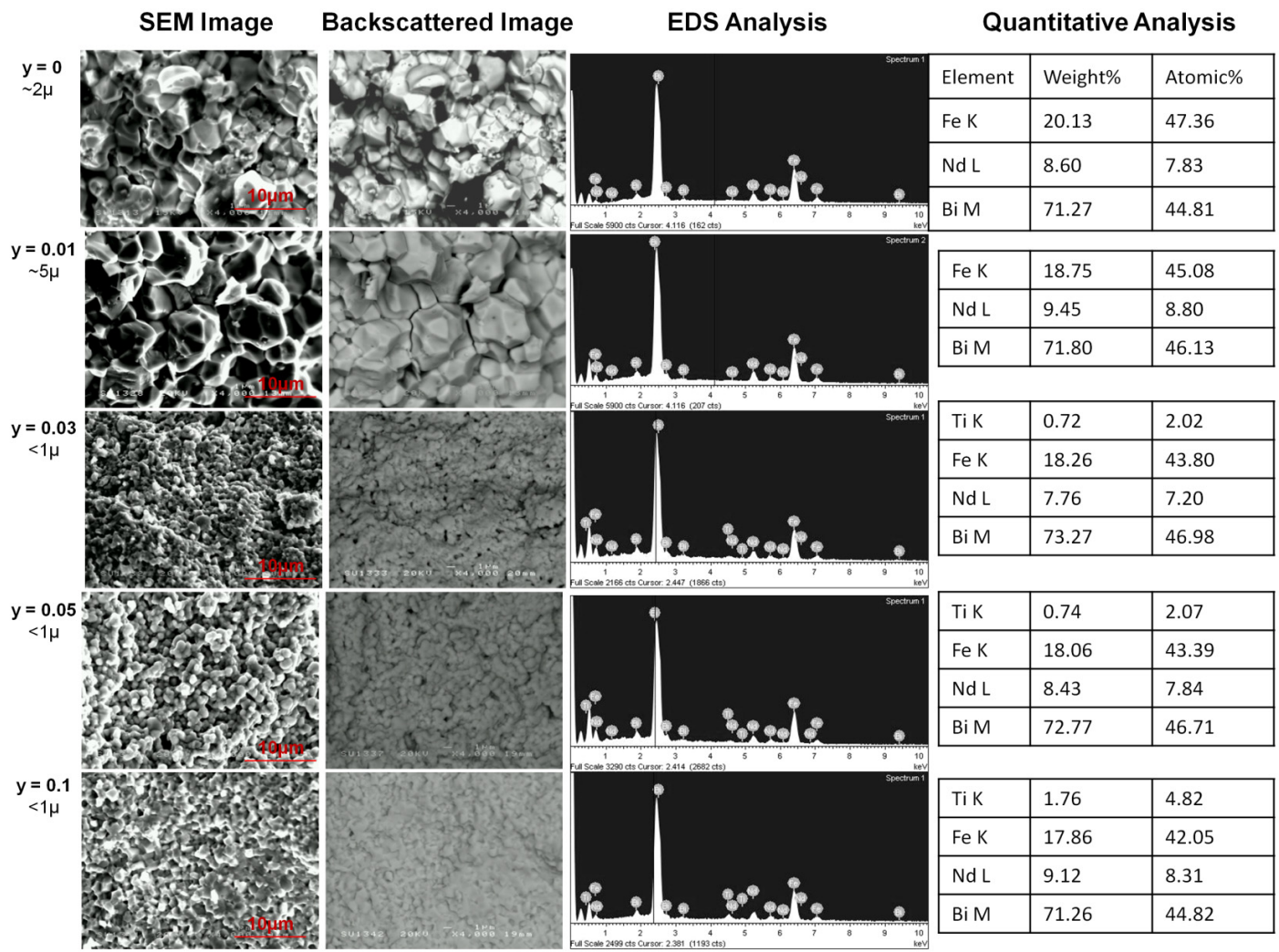


Figure 5.3: EDS results of Ti doped $\text{Bi}_{0.85}\text{Nd}_{0.15}\text{FeO}_3$ samples corresponding with backscattered images and elemental analysis tables.

5.2.3. Transmission Electron Microscopy (TEM)

The structural evolution as a function of Ti concentration is illustrated in Figure 5.4 using $\langle 110 \rangle_p$ zone axis electron diffraction patterns. For compositions with $y = 0$, 0.01 and 0.03 the superstructure reflections were identical (shown here for $y = 0.03$ in Figure 5.4a, and consistent with the PZ-like structure [2]. However, for $y = 0$ some regions were observed which did not exhibit quadrupled reflections and were thus considered to arise from the rhombohedral BiFeO_3 structure, in accordance with XRD (Figure 5.1). For $y = 0.01$ and 0.03, it was noted that all grains examined exhibited the PZ-like structure, consistent with XRD data. In Figure 5.4a, superstructure reflections at $\frac{1}{2}\{hkl\}_p$ positions (A) are present and associated with antiphase rotations of the $[\text{FeO}_6]$ octahedra. The B-arrowed spots appearing at $\frac{1}{2}\{001\}_p$ and $\frac{1}{2}\{110\}_p$ are typical of the PbZrO_3 structure, in which the oxygen octahedra rotation produces an orthorhombic $\sqrt{2}a \times \sqrt{2}a \times 2a$ unit cell. The spots indicated as C at $\frac{1}{4}\{111\}_p$ reveal the quadrupling of d-spacing of the $\{111\}$ planes in the perovskite structure and may only be explained if $c \approx 4a$ rather than $2a$ [1]. The electron diffraction (ED) pattern of $y = 0.05$ (Figure 5.4b) showed superstructure in the same reciprocal positions as the PZ-like phase but which were diffuse and streaked.

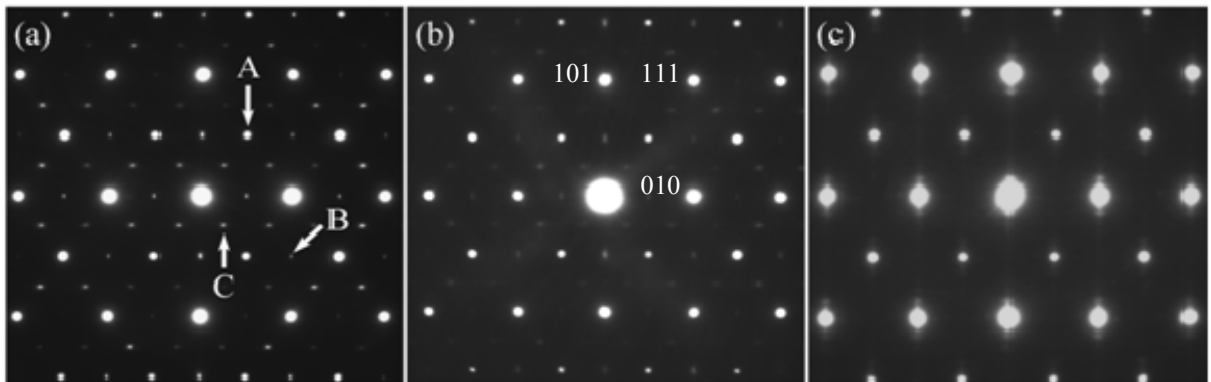


Figure 5.4: $\langle 110 \rangle_p$ SAED patterns of (a) $y = 0.03$; (b) $y = 0.05$ and (c) $y = 0.1$.

Superstructure reflections at $\frac{1}{2}\{hkl\}_p$ positions (A) are indicated and associated with antiphase rotations of the $[\text{FeO}_6]$ octahedra. The B-arrowed spots appearing at $\frac{1}{2}\{001\}_p$ and $\frac{1}{2}\{110\}_p$ are typical of PbZrO_3 structure, in which the oxygen octahedra rotation produces an orthorhombic $\sqrt{2}a \times \sqrt{2}a \times 2a$ unit cell. The C-arrowed spots at $\frac{1}{4}\{111\}_p$

reveal the quadrupling of d-spacing of the $\{111\}$ planes in the perovskite structure and may only be explained if $c \approx 4a$ rather than $2a$ [1].

For $y = 0.1$ (Figure 5.4c), the superstructure reflections associated with the PZ-like phase are absent and instead new incommensurate, satellite spots appear close to the fundamental perovskite reflections. Cheng *et al.* observed incommensurate superstructure at $\frac{1}{x}\{110\}$ positions in Sm-doped BiFeO_3 thin films appearing in nanoregions between FE and AFE phase regions, which they attributed to interfacial modulation arising from the competition between the two phases [3].

Figure 5.5a and b reveals the dark field image associated with the PZ-like superstructure in $y = 0$, and incommensurate spots in $y = 0.1$, respectively. In Figure 5.5a, the antiphase boundaries between antipolar regions that have nucleated out of the phase are observed whereas $y = 0.1$ shows some bright areas ~ 5 nm diameter. The exact nature of the incommensurate superstructure in $y = 0.1$ is not known but overall the ED patterns and dark field images illustrate that antipolar order is gradually destroyed for $y > 0.03$.

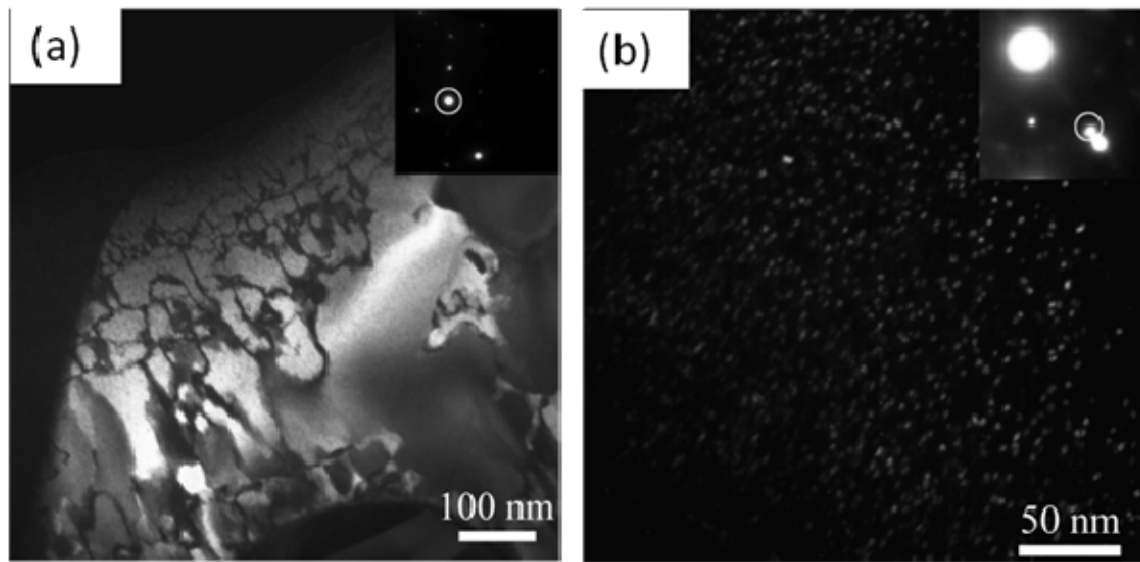


Figure 5.5: Dark field images from (a) $y = 0$ and (b) $y = 0.1$, using $\frac{1}{4}\{hkl\}$ and primary incommensurate satellite reflections, respectively.

5.3. Differential Scanning Calorimetry (DSC)

Figure 5.6a shows the differential scanning calorimetry (DSC) data for all samples. The large peaks correspond to the phase transition from the paraelectric to the antipolar state (T_C) and the weaker peaks relate to the Néel temperature (T_N) of the ceramics. T_C and T_N are plotted as a function of composition in Figure 5.6b. T_N decreases linearly with increasing Ti concentration. This trend is consistent with a dilution of long range antiferromagnetic coupling by substitution of the magnetic Fe^{3+} by diamagnetic Ti^{4+} ions [4]. Note that it is believed that T_N for sample $y = 0$ could not be observed due to overlap with T_C . In contrast to the linear trend for T_N , T_C shows a non linear trend as a function of composition.

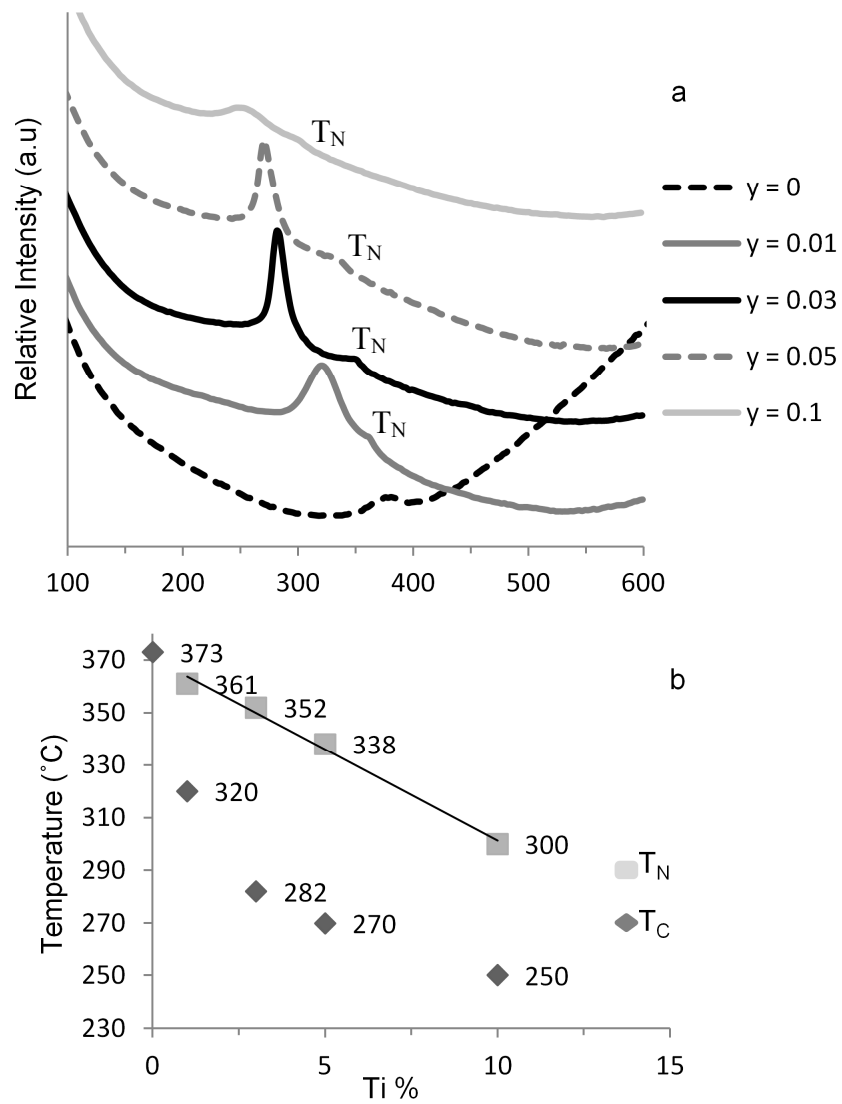
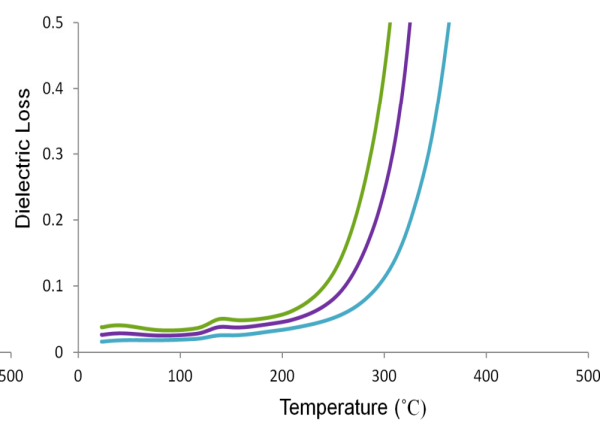
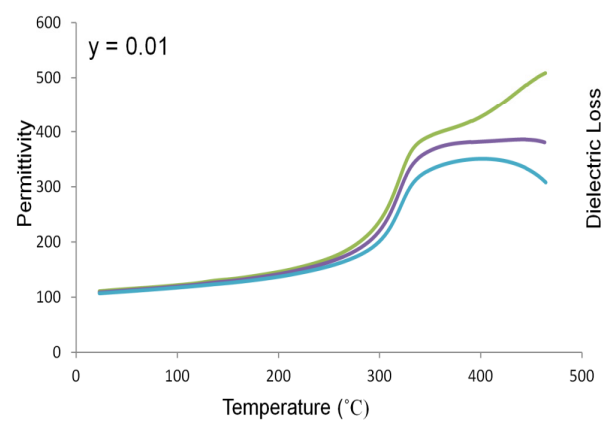
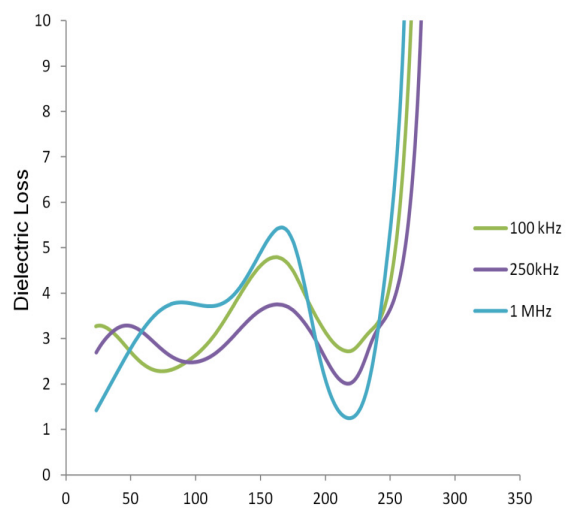
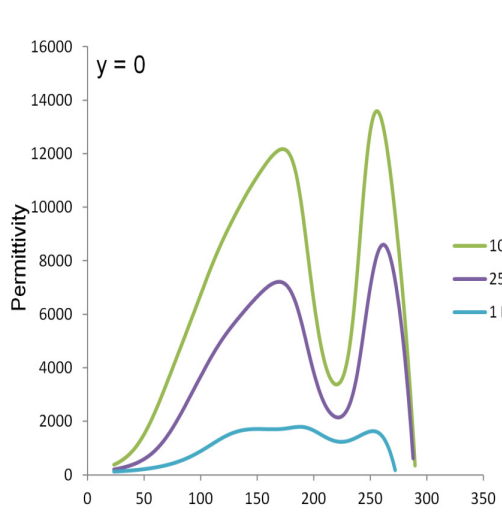


Figure 5.6: (a) DSC curves of all samples and (b) a plot of T_C and T_N versus y .

5.4. Electrical Properties

Figure 5.7 shows dielectric measurement results of Ti doped $\text{Bi}_{0.85}\text{Nd}_{0.15}\text{FeO}_3$ ceramics. The dielectric loss for $\text{Bi}_{0.85}\text{Nd}_{0.15}\text{FeO}_3$ is orders of magnitude greater than for the Ti-doped samples (notice the y axis scales). Consequently, the peaks in permittivity vs. temperature of $y = 0$ correspond to space charges in the ceramics and do not correspond to phase transitions. In contrast the dielectric loss of Ti-doped samples is less than 0.1 at temperatures lower than 300 °C. The temperatures of step-like changes in permittivity vs. temperature curves of these samples correspond well with phase transition temperatures in DSC results. The frequency dependent relaxation behaviour between 200 °C to 400 °C will be discussed in detail in the next chapter.

Figure 5.8 shows a comparison between the dielectric permittivity and loss as a function of temperature at 100 kHz. For $\text{Bi}_{0.85}\text{Nd}_{0.15}\text{FeO}_3$, there is no T_C observed despite a clear anomaly at 373 °C in the DSC data. Moreover, the dielectric loss for $\text{Bi}_{0.85}\text{Nd}_{0.15}\text{FeO}_3$ is orders of magnitude greater than for the Ti-doped samples. It is proposed that the large permittivity and $\tan \delta$ of the undoped sample arise from oxygen loss that results in the formation of $V^{\bullet\bullet}_O$ and reduction of Fe^{3+} ions to Fe^{2+} ions, according to the formula $\text{Bi}(\text{Fe}^{3+}_{1-x}\text{Fe}^{2+}_x)\text{O}_{3-x/2}$. The existence of Fe^{2+} in BiFeO_3 has been observed by XPS [5]. For the Ti doped samples, there are peaks in the dielectric permittivity and loss at approximately the same temperature as those in the DSC data. Moreover, the dielectric loss is reduced significantly between room temperature and ~ 300 °C, above which it rises sharply, presumably as the conductivity increases.



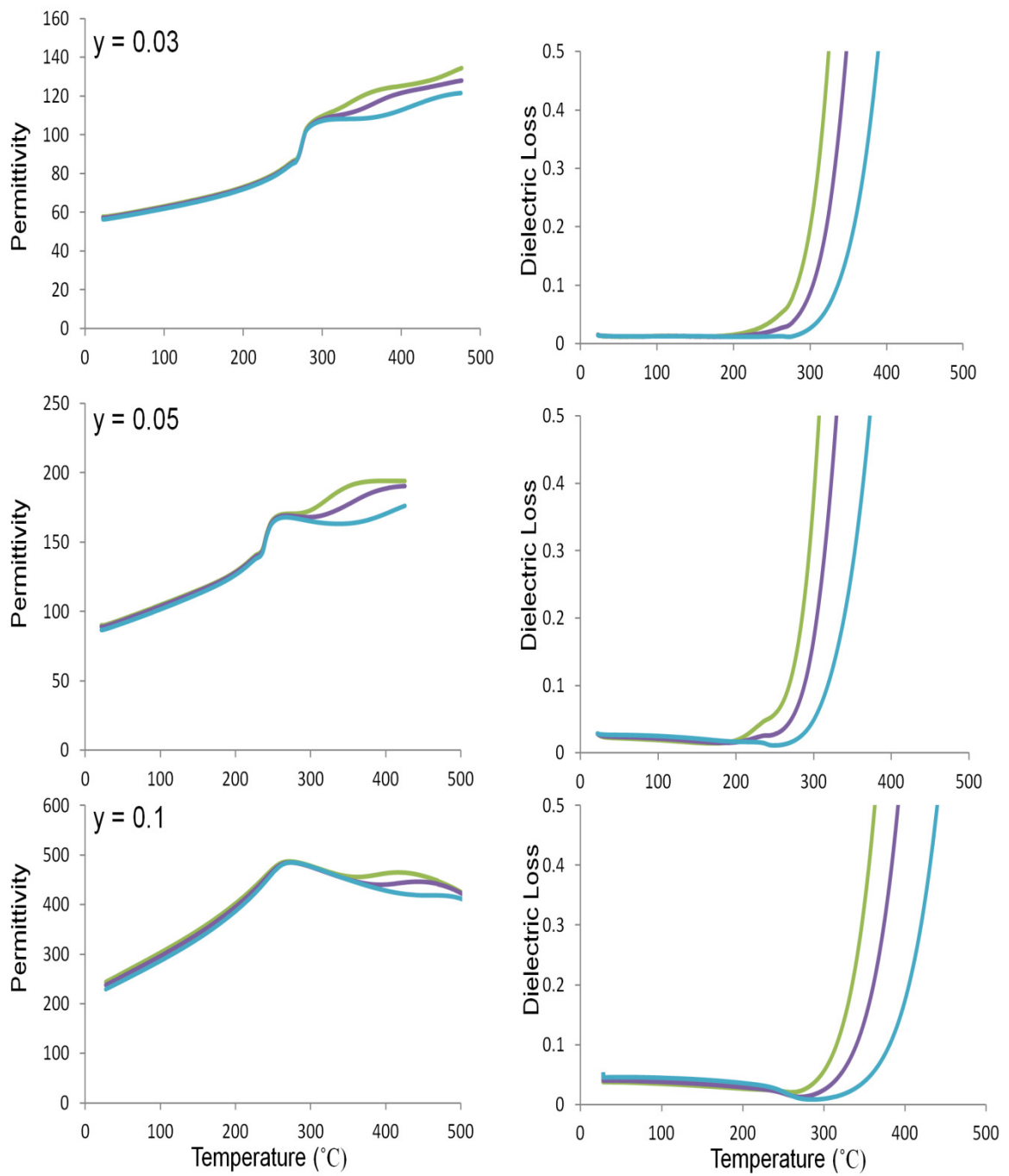


Figure 5.7: Permittivity and dielectric loss vs. temperature plots of Ti doped $\text{Bi}_{0.85}\text{Nd}_{0.15}\text{FeO}_3$.

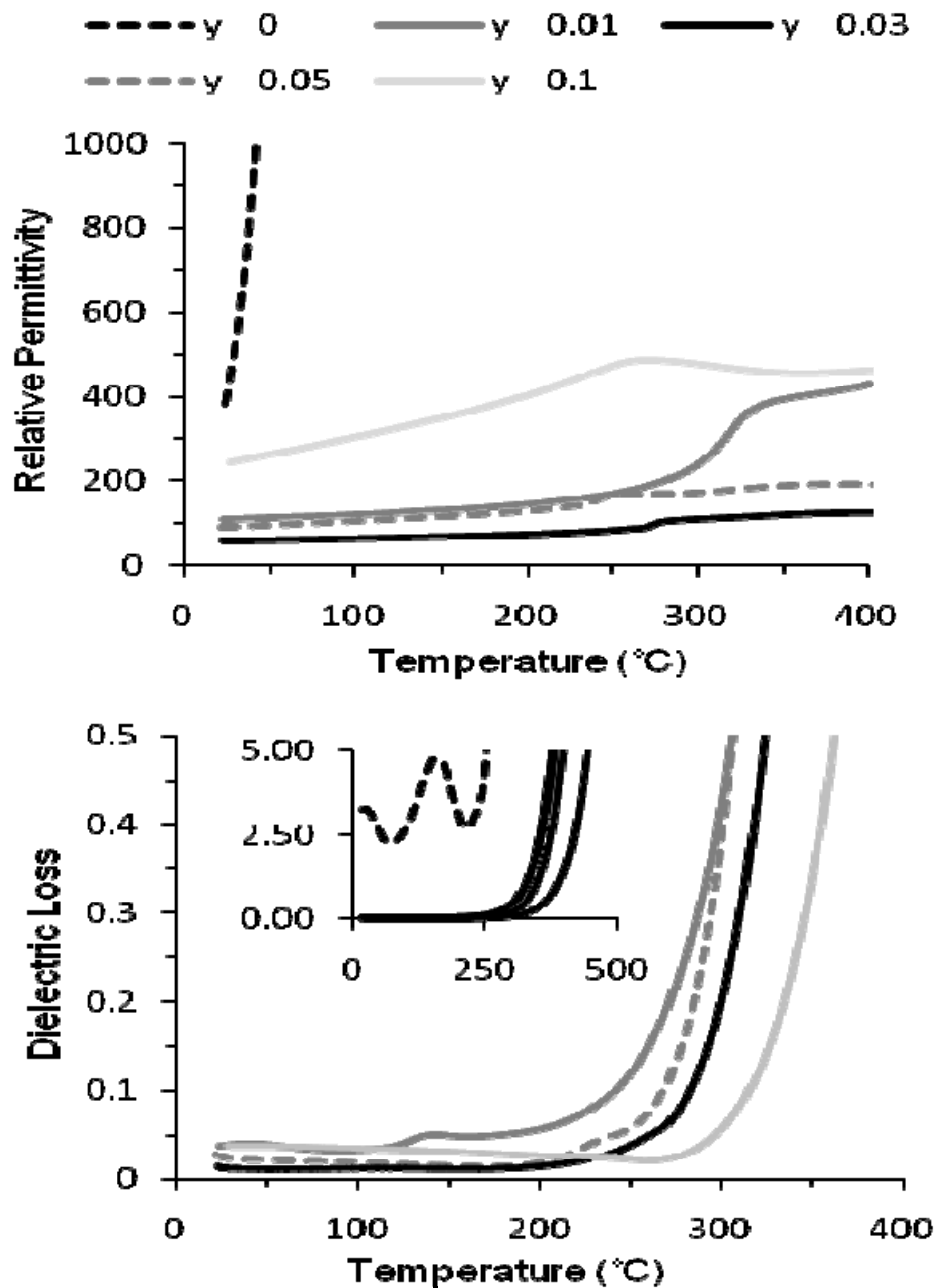


Figure 5.8: Comparison of dielectric properties for $\text{Bi}_{0.85}\text{Nd}_{0.15}\text{Fe}_{1-y}\text{Ti}_y\text{O}_3$ ceramics at 100 kHz.

To further investigate the effect of Ti-doping on the conductivity of $\text{Bi}_{0.85}\text{Nd}_{0.15}\text{FeO}_3$, impedance spectroscopy (IS) was performed. According to the impedance data (Table 5.1), the bulk resistance increases sharply for 1% Ti-doping but remains relatively constant at higher concentrations. Figure 5.9 compares IS data for $y =$

0 and 0.03. In the Z^* complex plane plot, $y = 0$ exhibits two contributions, one at 250 K and another at 373 K, whereas only one contribution is observed for $y = 0.03$. Combined Z'' and M'' spectroscopic plots are helpful in determining the source of the contributions observed in Z^* plots. For example, a peak maximum in a M'' spectroscopic plot, M''_{\max} , is inversely proportional to capacitance, so the highest M'' peak can be used to identify the component with the smallest capacitance in the sample, *i.e.* the bulk or grain response. In addition, the peak maximum in a Z'' spectroscopic plot, Z''_{\max} , is proportional to resistance; therefore, the highest Z'' peak identifies the component with the highest resistance, in this case the grain boundary. For $y = 0$, it is clearly seen in Figure 5.9 that a bulk response is observed at 250 K, small Z''_{\max} and large M''_{\max} , whereas a grain boundary response is observed at 373 K, small M''_{\max} and large Z''_{\max} . The coincidence in frequency of M''_{\max} and Z''_{\max} for the Ti-doped samples, as shown for $y = 0.03$ at 573 K in Figure 5.9, concludes that the material is electrically homogeneous, in other words only a bulk response is observed.

Table 5.1: Electrical properties of $\text{Bi}_{0.85}\text{Nd}_{0.15}\text{Fe}_y\text{Ti}_{1-y}\text{O}_3$ ceramics.

	Temperature (K)	Capacitance ($\pm 10\%$) (pF cm^{-1})	Resistance ($\pm 10\%$) (Ω cm)	Activation Energy (eV)
$y = 0$ Bulk	275	12	1.62E+5	0.29(2)
$y = 0$ GB	373	1800	7.61E+3	0.52(4)
$y = 0.01$	573	25	2.8E+6	1.25(3)
$y = 0.03$	573	25	2.8E+5	1.07(2)
$y = 0.05$	573	24	5.55E+5	1.07(2)
$y = 0.1$	573	44	5.83E+5	1.10(1)

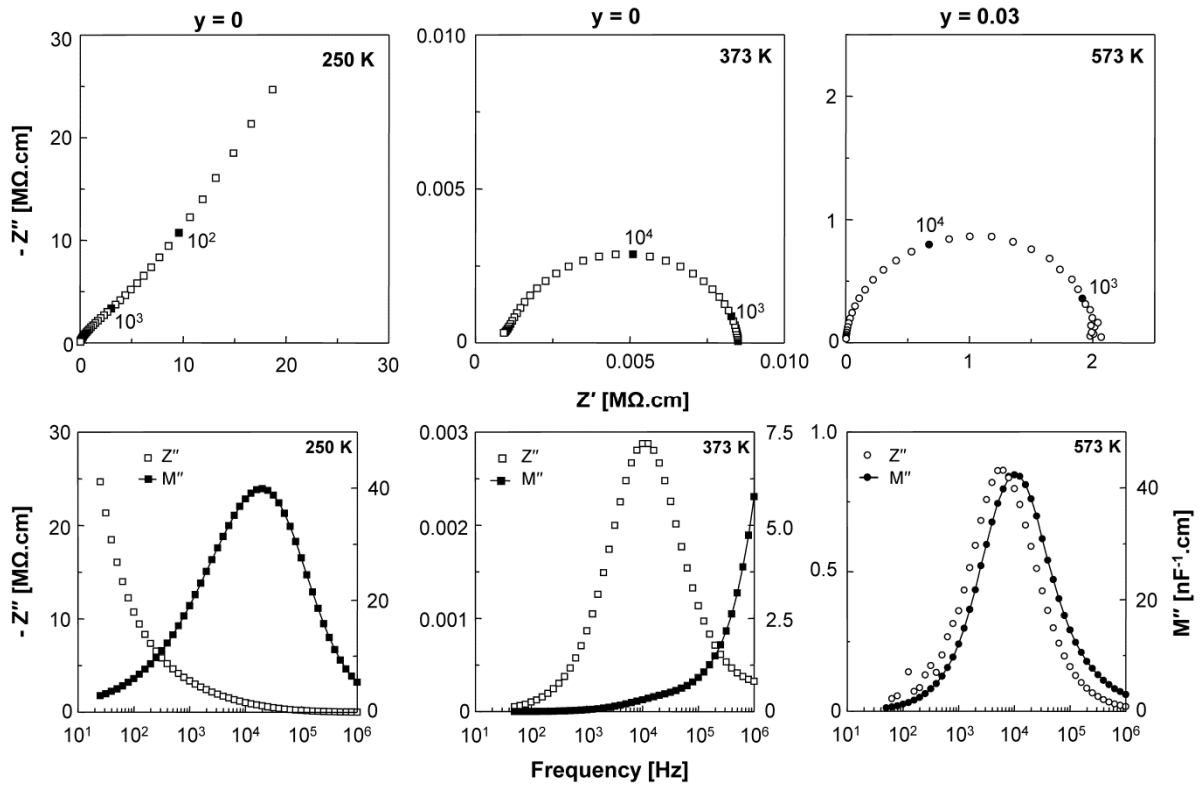


Figure 5.9: Z^* complex plane and combined Z'' and M'' spectroscopic plots for $y = 0$ at 275 K and at 373 K, showing the bulk and grain boundary responses, respectively, and for $y = 0.03$ at 573 K, showing only a bulk response. The plots for $y = 0.03$ are representative of $y \geq 0.01$.

An Arrhenius plot of the bulk and grain boundary conductivity for $y = 0$ and the bulk conductivity for $y \geq 0.03$ is shown in Figure 5.10. The activation energy of the Ti-doped samples is far higher than both the bulk and grain boundary components of undoped $\text{Bi}_{0.85}\text{Nd}_{0.15}\text{FeO}_3$.

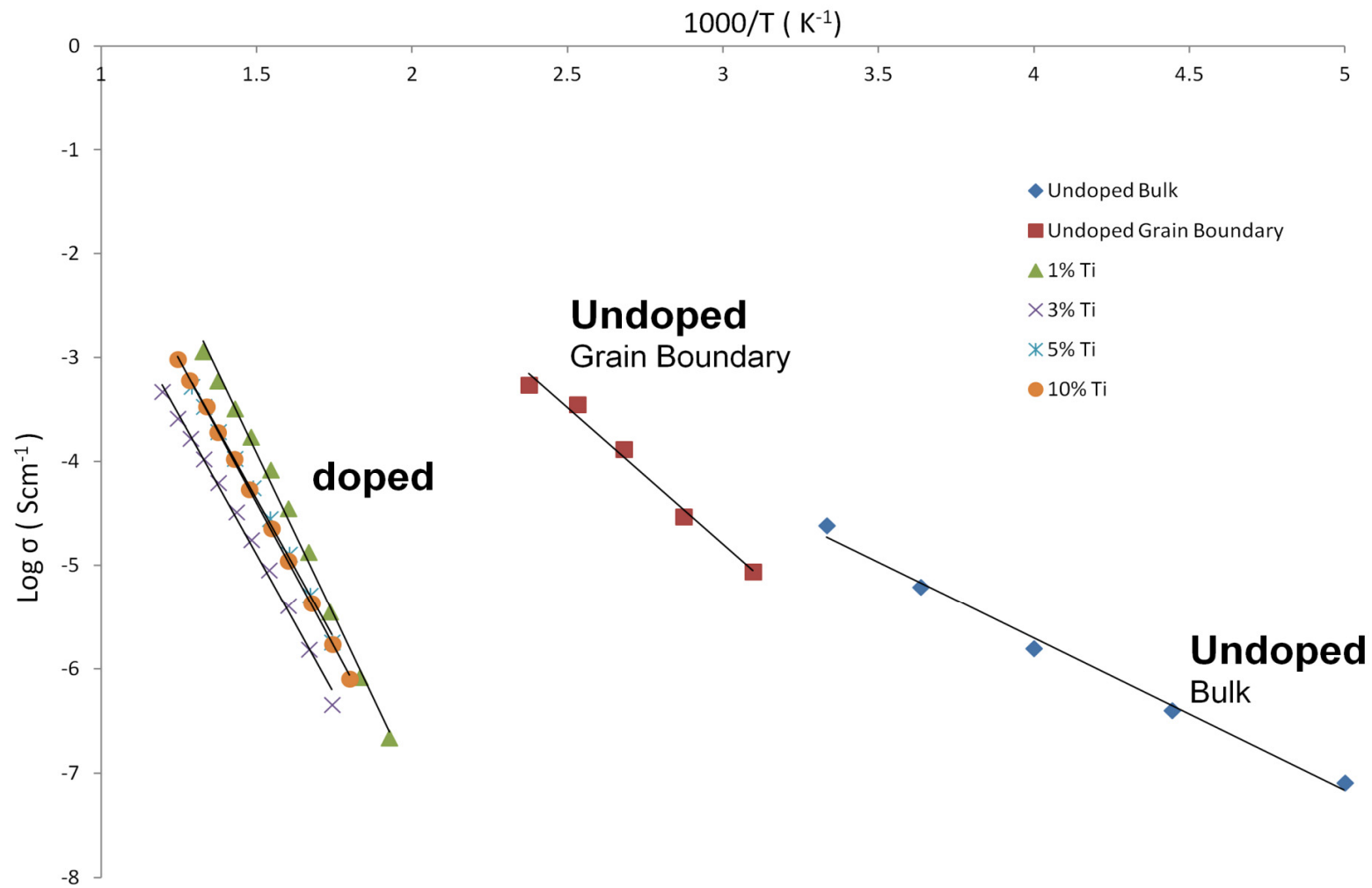


Figure 5.10: Arrhenius plot of bulk and grain boundary conductivities for $y = 0$ and bulk conductivities for $y \geq 0.01$.

The dielectric and IS data conclusively demonstrate that Ti-doping reduces the conductivity in the $\text{Bi}_{0.85}\text{Nd}_{0.15}\text{Fe}_y\text{Ti}_{1-y}\text{O}_3$ system. The bulk activation energy for all Ti doped compositions is > 1 eV and comparable with more conventional electroceramics such as doped PbTiO_3 and BaTiO_3 [6, 7, 8]. The low bulk activation energy (E_a) associated with the undoped sample is attributed to oxygen loss with concomitant partial reduction of Fe^{3+} to Fe^{2+} , *i.e.*, $\text{Bi}(\text{Fe}^{3+}_{1-x}\text{Fe}^{2+}_x)\text{O}_{3-x/2}$. Ti-doping, with the change in E_a clearly demonstrates a change in the bulk conduction mechanism.

An E_a of ~ 0.29 eV is consistent with small polaron hopping between Fe^{2+} and Fe^{3+} ions. The substitution of Fe by Ti (in a ratio of 1:1) was carried out without assuming any specific (ionic/electronic) charge compensation mechanism. Secondary phases were not detected up to $y = 0.1$, however the non-linear relationship between T_C and Ti concentration may suggest that there is more than one mechanism of charge compensation for Ti-doping. These mechanisms are the subject of further study. However, it is probable that for low ($y < 0.03$) concentrations Ti^{4+} compensates for Fe^{2+} and eliminates the oxygen vacancies present in $y = 0$ and this is the origin of the large decrease in bulk conductivity on Ti-doping. For higher Ti-doping levels antipolar order is disrupted. The most probable mechanism for disruption of antipolar order generating an incommensurate state is the presence of metal vacancies, most likely on the A-site, *i.e.*, V_{Bi} or V_{Nd} . Similar effects have been observed in PbZrO_3 -based compounds when donor doped with La and Nb [9, 10]. Unpublished data from Maclaren and co-workers [11] have confirmed that Nd is exsolved from the solid solution for $y = 0.1$ in the form of Nd_2O_3 nano-rods, suggesting that the formation of V_{Nd}''' is the preferred compensation mechanism for $\text{Ti}_{\text{Fe}}^\bullet$ according to the equation:



Figure 5.11 shows a comparison of the polarisation *vs.* electric field loops attained from samples with $y = 0$ and $y = 0.03$. For $y = 0$, the high leakage current leads to a malformed loop with no clear relationship between polarisation and field. In contrast, $y = 0.03$ shows a linear dependence of polarisation with field, similar to that

obtained for PZ ceramics under equivalent experimental conditions. Large electric fields can now be applied to these compounds but the absence of switching to a FE from an AFE state in the polarisation vs. field loops suggests the switching field is high. Comparison with undoped PZ indicates that the coercive field for AFE/FE switching is $\sim 100\text{-}200$ kV/cm and often ceramics breakdown before the coercive field is attained [12].

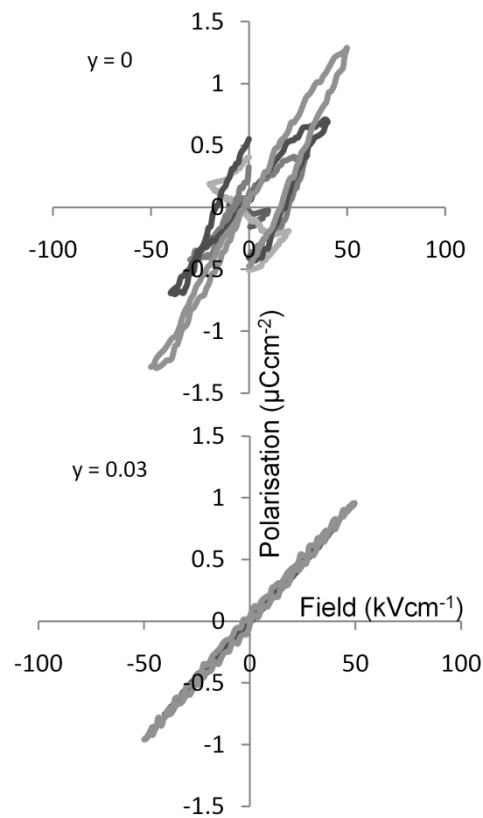


Figure 5.11: Polarisation vs. electric field for $y = 0$ and $y = 0.03$. Note that all Ti doped samples have identical response.

5.5. Conclusions

$\text{Bi}_{0.85}\text{Nd}_{0.15}\text{Fe}_y\text{Ti}_{1-y}\text{O}_3$ compositions have been fabricated. X-ray and electron diffraction established that Ti-doping promotes the PZ-like structure, reported by Karimi *et al.* The PZ-like structure is retained for samples with $y \leq 0.05$. However, the diffuse streaked intensities and superstructure reflections in the electron diffraction data for $y = 0.05$ indicate that the correlation length of antipolar order is reduced and the system becomes incommensurate by $y = 0.1$. Ti-doping reduced the dielectric loss which allowed the AFE/PE phase transition to be observed in dielectric as well as DSC measurements. The PE/AFE transition showed a step down on cooling rather than a peak in permittivity. The decrease in loss was associated with a large decrease in the room temperature bulk conductivity from $\sim 1 \text{ mS cm}^{-1}$ to $< 1 \text{ }\mu\text{S cm}^{-1}$ and a large increase in activation energy for conduction from 0.29 eV to $> 1.0 \text{ eV}$. Large fields may now be applied to these ceramics.

References

1. S. Karimi, I.M Reaney, I. Levin, I. Sterianou, *Nd-doped BiFeO₃ ceramics with antipolar order*, **2009**, App. Phys. Lett., 94, 112903.
2. S. Karimi, I.M. Reaney, Y. Han, J. Pokorny, I. Sterianou, *Crystal chemistry and domain structure of rare-earth doped BiFeO₃ ceramics*, **2009**, J. Mater Sci, 10853-009-3545-1.
3. C. J. Cheng, D. Kan, S. H. Lim, W. R. McKenzie, P. R. Munroe, L. G. Salamanca-Riba, R. L. Withers, I. Takeuchi, and V. Nagarajan, *Structural transitions and complex domain structures across a ferroelectric to antiferroelectric phase boundary in epitaxial Sm- doped BiFeO₃ thin films*, **2009**, Phys. Rev. B, , 80, 014109.
4. W. M. Zhu, H. Y. Guo, and Z. G. Ye, *structural and magnetic characterization of multiferroic (BiFeO₃)_{1-x}(PbTiO₃)_x solid solutions*, **2008**, Phys. Rev. B, , 78, 014401.
5. D. Rout, K. Moon and S. L. Kang, *Temperature-dependent Raman scattering studies of polycrystalline BiFeO₃ bulk ceramics*, **2009**, J. Raman. Spectrosc. 40, 618-626.
6. O.P. Thakur, A. Feteira, B. Kundys, D.C. Sinclair, *Influence of attrition milling on the electrical properties of undoped-BaTiO₃*, **2007**, J. Euro. Ceram. Soc. 27, 2577-2589.
7. D. Voltzke, H.P. Abicht, *The influence of different additives and the mode of their addition on the sintering behaviour and the properties of semiconducting barium titanate ceramics*, **2000**, Solid State Sciences. 2, 149-159.
8. S. Zhao, S.J. Zhang, W. Liu, N.J. Donnelly, Z. Xu and C.A. Randall, *Time dependent dc resistance degradation in lead-based perovskites: 0.7 Pb (Mg_{1/3}Nb_{2/3})O₃0.3PbTiO₃*, **2009**, J. App. Phys., 105, 053705.

9. H. He and X. Tan, *Electric-field-induced transformation of incommensurate modulations in antiferroelectric $Pb_{0.99}Nb_{0.02}[(Zr_{1-x}Sn_x)(1-y)Ti_y] (0.98) O_3$* , **2005**, Phys. Rev., 72, 024102.
10. T. Asada and Y. Koyama, *La-induced conversion between the ferroelectric and antiferroelectric incommensurate phases in $Pb_{1-x}La_x(Zr_{1-y}Ti_y)O_3$* , **2004**, Phys. Rev., 69, 104108.
11. I. Maclaren, K. Kalantari and I.M.Reaney, in preparation.
12. U. Sukkha, R. Muanghlua, S. Niemcharoen, B. Boonchoma and N. Vittayakorn, *Antiferroelectric-ferroelectric phase transition in lead zinc niobate modified lead zirconate ceramics: crystal studies, microstructure, thermal and electrical properties*, **2010**, Appl. Phys. A, 100, 551-559.

Chapter 6: Structural phase transitions in 3% Ti-doped $\text{Bi}_{1-x}\text{Nd}_x\text{FeO}_3$ ceramics

6.1. Introduction

In the previous chapter, it was demonstrated that donor doping with Ti on the B-site significantly reduces the conductivity in $\text{Bi}_{0.85}\text{Nd}_{0.15}\text{FeO}_3$ ceramics [1]. In this chapter, the phase transitions as a function of Nd concentration are investigated in 3% Ti-doped $\text{Bi}_{1-x}\text{Nd}_x\text{FeO}_3$ ceramics.

Processing pure BFO is difficult due to Bi_2O_3 loss that tends to encourage the formation of impurity phases with lower standard enthalpy of formation such as $\text{Bi}_2\text{Fe}_4\text{O}_9$ ($-2776 \text{ kJ mol}^{-1}$) and $\text{Bi}_{25}\text{FeO}_{39}$ ($-7699.8 \text{ kJ mol}^{-1}$) compared to BFO (768 kJ mol^{-1}) [2]. Furthermore, two main problems must be resolved before BFO-based ceramics may be utilised in devices. BFO is essentially antiferromagnetic rather than ferromagnetic which leads to cancelling of macroscopic magnetization and generally prohibits linear magnetoelectric effects [3]. Furthermore, to be exploited as a ferroelectric and compete with BaTiO_3 (BT) and $\text{Pb}(\text{Zr},\text{Ti})\text{O}_3$ (PZT) for applications, BFO requires switching under high electric fields. Therefore, the conductivity and coercive fields need to be comparable with those in BT and PZT. A-site isovalent, rare earth (RE) dopants have been extensively investigated recently since, in BFO, they simultaneously reduce the volume fraction of impurity phases [3, 4], decrease T_C [4,5] (thereby reducing the coercive field) and promote a weak ferrimagnetic response [6, 7 and 8].

Although the scientific literature on BFO is quite extensive, there are few publications that report dielectric data as a function of temperature, presumably due to frequency dispersive space charge polarisation that obscures the changes in permittivity in the vicinity of structural phase transitions. Even though the source of conductivity in

BFO-based ceramics is controversial, it is intuitively reasonable to suggest that reduction of Fe^{3+} to Fe^{2+} occurs within the perovskite matrix, compensated by oxygen vacancies (V_O) [9]. As a result, donor-doping strategies [10, 11 and 12] reduce the concentration of V_O by compensating for Fe^{2+} , thus decreasing the number of charge carriers. The precise mechanisms are still unclear and are recommended as the subject of further studies. The most successful donor dopant to date has been Ti substituting for Fe, which was shown in chapter 5 and ref [9], to overcome issues arising from conductivity in $\text{Bi}_{0.85}\text{Nd}_{0.15}\text{FeO}_3$ ceramics at least at room temperature. The following chapter utilizes the same dopant strategy but explores the phase assemblage and transitions across the $\text{Bi}_{1-x}\text{Nd}_x\text{FeO}_3$ phase diagram and draws comparisons with better understood ferroelectric systems such as BT and PZT.

6.2. X-ray diffraction

XRD patterns for crushed pellets of 3%Ti doped $\text{Bi}_{1-x}\text{Nd}_x\text{FeO}_3$ ($0 \leq x \leq 0.25$) are shown in Figure 6.1. The peak at $2\theta \sim 57^\circ$ may be used to differentiate between the different perovskite phases present within the solid solution. When the shoulder of this peak is on the left side, the phase is rhombohedral and similar to the end-member, BiFeO_3 . A shoulder on the right side indicates presence of the orthorhombic, PZ-like phase [3]. Splitting of the same peak also occurs when the phase has the orthoferrite structure [3], associated with the NdFeO_3 end-member. The weak peaks at $2\theta \sim 16^\circ$ and 28° are also associated with the PZ-like phase but the peak at $2\theta \sim 25^\circ$ is uniquely associated with the orthoferrite, NdFeO_3 phase.

To understand the effect of donor doping throughout the $\text{Bi}_{1-x}\text{Nd}_x\text{FeO}_3$ solid solution, 3% Ti was substituted onto the B-site for all values of x . However, as reported by many authors, e.g., [11] and [12], traces of secondary phases are routinely observed in BFO ceramics in the absence of A-site dopants, Figure 6.1. The secondary phases observed are $\text{Bi}_{25}\text{FeO}_{40}$ and $\text{Bi}_2\text{Fe}_4\text{O}_9$ whose main XRD peaks occur at 27.6° and 28.2° 2θ , respectively.

Traces from samples with $x \leq 0.125$ may be indexed according to the FE, rhombohedral, R3c phase whereas compositions with $0.15 \leq x \leq 0.2$ are best described by the antipolar PbZrO₃-like Pbam structure, first reported by Karimi *et al.* [3]. Ceramics with $x = 0.25$, match well to the peak distribution and intensities for the paraelectric (PE) orthoferrite structure (Pnma symmetry) [3]. It should be noted however, that $x = 0.125$ contains some weak reflections characteristic of the PbZrO₃ phase (Pbam) that suggest the coexistence of R3c and Pbam, thus defining this composition as lying at the antiferroelectric/ferroelectric (AFE/FE) phase boundary.

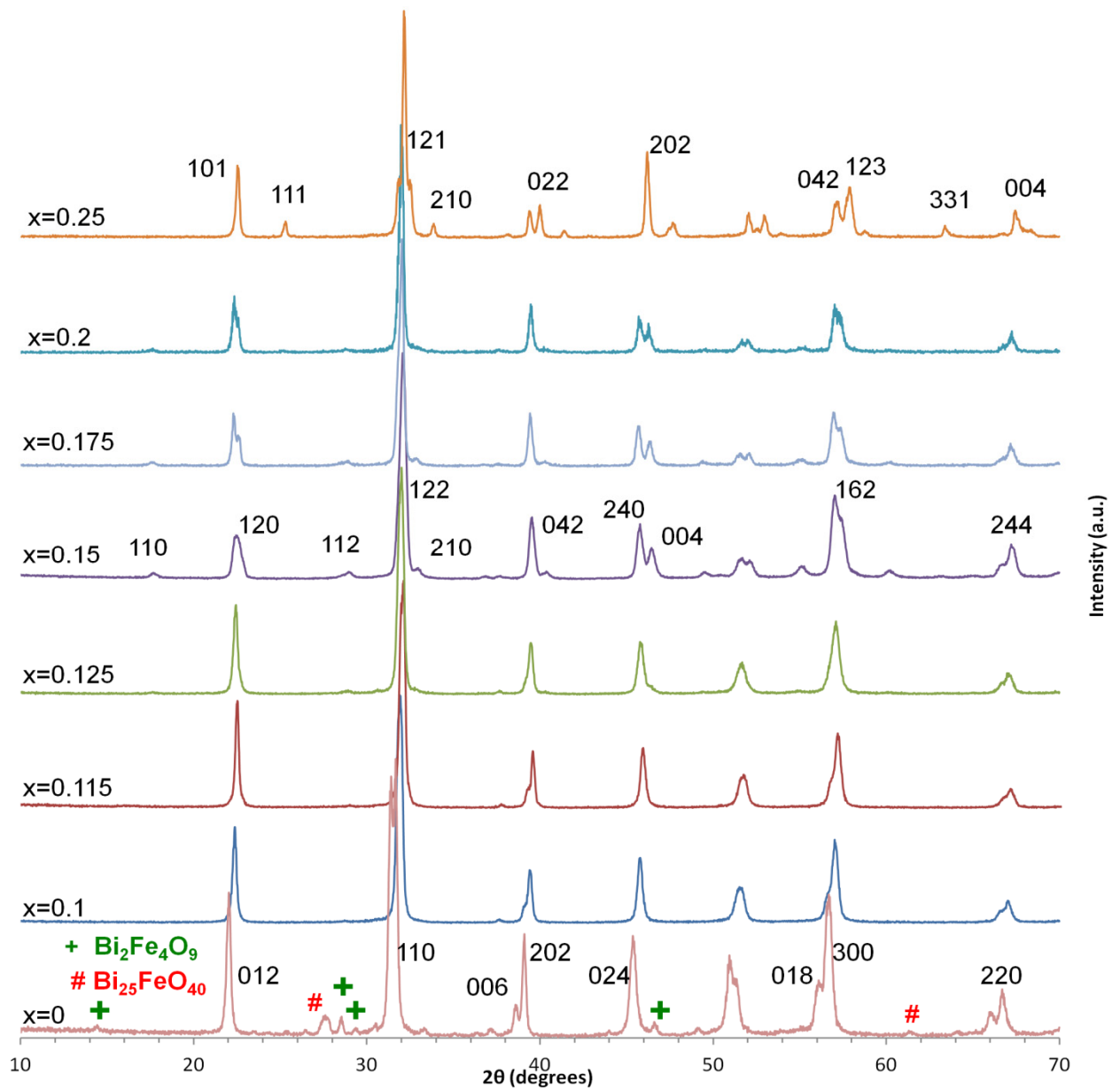
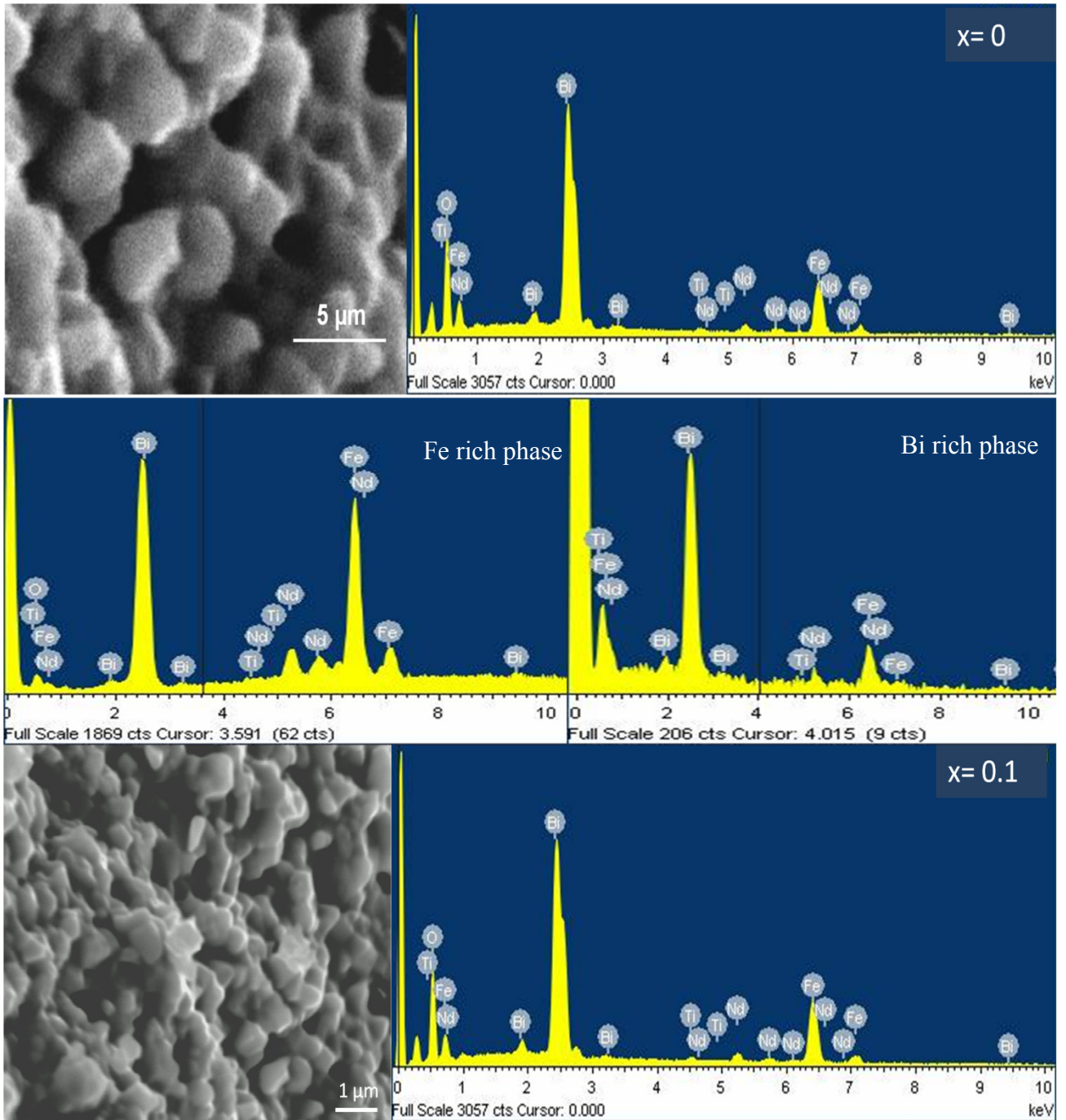
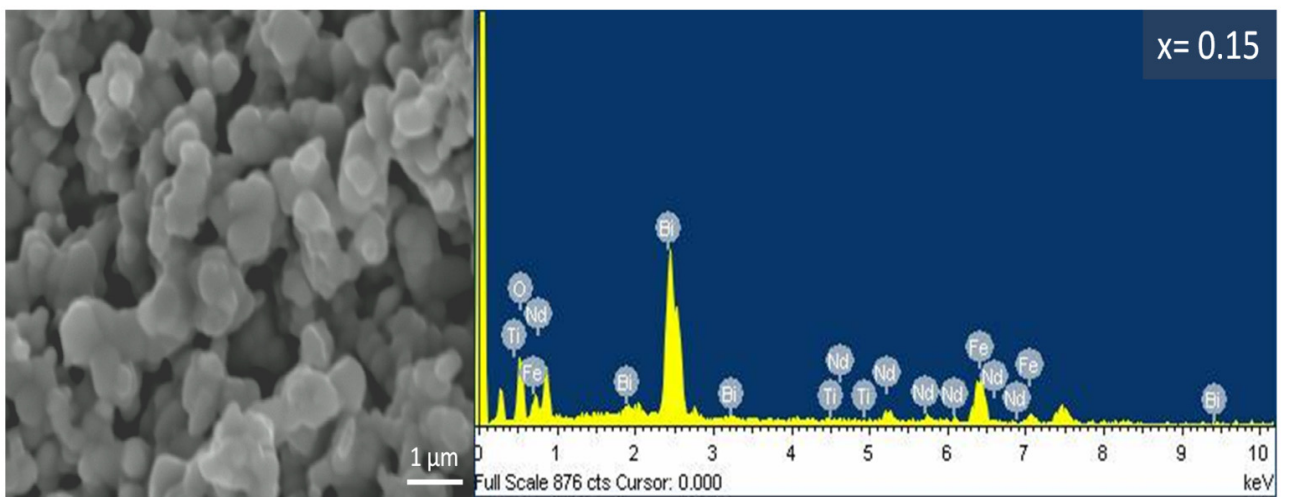
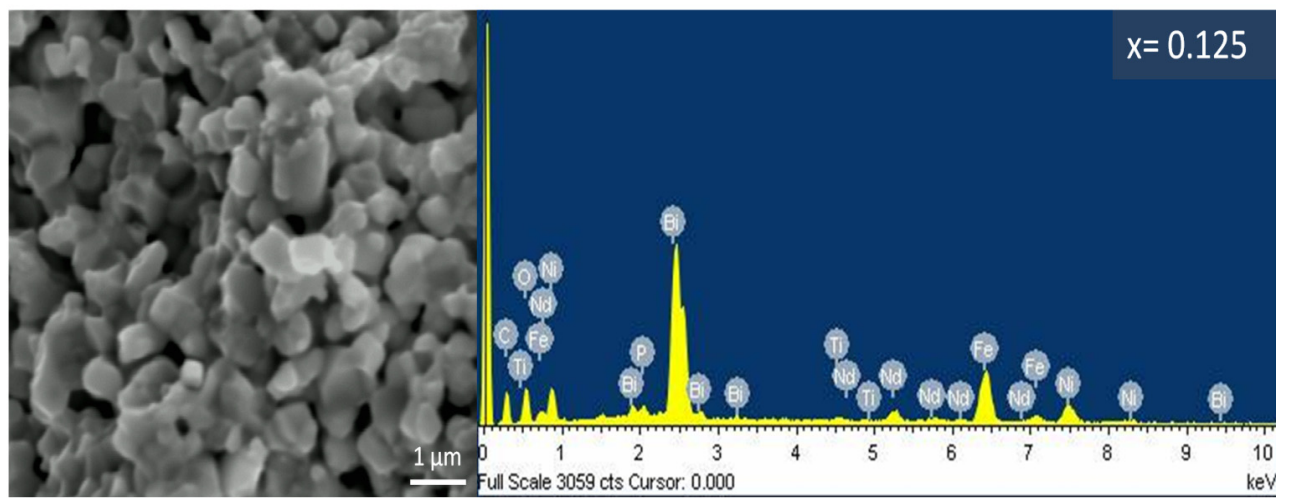
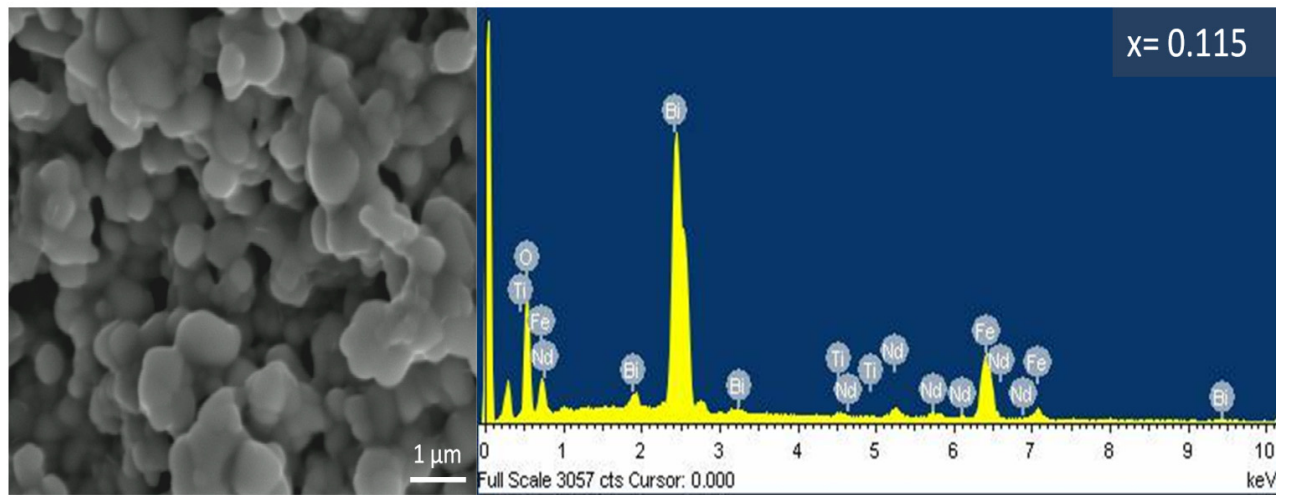


Figure 6.1: Room temperature XRD patterns of $\text{Bi}_{1-x}\text{Nd}_x\text{Fe}_{0.97}\text{Ti}_{0.03}\text{O}_3$. Indices for $x = 0$, 0.15 and 0.25, correspond to the rhombohedral, FE (R3c), the PbZrO_3 -like, AFE (Pbam), and the orthoferrite, PE (Pnma) structures, respectively.

6.3. Microstructure

Secondary electron images of fractured surfaces and EDS traces of $\text{Bi}_{1-x}\text{Nd}_x\text{Fe}_{0.97}\text{Ti}_{0.03}\text{O}_3$ ($0 \leq x \leq 0.25$) ceramics are presented in Figure 6.2. Some secondary phases (arrowed) are observed for samples with $x = 0$, consistent with the XRD data. These phases were either Bi-rich or Fe-rich compared with the matrix phase. For $0.1 \leq x \leq 0.25$, no secondary phases were observed, as SEM backscattered images and EDS traces from different positions were identical within experimental error. The grain size is approximately $2 \mu\text{m}$ for $x = 0$ but reduces to $< 1 \mu\text{m}$ for $0.1 \leq x \leq 0.25$.





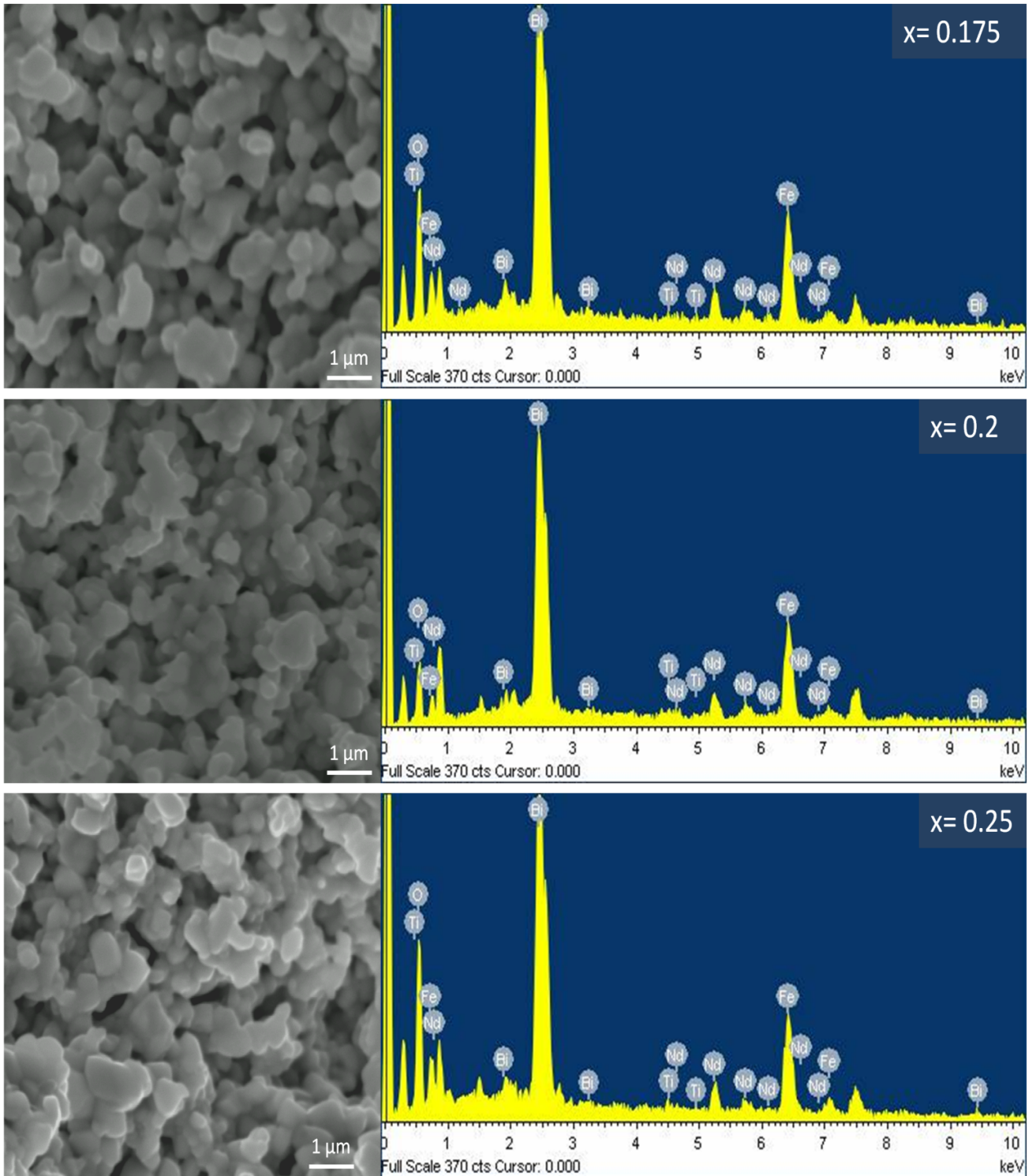


Figure 6.2: Secondary scanning electron micrographs of 3%Ti-doped $\text{Bi}_{1-x}\text{Nd}_x\text{FeO}_3$ along with their associated EDS traces.

6.4. Raman Spectroscopy

Room temperature Raman spectra of $\text{Bi}_{1-x}\text{Nd}_x\text{Fe}_{0.97}\text{Ti}_{0.03}\text{O}_3$ ceramics as a function of composition are shown in Figure 6.3. The spectra were corrected for the Bose–Einstein temperature factor and evaluated in a comparative manner to determine the onset of the phase transitions as a function of composition. For ceramics with $x \leq 0.115$, the spectra exhibit features characteristic of the rhombohedral structure associated with the BiFeO_3 end member, specifically the strong mode and its shoulder at $140\text{--}170\text{ cm}^{-1}$ and the doublets at $230\text{--}270\text{ cm}^{-1}$ and $470\text{--}530\text{ cm}^{-1}$ [5]. For compositions with $0.15 \leq x \leq 0.2$, the spectra are characteristic of the PZ-like phase and are identical to those reported by Karimi *et al.* [5]. The PZ-like phase is characterised by a broad mode at $\sim 180\text{ cm}^{-1}$. Samples with $x = 0.125$ exhibited modes consistent with both rhombohedral and PZ-like phases and thus were considered to lie on an AFE/FE phase boundary in agreement with the XRD data, Figure 6.1. For ceramics with $x = 0.25$, all modes within the spectra were consistent with those of the orthoferrite phase reported by Karimi *et al.* [5].

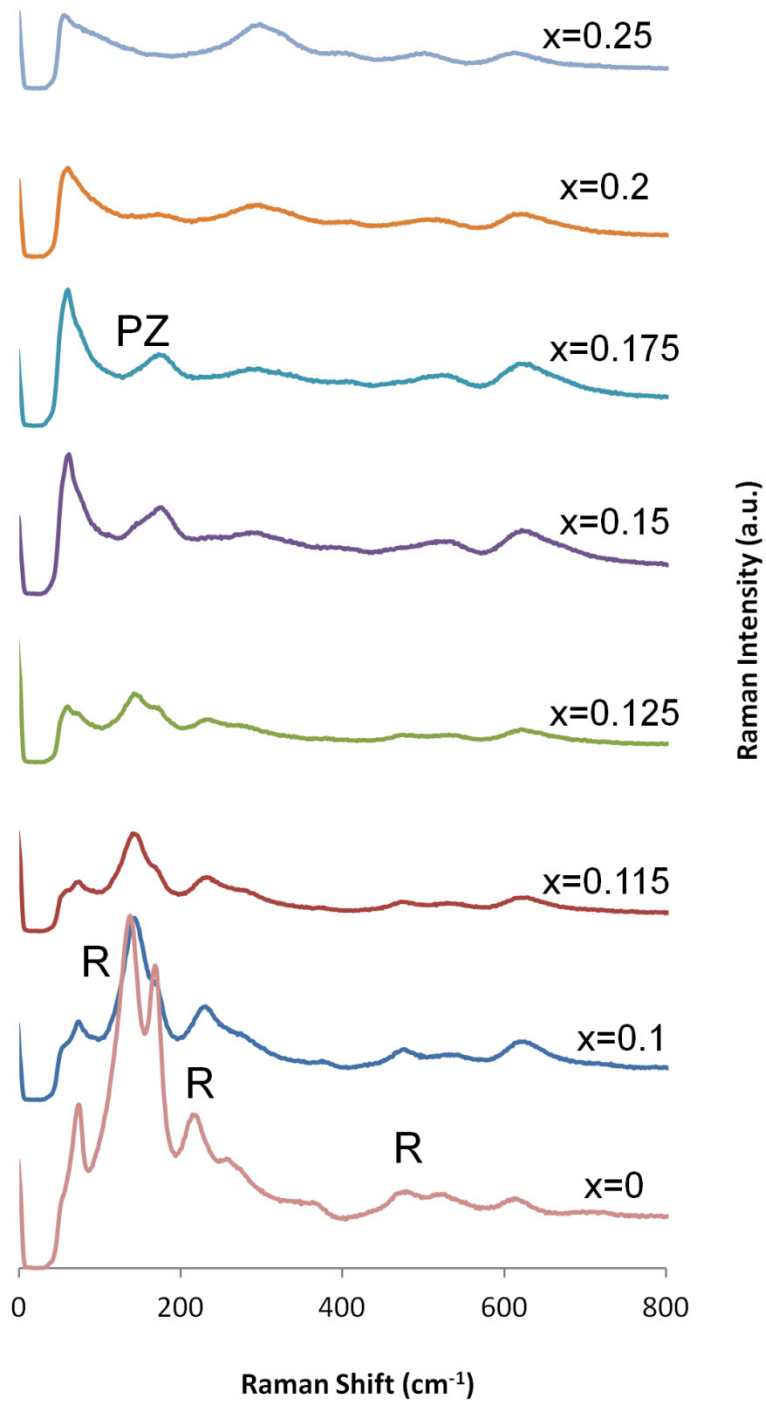


Figure 6.3: Room temperature Raman spectra of $\text{Bi}_{1-x}\text{Nd}_x\text{Fe}_{0.97}\text{Ti}_{0.03}\text{O}_3$ ceramics. Characteristic R3c and PZ-like modes are indicated by R and PZ, respectively.

6.5. Thermal Analysis

6.5.1. Differential Scanning Calorimetry (DSC)

Differential scanning calorimetry (DSC) data for $x = 0$ are shown in Figure 6.4. Two distinct transition temperatures are observed at 836 °C and 816 °C. Undoped BFO transforms from a ferroelectric (R3c) to paraelectric (Pbnm) phase at approx. 1100 K (827 °C) with a further paraelectric – paraelectric octahedral tilt transition at 835 °C [13]. As discussed in Section 5 (figure 5.7), Ti-doping decreases T_C in BNFO ceramics and it is reasonable to assume that the same effect is observed in BFO. It is proposed therefore, that the lower temperature peak at 816 °C corresponds to the ferroelectric R3c to paraelectric Pbnm phase transition whereas the peak at 835 °C is within the paraelectric phase and is associated with octahedral tilting. The antiferromagnetic phase transition is barely visible in the DSC data as a small change in slope at ~ 350 °C.

DSC curves for $\text{Bi}_{1-x}\text{Nd}_x\text{Fe}_{0.97}\text{Ti}_{0.03}\text{O}_3$ $0.1 \leq x \leq 0.25$ ceramics are shown in Figure 6.5. The prominent peaks correspond to the phase transition from either the paraelectric (PE) to the polar (FE) or antipolar (AFE) states (T_C) and the weaker peaks at ~ 350 °C relate to T_N [14]. As the Nd concentration increases, T_C decreases, with $x = 0.25$ presumably exhibiting a subambient transformation and thus outside the range of the present instrumentation. In BFO, the highly polarisable Bi^{3+} ion (6.12 \AA^3) is largely responsible for ferroelectricity and is displaced away from the centrosymmetric position relative to the adjacent oxygen ions. As the Nd concentration increases, substitution of Bi^{3+} by the less polarisable Nd^{3+} ion (5.01 \AA^3) [15] reduces the average A-site polarisability and thus T_C decreases. Simultaneously, the tolerance factor,

$$t = (\text{R}_A + \text{R}_O) / \sqrt{2(\text{R}_B + \text{R}_O)} \quad (6.1)$$

where R_A, R_B and R_O are the ionic radii of the A, B and O sites, decreases since Nd^{3+} (1.27 \AA) is smaller than Bi^{3+} (1.35 \AA) [16]. Karimi *et al.* postulated the combination of decreasing polarisability and tolerance factor with an increase in Nd concentration

replicated the conditions which occur as the Zr concentration increases across the FE/AFE boundary in $\text{Pb}(\text{Zr,Ti})\text{O}_3$ (PZT) and thus the PZ-like AFE phase is stabilised.

In contrast to the linear trend for T_C , T_N is almost invariant with composition, affirming that the Fe^{3+} sublattice is primarily responsible for the magnetic properties in this temperature range [17, 18]. Table 6.1 lists the latent heats associated with the structural transitions observed by DSC which are plotted against composition in Figure 6.6. The latent heat decreases linearly with increasing Nd concentration. Note that the ferroelectric-paraelectric phase transition latent heat reported for BFTO is 1.08 kJ/mole, which does not follow the trend in table 6.1 and Figure 6.6. It should be noted however, that BFTO ceramics exhibit two transitions and their total latent heat (2.75 kJ/mole) fits the overall linear trend exhibited by Nd doped compositions, Figure 6.6. This observation requires further study to assess whether this is merely coincidental or if it represents further insight into the nature of phase transitions in BFO ceramics.

Table 6.1: Latent heat associated with the phase transition at T_C for 3% Ti-doped $\text{Bi}_{1-x}\text{Nd}_x\text{FeO}_3$.

x	0 (816°C)	0 (835°C)	0.1	0.115	0.125	0.15	0.175	0.20
ΔH_{T_C} (kJ/mol)	1.08(08)	1.67(24)	1.97(14)	1.74(16)	1.66(11)	1.20(15)	0.73(05)	0.21(03)

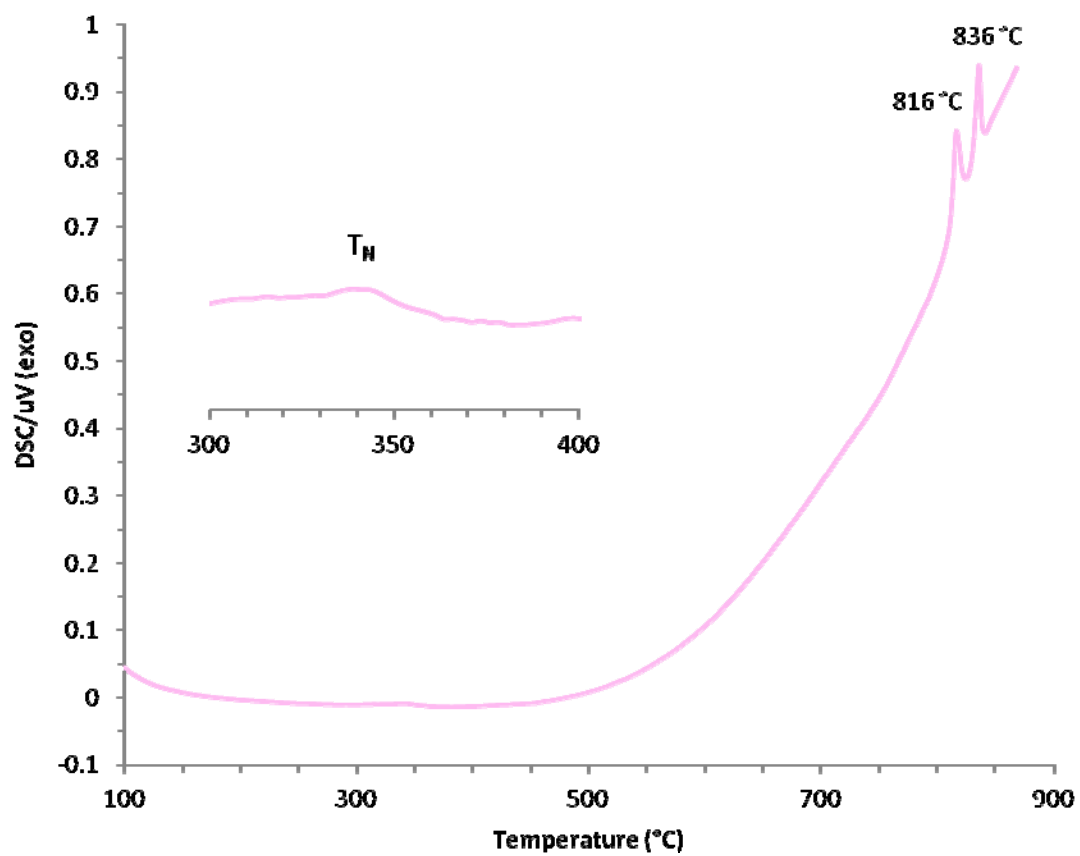


Figure 6.4: DSC trace of BFTO ceramics, revealing two different structural anomalies.

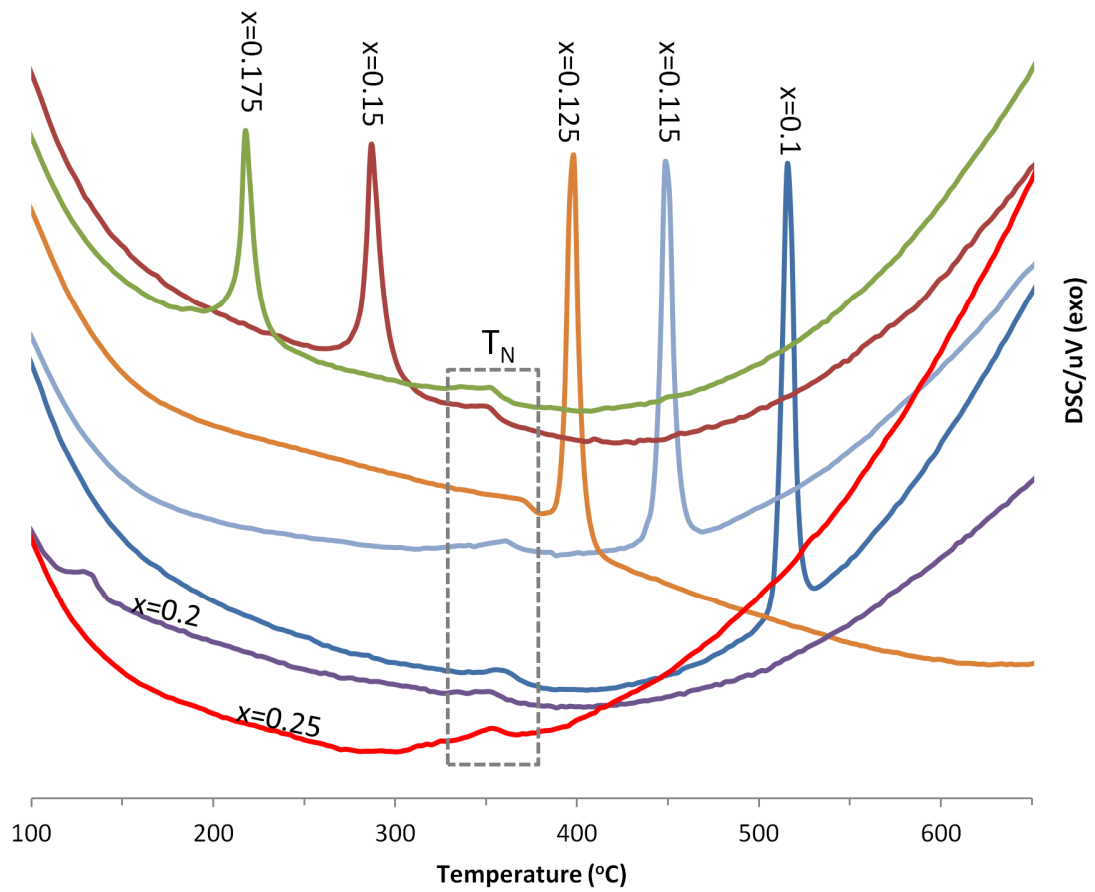


Figure 6.5: DSC curves of $\text{Bi}_{1-x}\text{Nd}_x\text{Fe}_{0.97}\text{Ti}_{0.03}\text{O}_3$ ceramics. T_N for the ceramics is indicated within the boxed region of the plot.

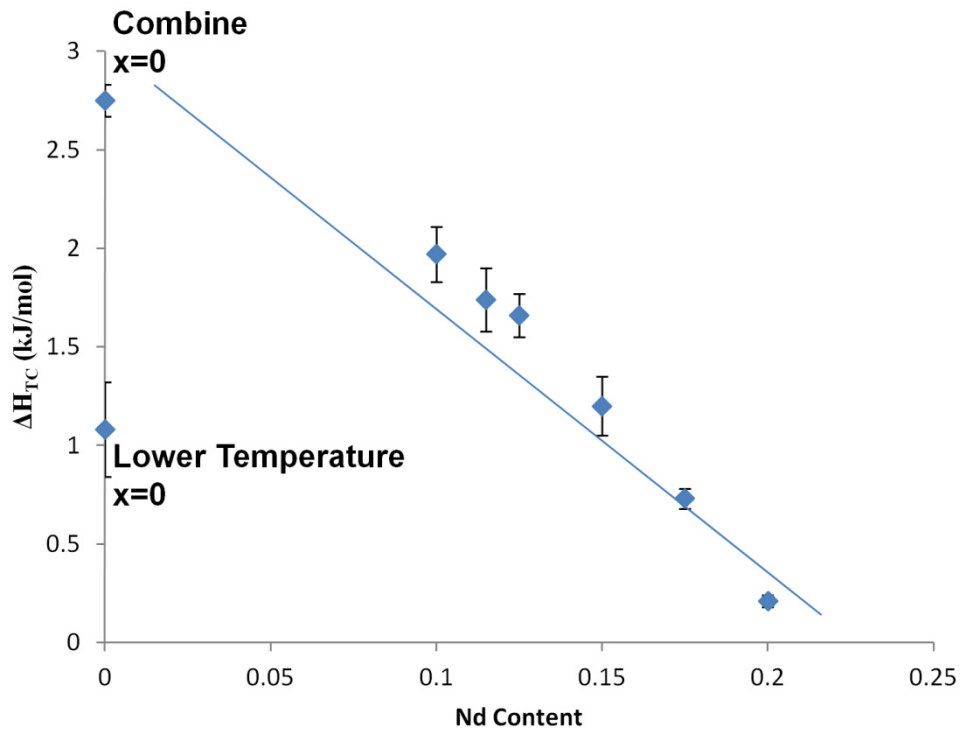


Figure 6.6: Latent heat vs. composition for Ti-doped $\text{Bi}_{1-x}\text{Nd}_x\text{FeO}_3$. Error bars correspond to standard deviation of the latent heats obtained from different DSC heating cycles.

6.5.2. Dilatometry

Dilatometry curves from Ti-doped $\text{Bi}_{1-x}\text{Nd}_x\text{FeO}_3$ $0.1 \leq x \leq 0.25$ ceramics are shown in Figure 6.7. Away from T_C all ceramics show an approximately linear thermal expansion. However, at T_C , there is a considerable volume change in agreement with the structural refinements of Levin and co-workers [8, 19]. As expected, no abrupt change in linear expansion is observed for $x = 0.25$ above room temperature since it remains paraelectric (PE) throughout the temperature range investigated. Dilatometry curves for $x = 0$ were not obtained since the phase transition temperatures were close to the melting temperature of BFO and consequently the risk of damage to equipment was a major concern. Although the volume change has been discussed in detail by Levin and co-workers [19] from a structural perspective, it is worth commenting further on its extraordinary magnitude and the sharpness of the structural transitions which give rise to the volume change. The latent heats associated with the transitions in Ti-doped $\text{Bi}_{1-x}\text{Nd}_x\text{FeO}_3$

$x\text{Nd}_x\text{FeO}_3$ ($0.1 \leq x \leq 0.15$) ceramics (Table 6.1, Figure 6.8) are broadly similar to PZT (1-3 kJ/mol) [20, 21] but an order of magnitude larger than BaTiO_3 (BT, 0.2 kJ/mol) [22, 23]. The latent heat however, decreases to values comparable with BaTiO_3 for $x = 0.2$. The volume change ($\sim 2\%$) [19], elucidated here in Figure 6.7, is however greater than that associated with, e.g. PbTiO_3 (0.6%) [24].

The fundamental difference between phase transitions in RE-doped BiFeO_3 compositions compared with PZT and BT is that for BT and PZT the PE phase is cubic (Pm3m) but in RE-doped BiFeO_3 , it is orthorhombic (Pnma) [5, 19]. Thus, the PE phase in RE-doped BiFeO_3 is already heavily distorted away from cubic symmetry before the onset of the polar/antipolar transition. The Pnma, orthoferrite cell has an $a^-a^-c^+$ Glazer tilt system [25] in which not only is the oxygen sublattice heavily distorted by a combination of antiphase and in-phase rotations but also the A-site cations are displaced in an antiparallel configuration. The transition from the PE to the polar FE state requires that the cation displacements are rearranged from antiparallel to a parallel configuration and also that the octahedral distortions reorient so that the rotations are only in antiphase around the $[111]_p$ axis [19]. The transition from PE to the antipolar state is also associated by striking changes in the tilt system and cation displacements. Hence, the volume changes are large (2%) [19] in comparison with conventional PE-FE transitions in ferroelectrics such as BT and PZT [24]. The large volume change and 1st order character of the structural phase transitions in Ti-doped $\text{Bi}_{1-x}\text{Nd}_x\text{FeO}_3$ result in an avalanche-like distortion which rapidly spreads throughout the ceramic, resulting in unusually sharp thermal anomalies. Such sharp anomalies are normally observed only for the end member compounds of a solid solution, e.g. PZ and PT in PZT, whilst compositions within the solid solution generally exhibit broad anomalies due to the distribution of the cations.

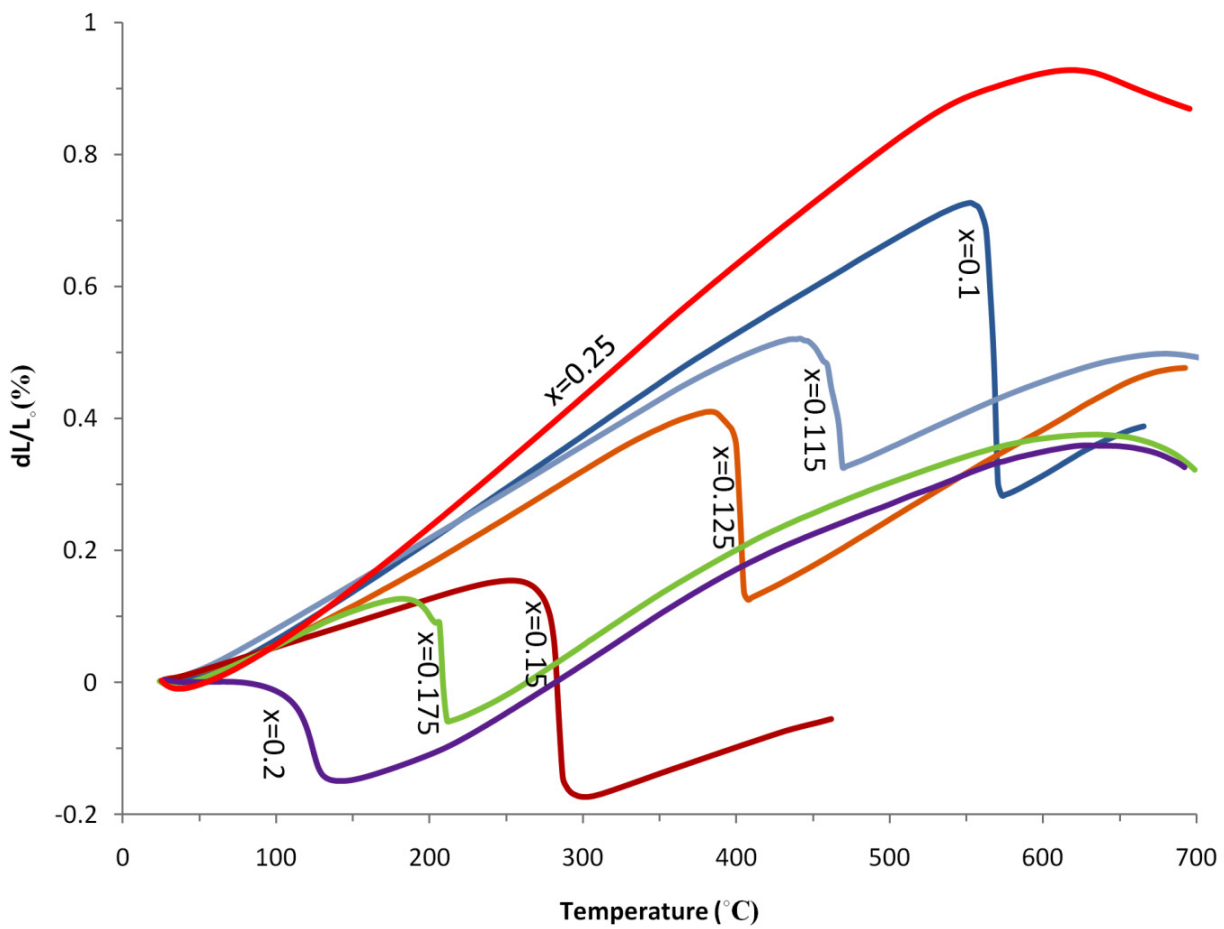


Figure 6.7: Dilatometry curves of Ti-doped $\text{Bi}_{1-x}\text{Nd}_x\text{FeO}_3$ ceramics. The anomalies correspond well to those observed by DSC.

6.6. Electrical Measurements

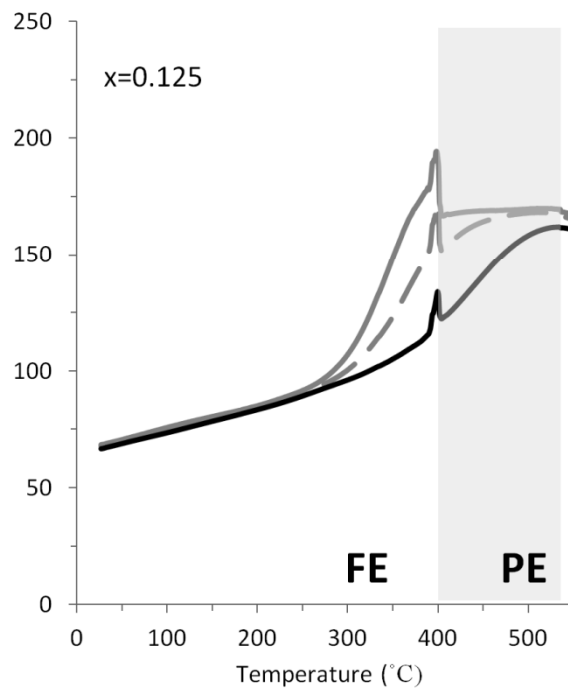
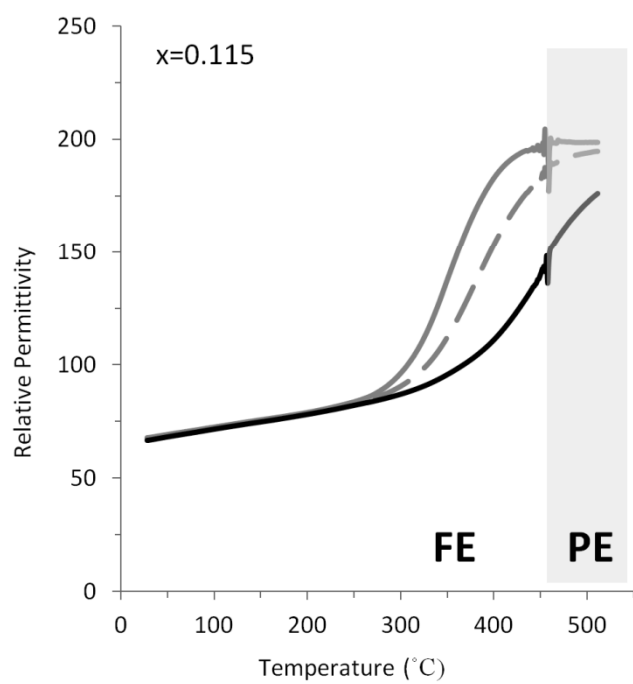
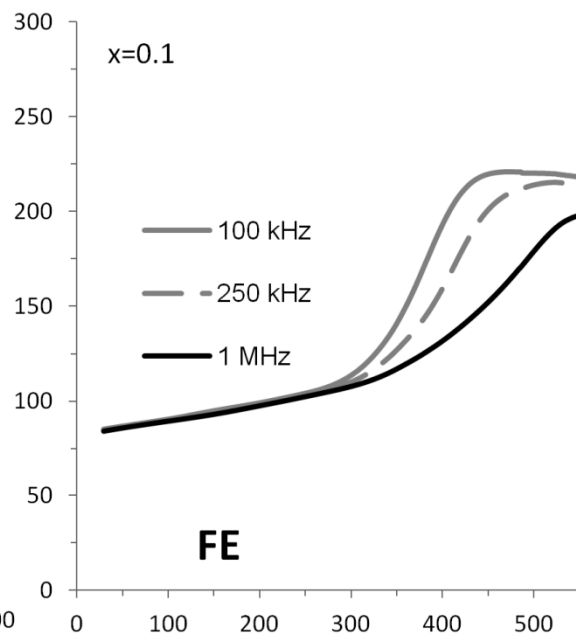
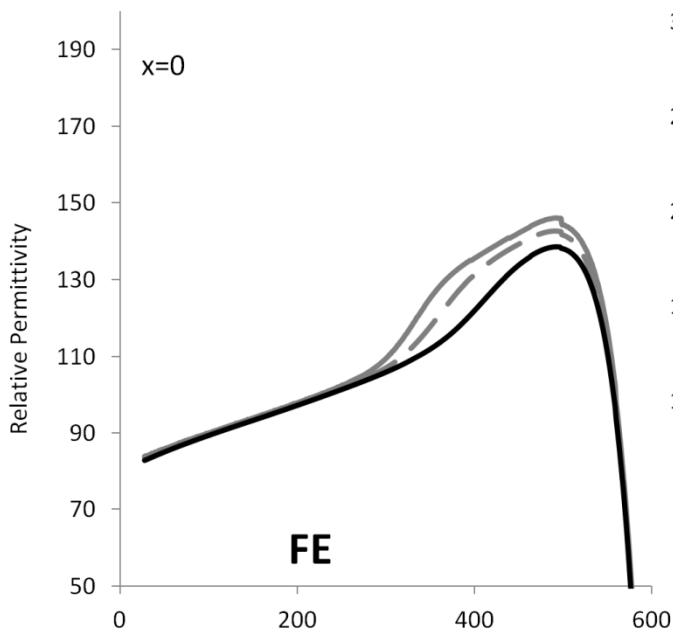
Despite large volume changes and sharp anomalies in latent heat associated with the structural transitions in RE-doped BiFeO_3 , there has been little evidence presented to date in the scientific literature of their presence in dielectric data as a function of temperature, presumably because the conductivity of these systems has been hitherto too high to obtain reliable dielectric measurements.

Figure 6.8 presents the permittivity vs. temperature curves for Ti-doped $\text{Bi}_{1-x}\text{Nd}_x\text{FeO}_3$ samples at different frequencies. There is no peak observed in $x = 0$ and 0.1 despite clear anomalies at 816°C and 520°C , respectively, in the DSC and dilatometry data. This is due to the high level of conductivity at temperatures $> 500^\circ\text{C}$, despite Ti-doping. For samples with $x = 0.115$, a weak but sharp anomaly in permittivity is observed which is coincident with those in the thermal analysis data presented in Figures 6.5 and 6.7. However, the phase transition is superimposed on a dielectric relaxation in the range $250 - 450^\circ\text{C}$ which is evident for all the samples. For $x = 0.125$, a doublet peak is observed in the dielectric data at a temperature coincident with anomalies in the DSC and dilatometry traces. The two peaks can be explained by considering that this composition lies at the phase boundary between the FE (R3c) and AFE (Pbam) structures and the anomalies correspond to either PE-FE, PE-AFE or FE-AFE transitions. At room temperature, $x = 0.125$ remains mixed phase, according to XRD (Figure 6.1) and Raman data (Figure 6.3) implying that the FE phase does not transform directly to AFE and that the two anomalies for $x = 0.125$ are most likely PE-FE and PE-AFE transitions occurring in different regions of the sample.

For samples with $0.15 \leq x \leq 0.2$ (Pbam, AFE), a step-like change in permittivity is observed, coincident in temperature with anomalies in DSC and dilatometry curves. In PZT, the nearest analogue to RE-doped BiFeO_3 systems, a PE-AFE transition is expected only for pure PZ from the phase diagram. However, it has been shown that small impurity and defect concentrations result in a PE-FE transformation in PZ prior to a step-like dielectric anomaly to the AFE phase [26]. The inevitable presence of impurities and defects has thus made the observation of a genuine PE – AFE transition

elusive for PZ ceramics [26] and single crystals [27]. Hence, there is no real point of comparison in the literature to determine whether the step-like behaviour in dielectric data for RE-doped BiFeO₃ is typical of a PE-AFE transition. Intuitively however, the transition from a non-polar PE to an antipolar AFE state would not be expected to give rise to a large peak in permittivity. For $x = 0.25$ the transition is potentially sub-ambient but further studies are required to determine whether these materials transform to the AFE structure on cooling or remain PE.

The dielectric relaxation in the vicinity of the T_N in BiFeO₃-based materials has been attributed either to coupling of the orientation of the magnetization to the ferroelastic strain [28] or Maxwell-Wagner behaviour arising from space charge polarization [29]. Jun and co-workers [11] observed a similar relaxation in Nb-doped BiFeO₃ ceramics, where the high resistivity allowed measurement of the intrinsic dielectric response. In the present work, assuming that the cause of the dielectric dispersion is the same for all compositions, we can exclude magnetoelectric coupling as the origin since for $x = 0.2$ and 0.25 the frequency dispersion occurs within the paraelectric state. Such anomalies have also been reported in antiferromagnetic systems such as the rare earth manganites [30, 31, 32] and Bi₂Fe₄O₉ [33] in the vicinity of T_N . In single crystal studies, authors have reported a frequency independent weak permittivity anomaly for directions that are in-plane with the antiferromagnetic ordering and a well-pronounced permittivity relaxation along out-of-plane crystallographic directions. The frequency independent dielectric anomaly in ReMnO₃ was attributed by Katsufuji *et al.* [31] to a spin-dependent charge-transfer gap between Mn $3d$ and in-plane oxygen $2p$ states with strong p - d exchange interaction, making the dominant factor for the permittivity change the nearest-neighbour spin correlation function, $\langle S_i S_j \rangle$, where i and j denote the neighbouring Mn sites. The strong dielectric relaxation was analysed by Park *et al.* [33] for Bi₂Fe₄O₉ and discussed in terms of a Maxwell-Wagner relaxation, with the authors noting that it is peculiar why such behaviour would be observed only in a particular crystal direction. The explanations presented above may well be applicable here; however, the polycrystalline nature of the samples does not allow us to distinguish between contributions from different crystallographic directions.



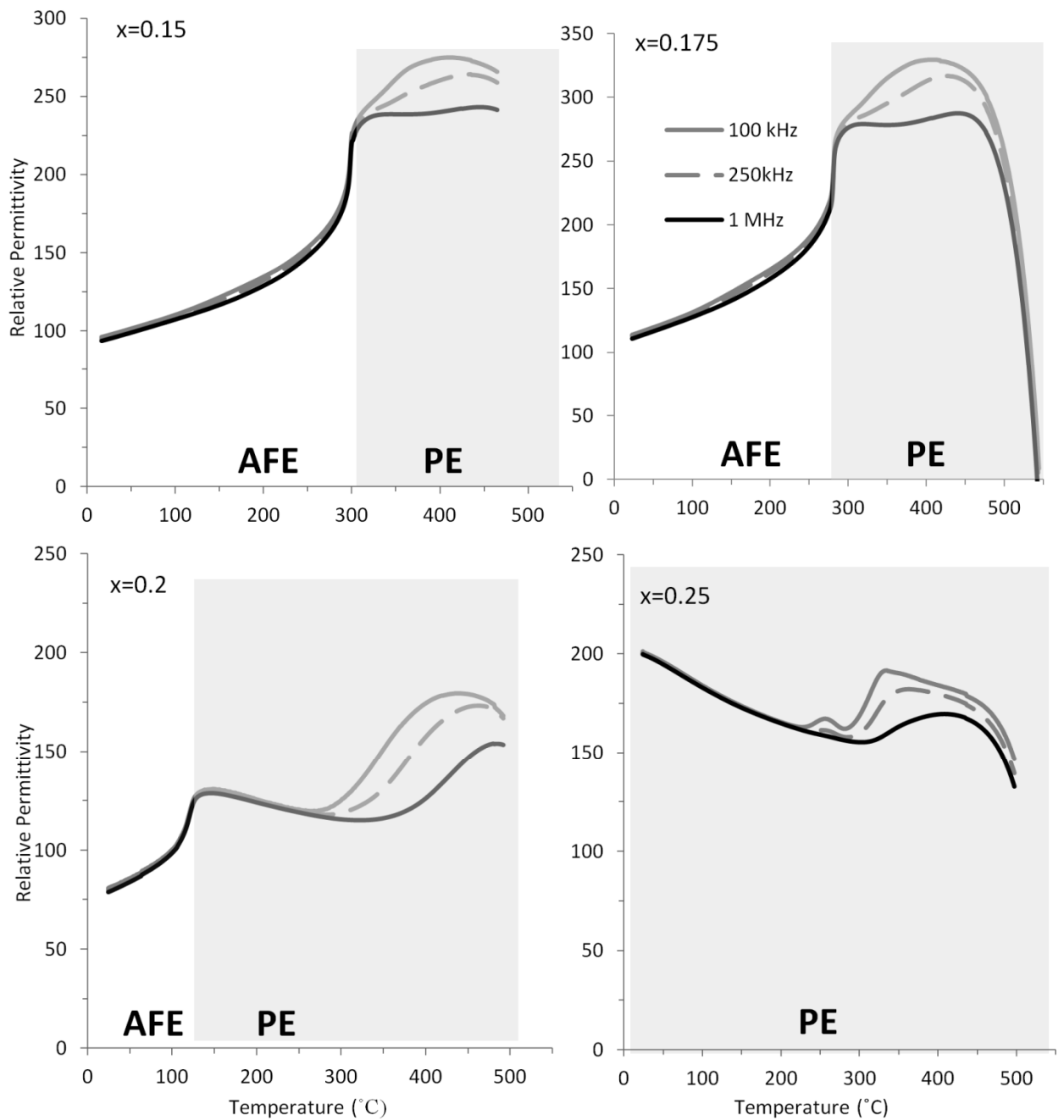


Figure 6.8: Permittivity versus temperature curves for 3% Ti-doped $\text{Bi}_{1-x}\text{Nd}_x\text{FeO}_3$ ceramics.

Figure 6.9 shows a comparison between permittivity vs. temperature results of Ti-doped $\text{Bi}_{1-x}\text{Nd}_x\text{FeO}_3$. The step-like phase transitions for $x = 0.15, 0.175$ and 0.2 can be easily observed. For the sample $x = 0.125$, the FE-PE phase transition can be observed as a peak at 400°C . The $x = 0.25$ sample is paraelectric at room temperature so no phase transition can be observed.

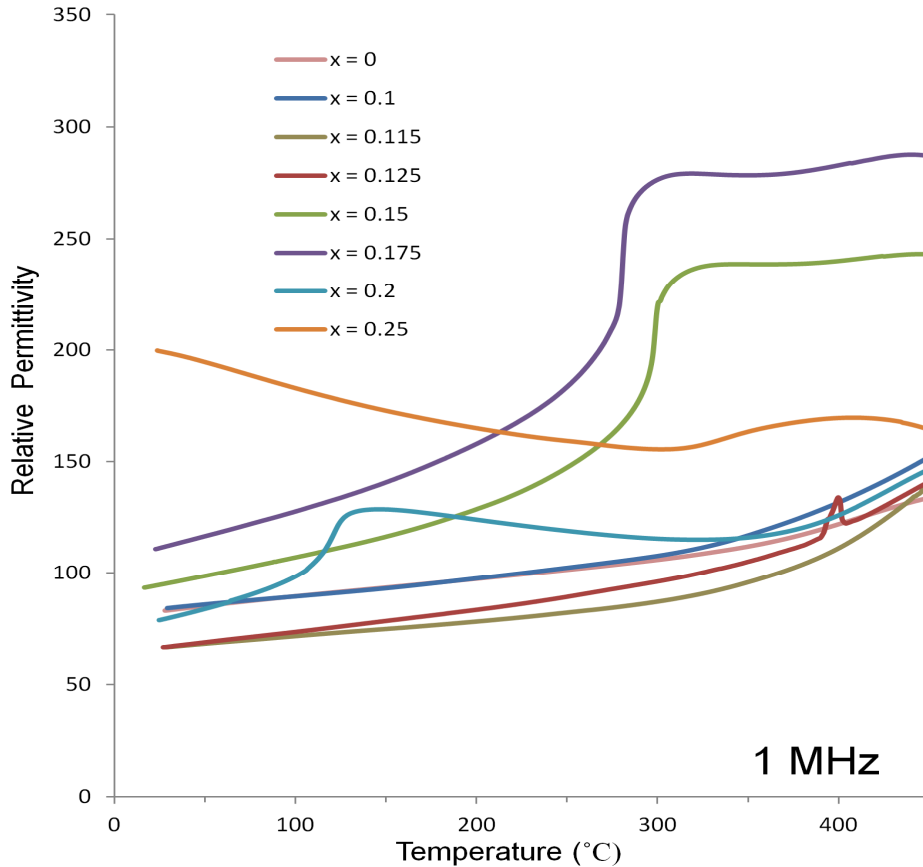


Figure 6.9: Comparison between permittivity versus temperature behaviour of $\text{Bi}_{1-x}\text{Nd}_x\text{Fe}_{0.97}\text{Ti}_{0.03}\text{O}_3$ ceramics at 1MHz.

The dielectric loss of all samples is less than 0.03 up to 300°C , above which it sharply rises, presumably as the conductivity increases, coincident with the large frequency dependent anomaly, Figure 6.10.

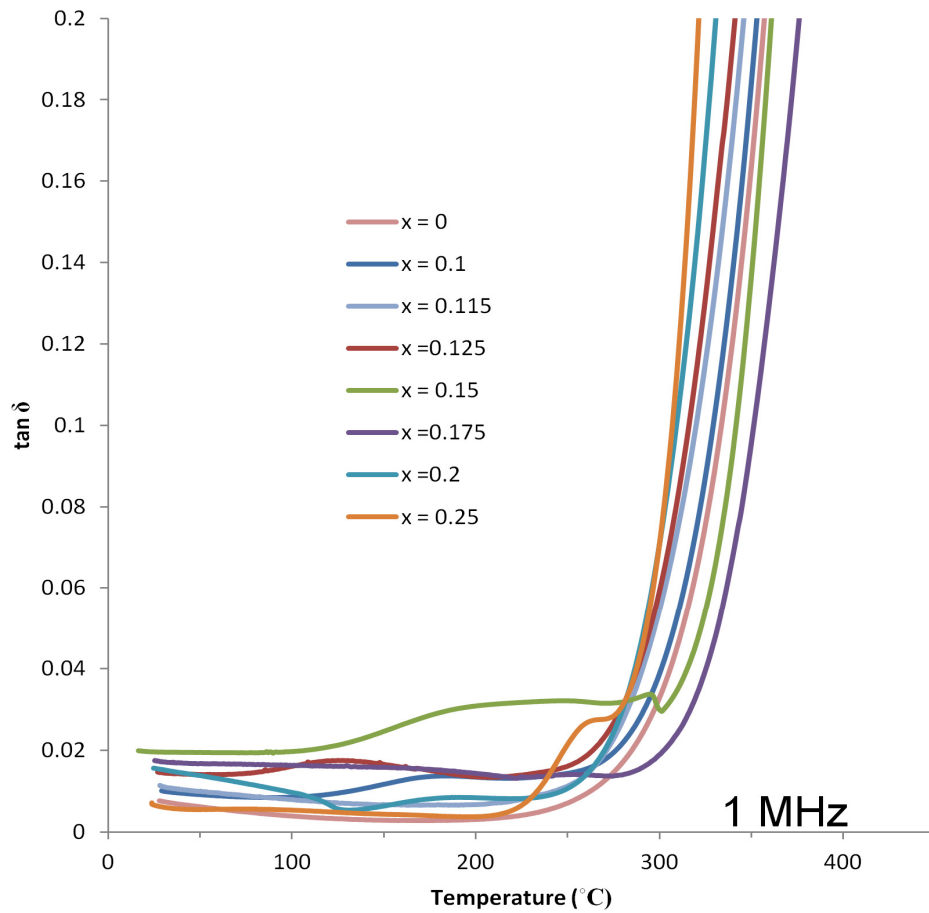


Figure 6.10: Dielectric loss versus temperature for $\text{Bi}_{1-x}\text{Nd}_x\text{Fe}_{0.97}\text{Ti}_{0.03}\text{O}_3$ ceramics at 1MHz.

Impedance spectroscopy was performed to further investigate the bulk electrical properties of 3%Ti doped BiNdFeO_3 ceramics, Figure 6.11. Ceramics were all resistive compared to undoped BiFeO_3 . The conductivity increased slightly with increasing Nd concentration. $x = 0$ (not shown here) does not follow this trend because BFTO ceramics contain impurity phases that are thought to be conductive [11, 12].

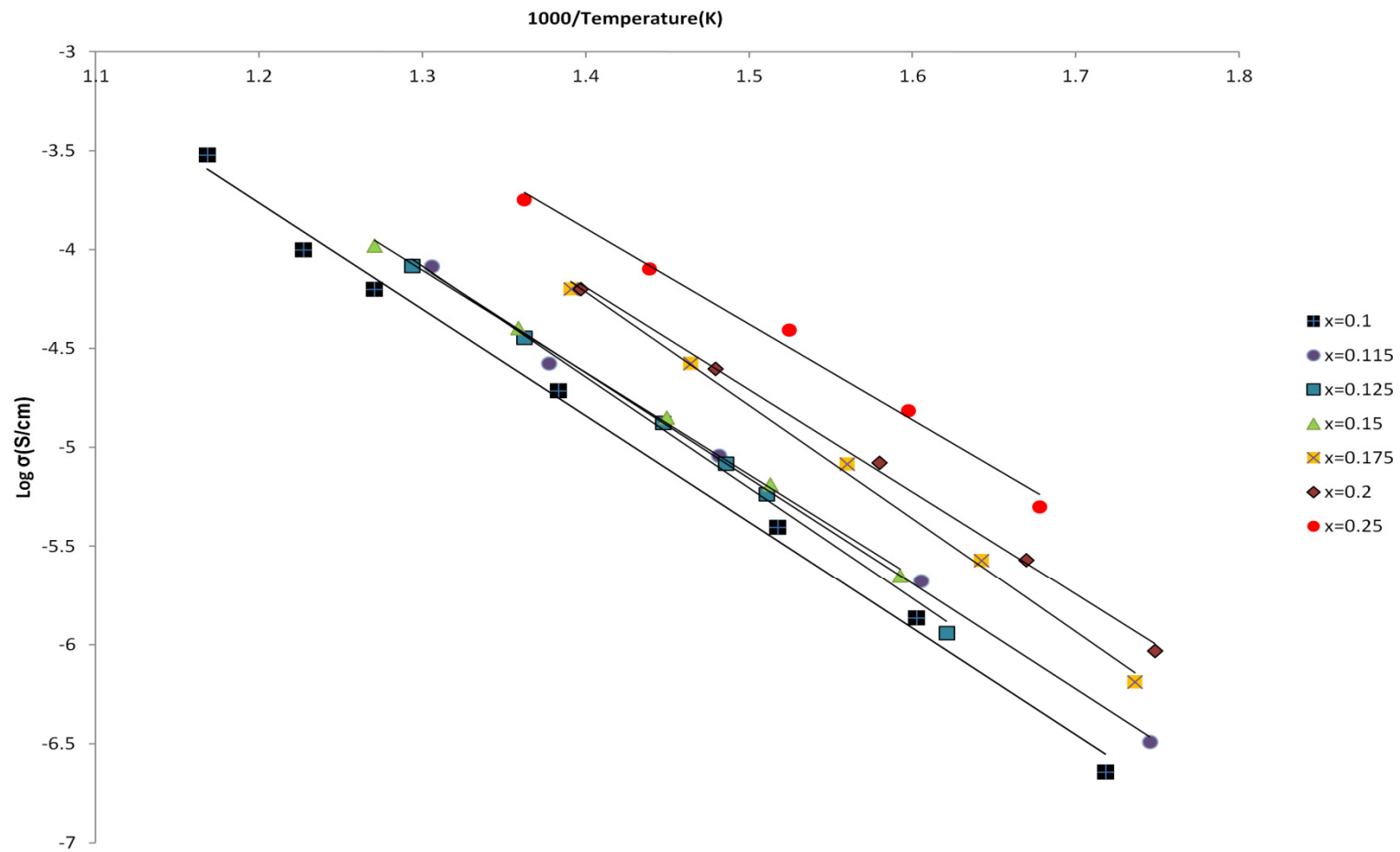


Figure 6.11: Arrhenius plot of 3% Ti-doped $\text{Bi}_{1-x}\text{Nd}_x\text{FeO}_3$ ceramics.

A summary of the FE/PE or AFE/PE phase transition temperatures as obtained from DSC, dilatometry and the permittivity measurements is given in Figure 6.12. The values are in good agreement in general, taking into account that these techniques study different physical phenomena. Assuming a linear decrease in T_C with Nd content, gives an extrapolated T_C of $-85\text{ }^\circ\text{C}$ for $x = 0.25$.

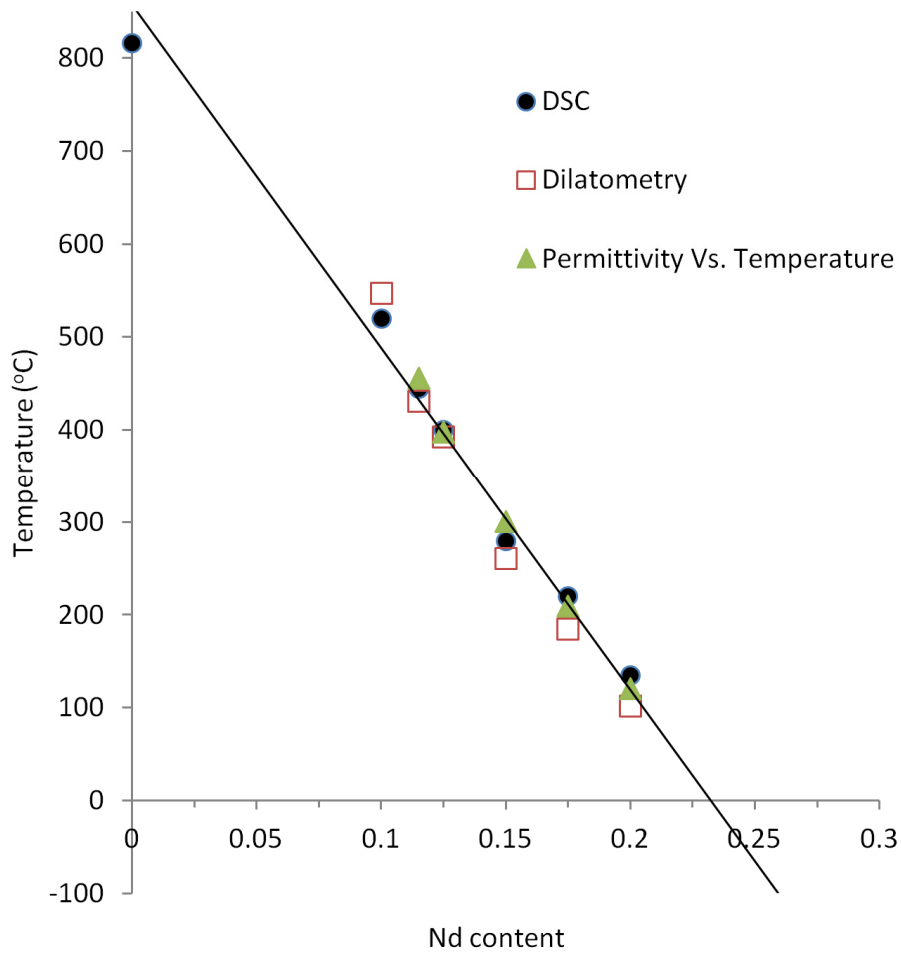


Figure 6.12: Plot of T_C versus Nd content obtained from DSC, dilatometry and dielectric measurements.

6.7. Conclusions

Compositions within the solid solution $\text{Bi}_{1-x}\text{Nd}_x\text{Fe}_{0.97}\text{Ti}_{0.03}\text{O}_3$ were fabricated. $x = 0$ samples exhibited secondary phases but compositions with $x \geq 0.1$ were essentially single phase.

Samples with $x \leq 0.125$ were predominantly FE, rhombohedral (R3c) whereas for $0.15 \leq x \leq 0.2$, ceramics exhibited the AFE, PZ-like structure reported by Karimi *et al.* [3, 5]. Samples with $x = 0.25$ had the PE, orthoferrite structure. Compositions with $x = 0.125$ exhibited mixed phase denoting that they lay on the FE/AFE phase boundary but at no stage was there evidence of a FE-AFE transition, typically observed in PZT.

For $x \geq 0.125$, PE-FE or PE-AFE (depending on composition) phase transitions were observed within dielectric data as a function of temperature, accompanied by sharp changes in volume and latent heat as determined by dilatometry and DSC, respectively, for all values of x . The unusually sharp anomalies in permittivity, volume and latent heat are attributed to the discontinuous structural rearrangement of cation displacements and rotations of the O-octahedra at the PE-FE and PE-AFE transitions which result in avalanche-like transformations. A frequency dependent broad peak in permittivity was observed for all compositions between 250 °C and 450 °C, which requires further study.

It should be noted that several authors [34, 35 and 36] have reported promising room temperature trends in piezoelectric properties as a function of RE-dopant with a peak in piezoelectric coefficient in the FE phase adjacent to the FE/AFE boundary. The high T_C of RE-doped BiFeO_3 has fuelled speculation that they may well have applications as high temperature piezoelectrics. However, it is evident from the data presented here that whilst the dielectric relaxation dominates the response in the temperature range 250 – 450 °C and the dielectric loss remains of the order of 20 % above 300 °C, the potential of RE-doped BiFeO_3 for high temperature piezoelectric applications is highly speculative. It is recommended that future studies should focus on the source of the relaxation and its eradication.

References

1. K. Kalantari, I. Sterianou, S. Karimi, M. C. Ferrarelli, S. Miao, D. C. Sinclair, and I. M. Reaney, *Ti Doping to reduce conductivity in $\text{Bi}_{0.85}\text{Nd}_{0.15}\text{FeO}_3$ ceramics*, **2011**, Adv. Funct. Mater. 21, 3737.
2. S. Phapale, R. Mishra, and D. Das, *Standard enthalpy of formation and heat capacity of compounds in the pseudo-binary $\text{Bi}_2\text{O}_3\text{-Fe}_2\text{O}_3$ system*, **2008**, J. Nucl. Mater. 373, 137.
3. S. Karimi, I. M. Reaney, I. Levin, and I. Sterianou, *Nd-doped BiFeO_3 ceramics with antipolar order*, **2009**, Appl. Phys. Lett. 94, 112903.
4. C. Fanggao, S. Guilin, F. Kun, Q. Ping, and Z. Qijun, *Effect of Gadolinium substitution on dielectric properties of bismuth ferrite*, **2006**, J. Rare Earths 24, 273.
5. S. Karimi, I. Reaney, Y. Han, J. Pokorny, and I. Sterianou, *Crystal chemistry and domain structure of rare-earth doped BiFeO_3 ceramics*, **2009**, J. Mater. Sci. 44, 5102.
6. V.A. Khomchenko, D.A. Kiselev, J.M. Vieira, L. Jian, A.L. Kholkin, A.M.L. Lopes, Y.G. Pogorelov, J.P. Araujo, M. Maglione, *Effect of diamagnetic Ca, Sr, Pb, and Ba substitution on the crystal structure and multiferroic properties of the BiFeO_3 perovskite*, **2008**, J. App. Phys., 103, 024105
7. D. Maurya, H. Thota, A. Garg, B. Panday, P. Chand, H.C. Verma, *Magnetic studies of multiferroic $\text{Bi}_{1-x}\text{Sm}_x\text{FeO}_3$ ceramics synthesized by mechanical activation assisted processes*, **2009**, J.Phys: Condens, Matter 21, 026007.
8. I. Levin, S. Karimi, V. Provenzano, C. L. Dennis, H. Wu, T. P. Comyn, T. J. Stevenson, R. I. Smith, and I. M. Reaney, *Reorientation of magnetic dipoles at the antiferroelectric-paraelectric phase transition of $\text{Bi}_{1-x}\text{Nd}_x\text{FeO}_3$ ($0.15 \leq x \leq 0.25$)*, **2010**, Phys. Rev. B 81, 020103.

9. K. Kalantari, I. Sterianou, D.C. Sinclair, P.A. Bingham, J. Pokorný and I.M. Reaney, *Structural phase transitions in Ti-doped Bi_{1-x}Nd_xFeO₃ ceramics*, **2012**, submitted to J. Appl. Phys.
10. K. Abe, N. Sakai, J. Takahashi, H. Itoh, N. Adachi, and T. Ota, *Leakage current properties of cation-substituted BiFeO₃ ceramics*, **2010**, Jpn. J. Appl. Phys., 49, 09MB01.
11. Y. K. Jun, W. T. Moon, C. M. Chang, H. S. Kim, H. S. Ryu, J. W. Kim, S. H. Hong, *Effects of Nb-doping on electric and magnetic properties in multi-ferroic BiFeO₃ ceramics*, **2005**, 135, 133-137.
12. B. Yu, M. Li, J. Wang, L. Pei, D. Guo, X. Zhao, *Enhanced electrical properties in multiferroic BiFeO₃ ceramics co-doped by La³⁺ and V⁵⁺*, **2008**, J. Appl. Phys., 41, 185401.
13. D. C. Arnold, K. S. Knight, F.d. Morrison, P. Lightfoot, *The ferroelectric-paraelectric transition in BiFeO₃ crystal structure of the orthorhombic β -phase*, **2009**, Phys. Rev. Lett., 102, 027602.
14. S. M. Selbach, T. Tybell, M.-A. Einarsrud, and T. Grande, *The ferroelectric phase transitions of BiFeO₃*, 2008, Adv. Mater. 20, 3692.
15. R. D. Shannon, *Dielectric polarizabilities of ions in oxides and fluorides*, **1993**, J. Appl. Phys. 73, 348.
16. R. D. Shannon, *Revised effective radii and systematic studies of interatomic distances in halides and chalcogenides*, **1976**, Acta Crystallogr., Sect. A 32, 751.
17. R. L. White, *Review of recent work on magnetic and spectroscopic properties of rare-earth orthoferrites*, **1969**, Appl. Phys. 40, 1061.
18. W. Sławiński, R. Przeniosło, I. Sosnowska, and E. Suard, *Spin reorientation and structural changes in NdFeO₃*, **2005**, J. Phys.: Condens. Matter 17, 4605.
19. I. Levin, *Displacive phase transitions and magnetic structures in Nd-substituted BiFeO₃*, **2010**, Chem. Mater. 23, 2166.

20. E. Sawaguchi, *Ferroelectricity versus antiferroelectricity in the solid solutions of PbZrO₃ and PbTiO₃*, **1953**, J. Phys. Soc. Jpn. 8, 615 (1953).
21. G. A. Rossetti, J. P. Cline, Y. M. Chiang, and A. Navrotsky, *Lattice energies and structural distortions in Pb(Zr_xTi_{1-x})O₃ solid solutions*, **2002**, J. Phys.: Condens. Matter 14, 8131.
22. S. Lee, Z.-K. Liu, M.-H. Kim, and C. A. Randall, *Probing local dipoles and ligand structure in BaTiO₃ nanoparticles*, **2007**, J. Appl. Phys. 101, 054119.
23. G. Shirane and A. Takeda, *Phase transitions in solid solutions of PbZrO₃ and PbTiO₃ .2. X-Ray study*, **1952**, J. Phys. Soc. Jpn. 7, 1, 12-18.
24. B. Jaffe, W. R. J. Cook and H. Jaffe, *Piezoelectric ceramics* **1971**, Academic Press, London.
25. A. M. Glazer, *The classification of tilted octahedral in perovskites*, **1972**, Acta. Cryst., B28, 3384.
26. G. Shirane and A. Takeda, *Phase transitions in solid solutions of PbZrO₃ and PbTiO₃ .1. small concentrations of PbTiO₃*, **1952**, J. Phys. Soc. Jpn. 7, 1, 5-11.
27. R. W. Whatmore and A. M. Glazer, *Structural phase transitions in lead zirconate*, **1979**, J. Phys. C-Solid State Phys. 12, 1505.
28. Z. X. Cheng, A. H. Li, X. L. Wang, S. X. Dou, K. Ozawa, H. Kimura, S. J. Zhang, and T. R. ShROUT, *Enhancement of ferroelectricity and ferromagnetism in rare earth element doped BiFeO₃*, **2008**, J. Appl. Phys. 103, 07E507.
29. V. Goian, S. Kamba, S. Greicius, D. Nuzhnyy, S. Karimi, and I. M. Reaney, *Terahertz and infrared studies of antiferroelectric phase transition in multiferroic Bi_{0.85}Nd_{0.15}FeO₃*, **2011**, J. Appl. Phys. 110, 074112.
30. T. Goto, T. Kimura, G. Lawes, A. P. Ramirez, and Y. Tokura, *Ferroelectricity and giant magnetocapacitance in perovskite rare-earth manganites*, **2004**, Phys. Rev. Lett. 92, 257201.
31. T. Katsufuji, S. Mori, M. Masaki, Y. Moritomo, N. Yamamoto, and H. Takagi, *Dielectric and magnetic anomalies and spin frustration in hexagonal RMnO₃ (R=Y, Yb, and Lu)*, **2001**, Phys. Rev. B 64, 104419.

32. F. Schrettle, P. Lunkenheimer, J. Hemberger, V. Y. Ivanov, A. A. Mukhin, A. M. Balbashov, and A. Loidl, *Relaxations as key to the magnetocapacitive effects in the perovskite manganites*, **2009**, Phys. Rev. Lett. 102, 207208.
33. A. Park, K. M. Song, K. D. Lee, C. J. Won, and N. Hur, *Effect of antiferromagnetic order on the dielectric properties of $\text{Bi}_2\text{Fe}_4\text{O}_9$* , **2010**, Appl. Phys. Lett. 96, 092506.
34. D. Kan, L. Palova, V. Anbusathaiah, C. J. Cheng, S. Fujino, V. Nagarajan, K. M. Rabe, and I. Takeuchi, *Universal behaviour and electric-field-induced transition in rare-earth substituted BiFeO_3* , **2010**, Adv. Funct. Mater. 20, 1108.
35. Z. Y. Zhong, Y. Sugiyama, and H. Ishiwara, *Large Remanent in Sm-substituted BiFeO_3 thin film formed by chemical solution deposition*, **2010**, Jpn. J. Appl. Phys. 49, 4.
36. I. O. Troyanchuk, D. V. Karpinsky, M. V. Bushinsky, O. S. Mantyskaya, N. V. Tereshko, and V. N. Shut, *Structural stability and magnetic properties of $\text{Bi}_{1-x}\text{La}(\text{Pr})_x\text{FeO}_3$ solid solutions*, **2011**, Solid State Commun., 151, 1686.

Chapter 7: $\text{Bi}_{0.825}\text{Nd}_{0.175}\text{Fe}_{0.97}\text{Ti}_{0.03}\text{O}_3$ thin films: a preliminary investigation

7.1. Introduction

BiFeO_3 (BFO) has recently attracted enormous interest due to the co-existence of ferroelectricity and antiferromagnetism above room temperature. BiFeO_3 [1-3] has the perovskite structure with a rhombohedral distortion along the [111] direction. Since its ferroelectric properties arise from Bi 6s lone pair electrons [4], chemical modification of the A-site in the perovskite structure is expected to affect the (anti)ferroelectric properties. An important consequence of the RE substitution is a phase transition from the rhombohedral FE phase of the parent compound into a PZ-like AFE structure [5, 6].

Although BiFeO_3 has been recognized as a probable environmentally friendly alternative to current Pb-based piezoelectrics, it suffers from high leakage current, large coercive fields and electrochemical coefficients much smaller than Pb-based compositions [7]. However, A and B site doping of BiFeO_3 has been shown to improve leakage resistance [5, 8] and the electrochemical response [9-11].

Chapter 5 of this thesis focused on Ti-doping to increase the resistivity of RE-doped BFO ceramics. Although large fields were applied to the ceramics, switching either between FE states or from AFE-FE was not attained and invariably samples broke down before the nominal coercive field was achieved. However, it is well known that high quality thin films have orders of magnitude greater breakdown strength than the equivalent ceramic. Hence, thin films of $\text{Bi}_{0.825}\text{Nd}_{0.175}\text{Fe}_{0.97}\text{Ti}_{0.03}\text{O}_3$, which in bulk ceramic has the PZ-like structure (Chapter 6, Figure 1), were deposited by Pulsed Laser

Deposition (PLD) on Pt/Si substrates in collaboration with the group of Professor Troler-Mckinstry at Pennsylvania State University, PA, USA.

7.2. Pulsed Laser Deposition (PLD)

PLD is a thin film deposition technique where a high power pulsed laser beam is focused inside a vacuum chamber to strike a target of the material that is to be deposited, Figure 7.1. This material is vaporized from the target creating a plasma plume which subsequently deposits as a thin film on the substrate. This process normally occurs in ultra high vacuum but may be carried out in the presence of a background gas, such as oxygen or in this case ozone/oxygen (O_3/O_2), which is commonly used to minimise V_O in deposited oxide films.

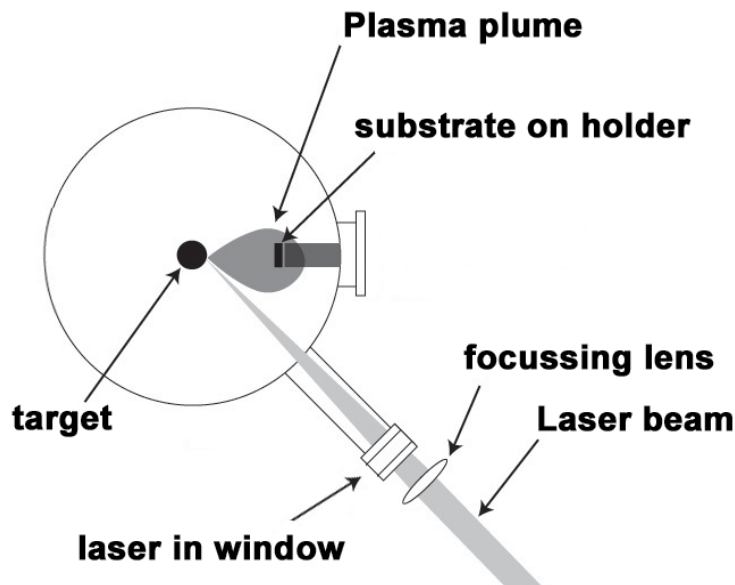


Figure 7.1: Schematic of the configuration of a typical PLD chamber.

Despite the relatively simple basic set-up compared with many other deposition techniques, the physical phenomena of laser-target interaction and film growth are quite complex. After the laser pulse is absorbed by the target, energy is first converted to

electronic excitation and then into thermal, chemical and mechanical energy resulting in evaporation, ablation, plasma formation and even exfoliation [12]. The ejected species expand into the surrounding vacuum in the form of a plume containing many energetic species before depositing on the substrate.

The nucleation process and growth kinetics of the film depend on several factors. The laser fluence [J/cm^2], laser energy, and ionization degree of the ablated material will affect the film quality, the stoichiometry [13], and the deposition flux. The nucleation density increases when the deposition flux and substrate surface temperature are enhanced [14]. Nucleation and growth are also affected by surface preparation such as chemical etching [15] and the roughness and film quality is critically improved if O stoichiometry is maintained by the use of a background gas such as O_3/O_2 [16-18].

$\text{Bi}_{0.825}\text{Nd}_{0.175}\text{Fe}_{0.97}\text{Ti}_{0.03}\text{O}_3$ was deposited on Pt/Si substrates using a 248 nm KrF excimer laser. Images of the experimental setup are shown in Figure 7.2. The specific processing conditions are summarized in Table 7.1. To reduce non-uniform erosion as well as droplet formation, targets were rotated during the ablation process. Elevated growth temperatures up to 750 °C were achieved by attaching the substrates, with silver paint, to a stainless steel block-style heater placed opposite and parallel to the target. Before each experiment, the substrates were cleaned ultrasonically using Micro Lab Solvent, deionized water, acetone and ethanol. Film depositions were performed in a dynamic 100 – 400 mTorr pressure of a mixture of 10% O_3 - 90% O_2 , the 10% O_3 atmosphere referring to the undistilled output of a commercially available ozone generator.

Table 7.1: Parameters of pulsed laser deposition.

Parameters	
Temperature (°C)	370-750
Atmosphere	10% O ₃ –90% O ₂
Pressure (mTorr)	75
Laser power (mJ)	250
Laser fluence (J/cm ²)	2.5
Laser frequency (Hz)	10
Target	3% Ti-doped Bi _{0.825} Nd _{0.175} FeO ₃
Target to substrate distance (cm)	5

O₃/O₂ was utilised to help stabilize the desired perovskite phase but it has also been reported that an oxidizing atmosphere allows better control of Pb and PbO_x compositions [19]. Here, it is suggested that O₃/O₂ reduces Bi volatilization. Immediately after deposition, the samples were cooled, under the same pressure and in the same O₃/O₂ mix until 400 °C to avoid any additional annealing step.

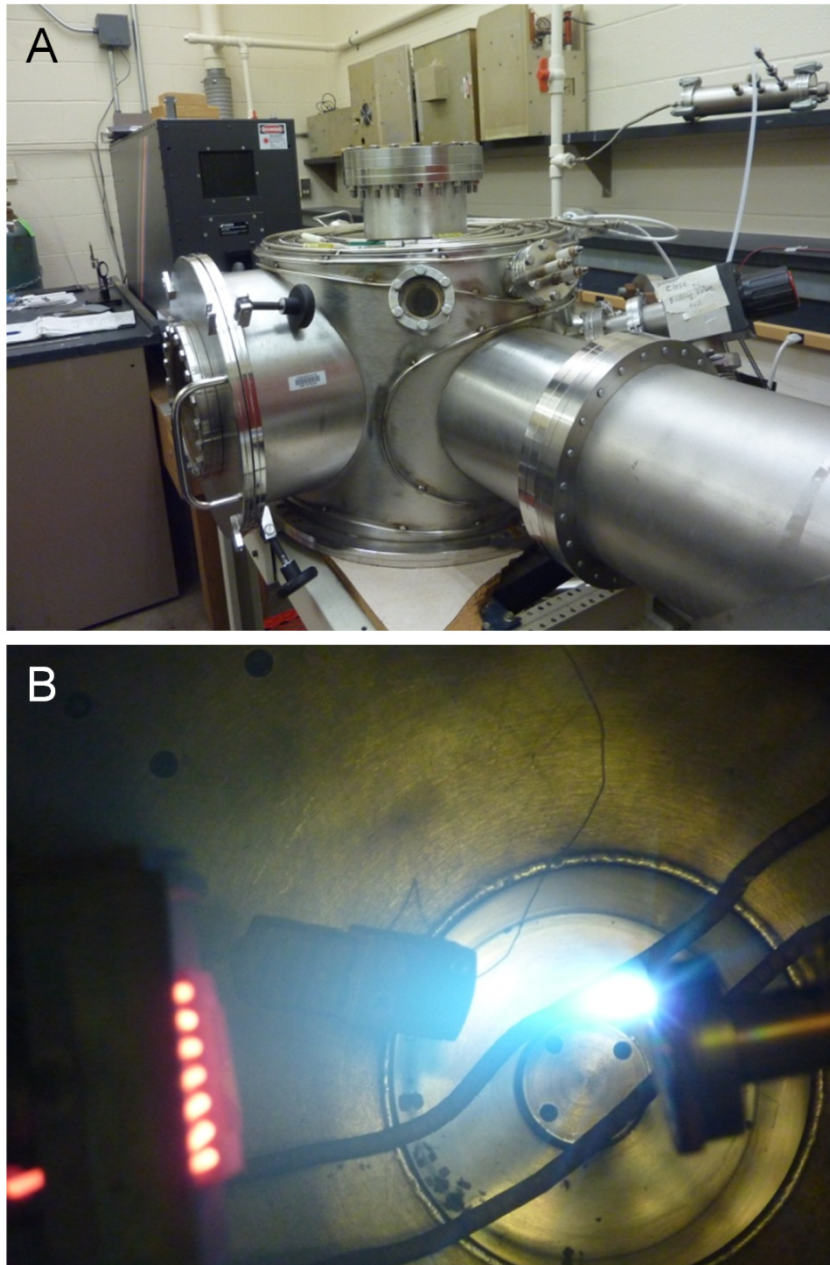


Figure 7.2: A) Pulsed Laser Deposition chamber, Pennsylvania State University, PA, US. B) Collision of laser beam on to target ceramic inside the PLD chamber. The substrate can be seen on the elements (the red area).

7.3. X-Ray Diffraction (XRD)

Thin films deposited with substrate temperature ≤ 550 °C did not exhibit the perovskite pattern in XRD but all peaks from films deposited on substrate heated at 625 and 650 °C could be indexed according to a fundamental perovskite lattice, with a preferred (001) orientation, Figure 7.3. In addition to perovskite, two strong peaks corresponding to Pt(111) and Si(400) at $2\theta = 40^\circ$ and 70° , respectively, were also observed. In Figure 7.3, the bulk target XRD trace is included which has the PZ-like structure, first described by Karimi *et al.* [5]. As discussed in Chapters 5 and 6, there are unique reflections associated with the PZ-like phase at, e.g., ~ 18 and $28^\circ 2\theta$. These reflections are absent in the thin film XRD trace, moreover much of the characteristic splitting of peaks which also denotes the PZ-like cell is not observed.

The absence of conclusive weak reflections and peak splitting in XRD traces from thin films of distorted perovskites is not unusual and is normally attributed to a combination of preferred orientation, substrate clamping effects and weak intensity from the thin layer (225 nm). However, it is important to ascertain the structure of the film utilising a non-destructive technique, specifically, whether the film is ferroelectric (R3c), antiferroelectric (Pbam) or paraelectric (Pnma). Karimi *et al.* [5] reported that these symmetries may be readily distinguished using Raman spectroscopy and illustrated the key modes and bands associated with each phase. Similar data has been presented in Chapter 6. Provided that the film is ≥ 200 nm thick, it is possible to distinguish the symmetry of different phases in thin films grown on opaque substrates such as Pt/Si [20].

7.4. Raman Spectroscopy

Room temperature Raman spectra of thin films as a function of substrate temperature are shown in Figure 7.4. The spectra were corrected for the Bose–Einstein temperature factor and evaluated in a comparative manner. Thin films with substrate

temperatures of 625 and 650 °C exhibited broadly similar Raman modes to the target material and hence were considered to have predominantly the PZ-like structure. However, higher substrate temperatures exhibited sharp modes that could not be assigned to any of the expected perovskite phases and which to date remain unidentified.

Raman spectra from thin films deposited at 625°C are compared in greater detail and clarity to bulk spectra from the PZ-like and ferroelectric R3c phases, derived from $\text{Bi}_{0.825}\text{Nd}_{0.175}\text{Fe}_{0.97}\text{Ti}_{0.03}\text{O}_3$ and $\text{Bi}_{0.9}\text{Nd}_{0.1}\text{Fe}_{0.97}\text{Ti}_{0.03}\text{O}_3$ bulk samples, respectively, Figure 7.5. As commented above, most film modes correspond to the AFE PZ-like structure but some are best described as arising from the ferroelectric R3c structure. For example, the thin film mode at 400 cm^{-1} is present in the PZ-like bulk spectrum while the sharper mode at 150 cm^{-1} exists only in R3c. It is concluded therefore that the thin film deposited at 625 °C (and 650 °C) is predominantly PZ-like but contains regions composed of the R3c phase. Further TEM analysis is required to assess whether the R3c phase is homogeneously distributed through the film thickness in an inter- or intra-granular manner or whether it is confined to the film surface or film electrode interface.

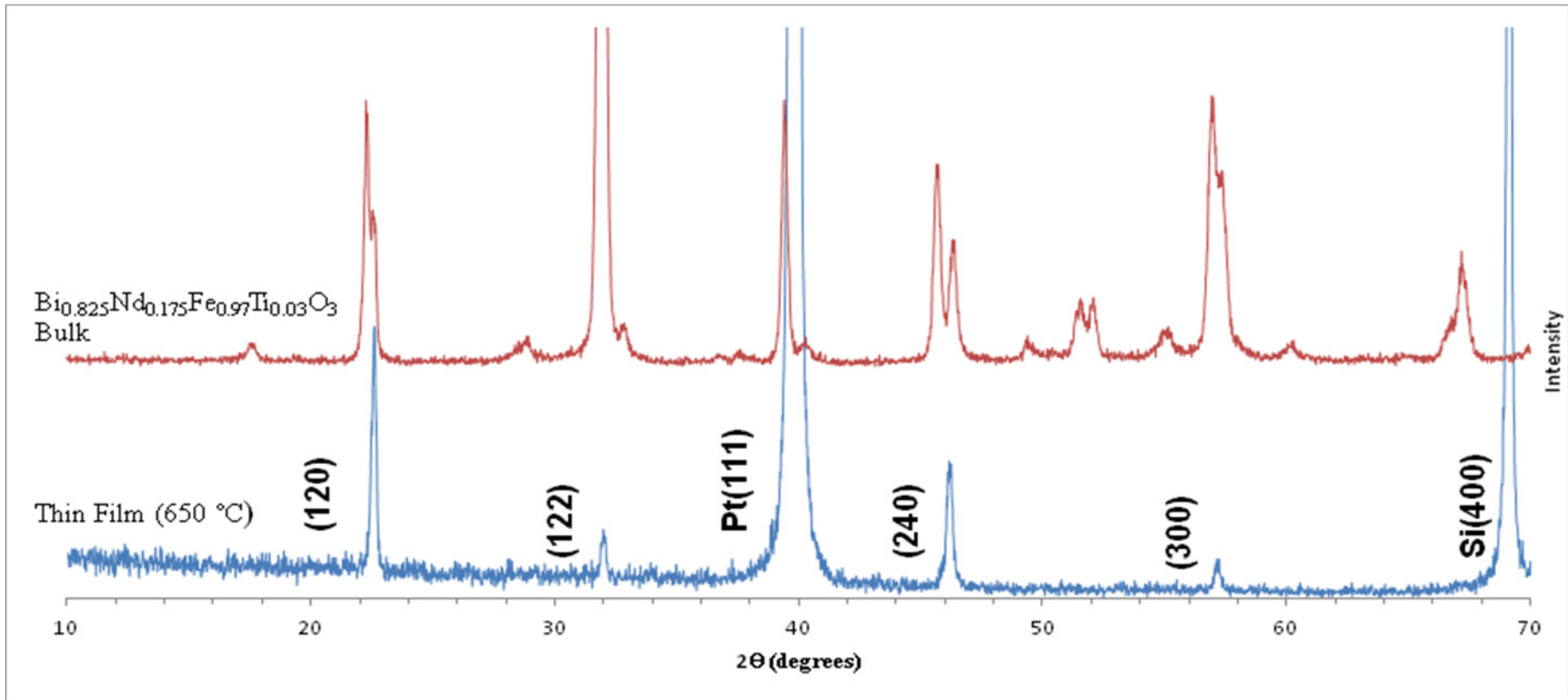


Figure 7.3: Comparison between XRD patterns of target ceramic and typical traces from thin films deposited at 625°C and 650°C (only one shown here since they are identical).

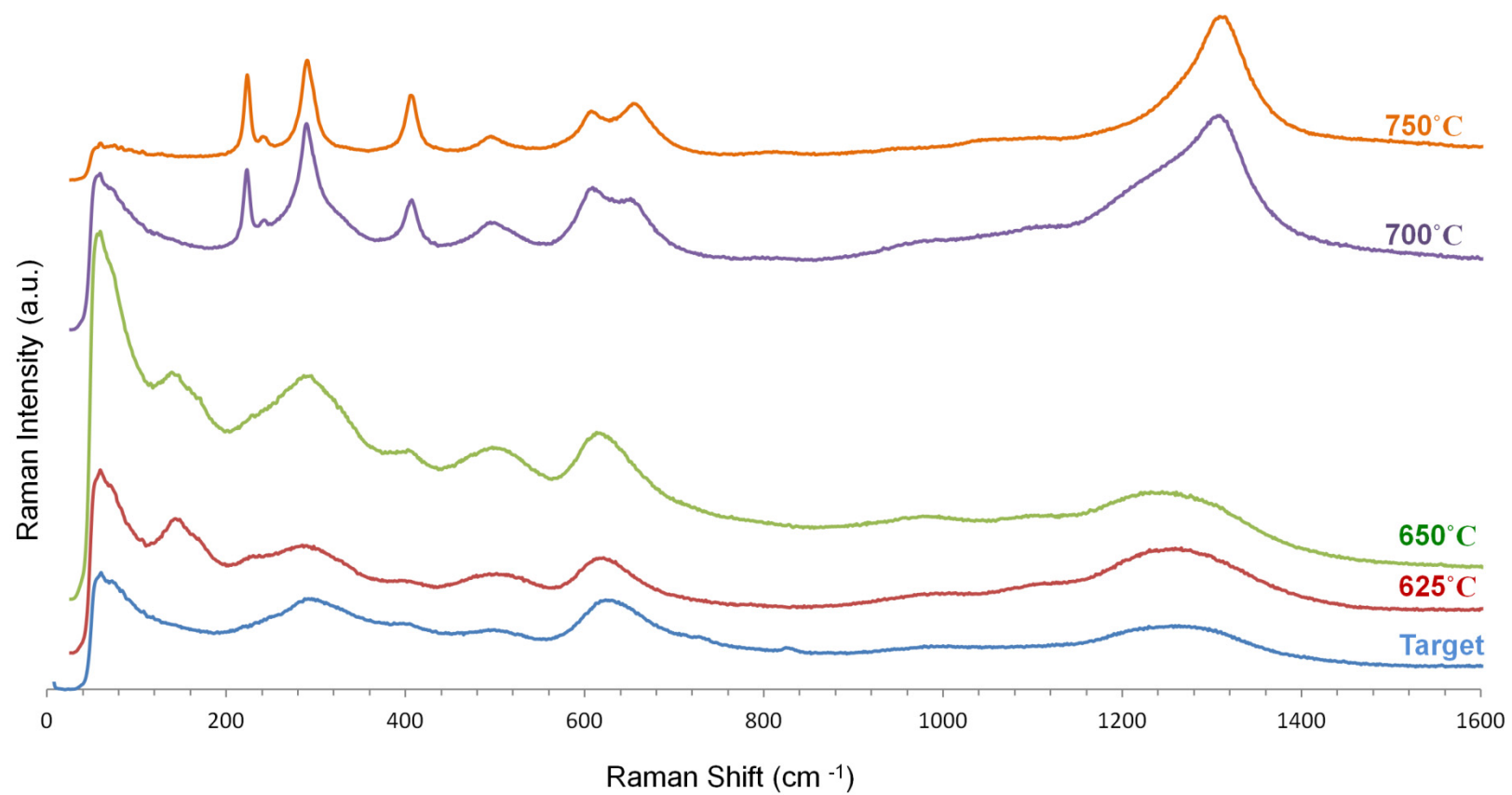


Figure 7.4: Raman spectra of target ceramic compared to thin films with substrate temperatures from 625 °C to 750 °C.

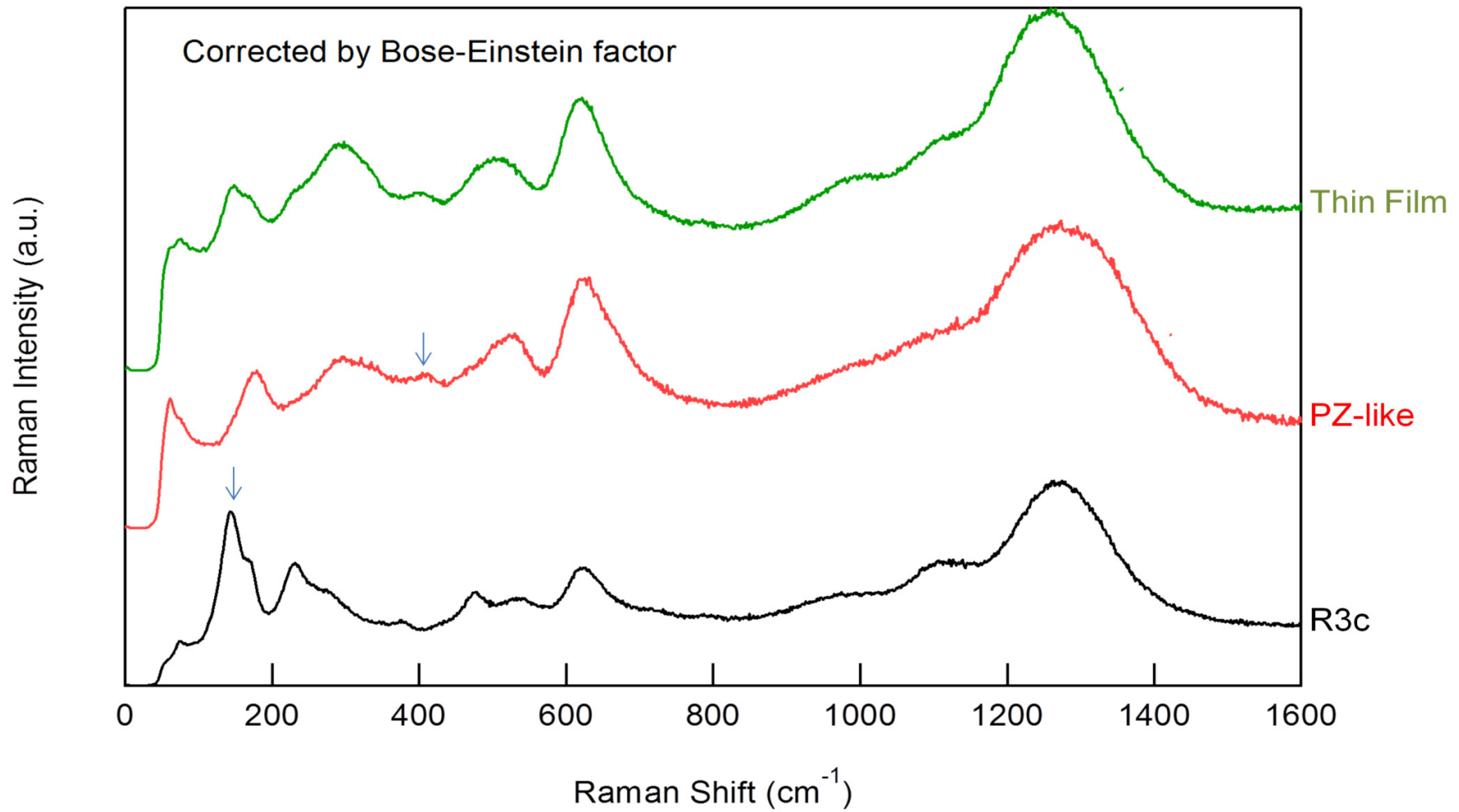


Figure 7.5: Raman spectrum of fabricated thin film compared to typical spectra of PZ-like and R3c structures. The blue arrows indicate modes present only in one structure.

7.5. Scanning Electron Microscopy (SEM)

Figure 7.6 shows a secondary electron image of the surface of a thin film deposited at a substrate temperature of 625 °C. Similar images were obtained for higher temperature depositions. The morphology and grain size ($< 0.2 \mu\text{m}$) was the same over the entire film surface with no obvious secondary phases in backscattered images.

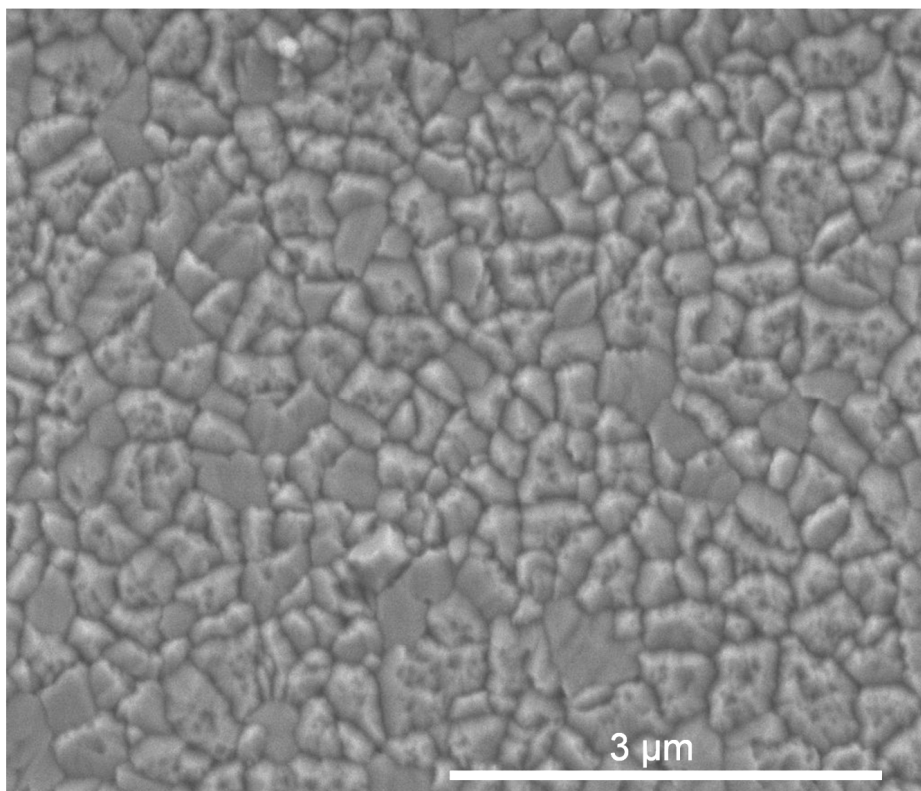


Figure 7.6: SEM image of a thin film deposited with a substrate temperature of 625° C.

7.6. Piezoresponse Force Microscopy

The intent of this study in the context of the thesis was not to undertake an extensive PFM analysis of the films but rather demonstrate that these films exhibited a piezoelectric response. Such a response may arise from either the intrinsically piezoelectric FE regions or via switching from an AFE to a FE state. Figure 7.7 reveals the PFM images of films deposited at a substrate temperature of 625°C. A DC bias (46 V) was applied to a $1\ \mu\text{m} \times 1\ \mu\text{m}$ square in the middle of the area scanned by PFM and revealed a change in contrast attributed to a piezoresponse. Similar data were obtained from films deposited with a substrate temperature of 650 °C. It should be noted that with time the contrast decreased in intensity which is attributed to leakage currents within the sample.

Although thin films showed some contrast after application of a bias voltage, the effect was not strong and at this stage it is inconclusive whether any AFE-FE switching has been induced. More likely, only the FE regions are responding to the bias field giving a local piezoresponse commensurate with the low volume fraction of R3c phase present in the films.

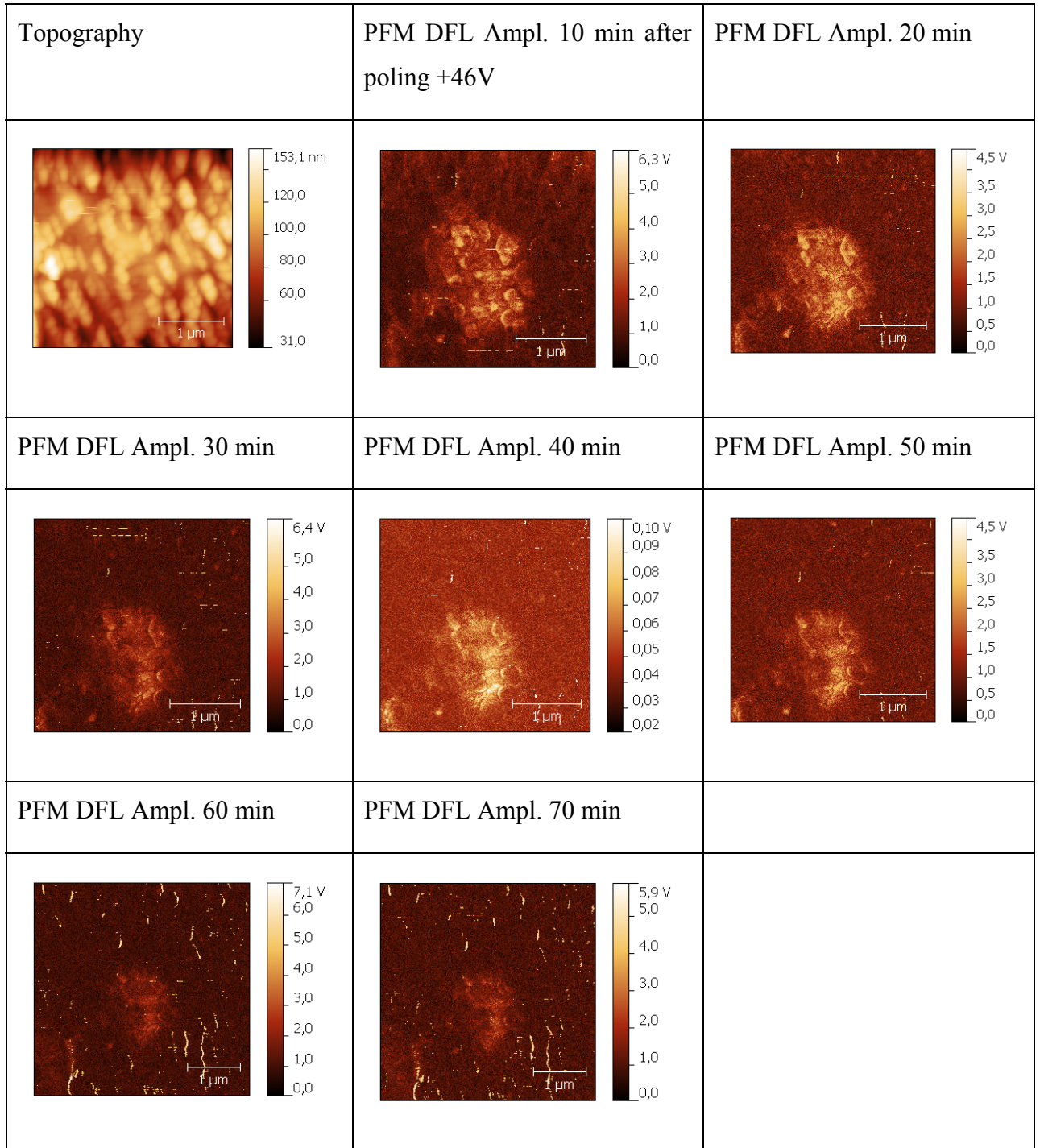


Figure 7.7: Preliminary PFM results of thin films.

7.7. Ferroelectric Characterisation

In this section, preliminary studies are presented on the switching characteristics of $\text{Bi}_{0.825}\text{Nd}_{0.175}\text{Fe}_{1-x}\text{Ti}_x\text{O}_3$. Figure 7.8 compares the polarisation vs. electric field loops obtained from samples grown at substrate temperatures of 625 and 650°C. Well below the coercive field (< 100 kV/cm), there is a linear dependence of polarisation with field, similar to that obtained for PZ ceramics under equivalent experimental conditions [21]. As the field increases to ~ 200 kV/cm, the polarisation loops show evidence of opening up accompanied by an increase in the gradient (dP/dE). Above ~ 400 kV/cm, a square hysteresis loop is obtained which shows evidence of a contribution from space-charge as well as dipole polarisation reversal. Contributions from space-charge reversal are characterised by broadening of the tips of the hysteresis curve and $P_{\text{max}} > P_{\text{sat}}$. Despite the space-charge contribution to the total polarisation reversal, there is clear evidence of dipolar switching behaviour. Given the relatively low volume fraction of FE phase in these samples, the dominance of the PZ-like structure and the huge coercive field (400 kV/cm), it is speculated that the large nominal remanent polarisation ($100 \mu\text{C}/\text{cm}^2$ for 650 °C substrate temperature) arises at least in some part from AFE-FE switching as well that between equivalent FE states. However, considerably more work is required to prove conclusively whether or not this is the case. Moreover, the piezoresponse from PFM measurements does not indicate any large local scale switching from AFE-FE but rather weak contrast that could easily arise from the piezoresponse associated with the FE phase.

It is difficult to compare these loops to any that are illustrated in the literature. Double hysteresis loops are often quoted as indisputable evidence of AFE behaviour but such loops are rarely seen in the context of PZ ceramics which break down at < 200 kV/cm [21]. Ironically, double loops are most frequently observed for acceptor doped ferroelectrics or induced in the PE phase above a 1st order FE transition [22]. Consequently, it is difficult to interpret the behaviour of the above films by comparison with other systems.

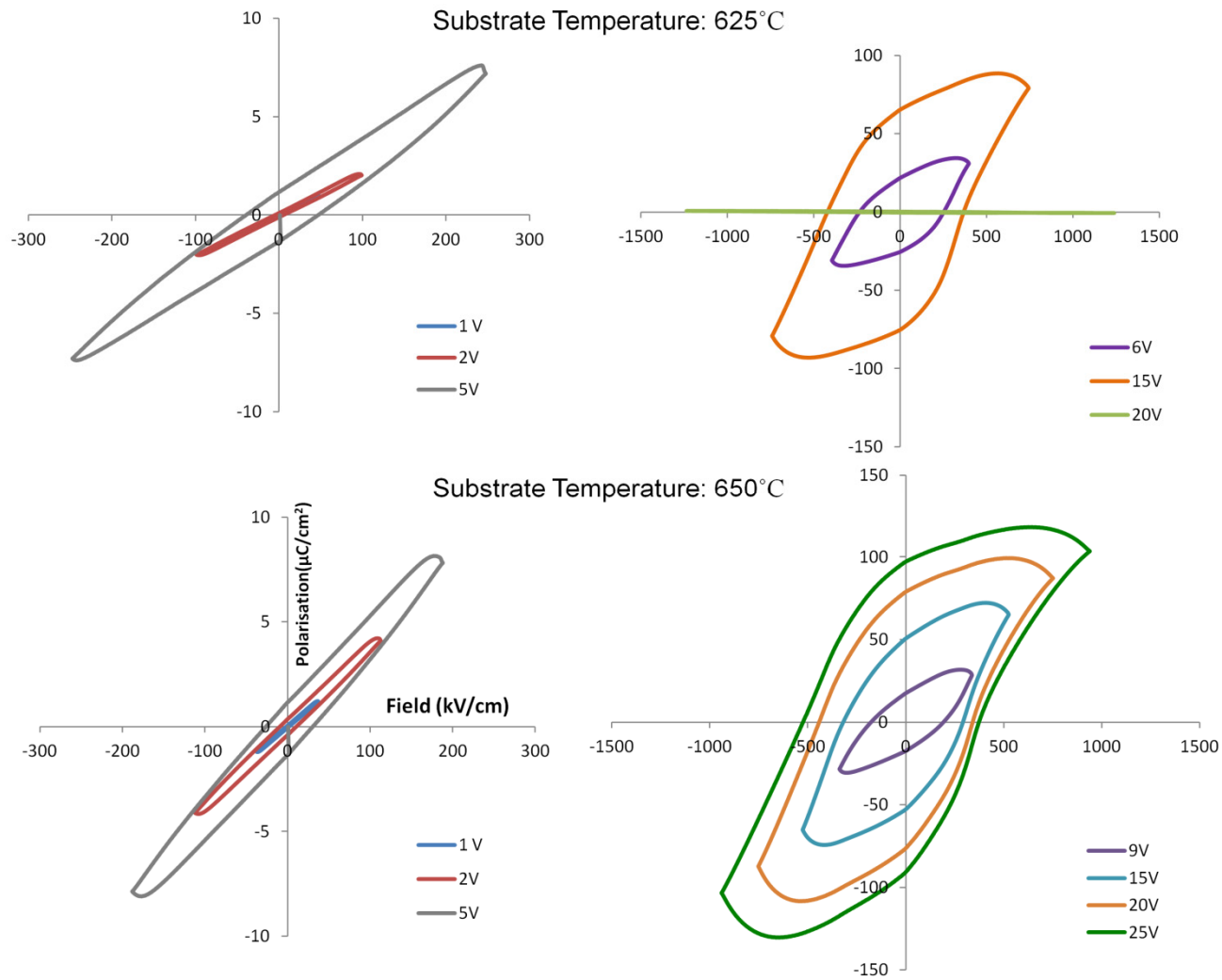


Figure 7.8: Polarisation vs. electric field measurements of $\text{Bi}_{0.825}\text{Nd}_{0.175}\text{Fe}_{0.97}\text{Ti}_{0.03}\text{O}_3$ thin films.

7.8. Conclusions

Polycrystalline $\text{Bi}_{0.825}\text{Nd}_{0.175}\text{Fe}_{0.97}\text{Ti}_{0.03}\text{O}_3$ films were fabricated by pulsed laser deposition. The target had the PZ-like AFE structure but Raman spectroscopy, revealed that films grown at substrate temperatures of 625°C and 650°C had a mixture of PZ-like and R3c phases. SEM did not reveal any secondary phases and the morphology of the sample was constant on the entire surface of the film.

PFM measurements revealed a weak piezoresponse best explained as arising from an FE phase, identified in minor concentration using Raman spectroscopy. However, the very large coercive field and high remanent polarisation obtained from polarisation-field measurements could indicate at least in part AFE-FE switching in the system. These preliminary findings are significant enough to warrant further study since, AFE-FE switching in PbO-free ceramics could have commercial potential in actuators.

References

1. J. Wang, J.B. Neaton, H. Zheng, V. Nagarajan, S. B. Ogale, B. Liu, D. Viehland, V. Vaithyanathan, D.G. Scholm, U.V. Waghmare, N.A. Spaldin, K.M. Rabe, M. Wuttig and R. Ramesh, *Epitaxial BiFeO₃ Multiferroic thin film heterostructures*, **2003**, Science, 299, 5613, 1719-1722.
2. G. Catalan, J. F. Scott, *Physics and Applications of Bismuth Ferrite*, **2009**, Adv. Mater., 21, 2463.
3. D. Lebeugle, D. Colson, A. Forget, M. Viret, *Thickness-dependent structural and magnetic properties of BiFeO₃ films prepared by metal organic decomposition method*, **2007**, Appl. Phys. Lett., 91, 022907.
4. P. Baettig, C.F. Schelle, R. Lesar, U.V. Waghmare, N.A. Spaldin, *First principles study of the multiferroics BiFeO₃ Bi₂FeCrO₆, and BiCrO₃: Structure, polarisation, and magnetic ordering temperature*, **2005**, Chem. Mater., 17, 1376.
5. S. Karimi, I. Reaney, Y. Han, J. Pokorny, and I. Sterianou, *Crystal chemistry and domain structure of rare-earth doped BiFeO₃ ceramics*, **2009**, J. Mater. Sci. 44, 5102.
6. D. Kan, L. Palova, V. Anbusathaiah, C.J. Cheng, S. Fujino, V. Nagarajan, K.M. Rabe, and I. Takeuchi, *Universal behaviour and electric-field-induced structural transition in rare-earth-substituted BiFeO₃*, **2010**, Adv. Funct. Mater., 20, 7, 1108-1115.
7. C.J. Cheng, D Kan, S.H. Lim, W.R. Mckenzie, P.R. Munroe, L.G. Salamanca-Riba, R.L. Withers, I. Takeuchi and V. Nagaraian, *Structural transitions and complex domain structures across a ferroelectric-to-antiferroelectric phase boundary in epitaxial Sm-doped BiFeO₃ thin films*, **2009**, Phys Rev. B., 80, 014109.

8. K. Kalantari, I. Sterianou, S. Karimi, M. C. Ferrarelli, S. Miao, D. C. Sinclair, and I. M. Reaney, *Ti Doping to reduce conductivity in $\text{Bi}_{0.85}\text{Nd}_{0.15}\text{FeO}_3$ ceramics*, **2011**, Adv. Funct. Mater. 21, 3737.
9. Y.H. Chu, Q. Zhan, C.H. Yang, M.P. Cruz, L.W. Martin, T. Zhao, P. Yu, R. Ramesh, P.T. Joseph, I.N. Lin, W. Tian and D.G. Scholm, *Low voltage performance of epitaxial BiFeO_3 films on Si substrates through lanthanum substitution*, **2008**, Appl. Phys. Lett., 92, 102909.
10. G.L. Yuan and S.W. Or, *Multiferroicity in polarized single-phase $\text{Bi}_{0.875}\text{Sm}_{0.125}\text{FeO}_3$ ceramics*, **2006**, J. Appl. Phys., 100, 024109.
11. H. Uchida, R. Ueno, H. Funakubo and S. Koda, *Crystal structure and ferroelectric properties of rare-earth substituted BiFeO_3 thin films*, **2006**, J. Appl. Phys., 100, 014106.
12. D.B. Chrisey, *Pulsed Laser Deposition of Thin Films*, **1994**, John Wiley & Sons
13. T. Ohnishi, K. Shibuya, T. Yamamoto, M. Lippmaa, *Defects and transport in complex oxide thin films*, **2008**, J. Appl. Phys., 103, 10, 103703.
14. J.D. Ferguson, G. Arikan, D.S. Dale, A.R. Woll and J.D. Brock, *Measurements of surface diffusivity and coarsening during pulsed laser deposition*, **2009**, Phys. Rev. Lett., 103, 25, 256103.
15. G. Koster, B.L. Kropman, G. Rijnders, A. Blank, H. Rogalla, *Quasi-ideal strontium titanate crystal surfaces through formation of strontium hydroxide*, **1998**, Appl. Phys. Lett., 73, 20, 2920.
16. A. Ohtomo, H.Y. Hwang, *Growth mode control of the free carrier density in $\text{SrTiO}_{3-\delta}$ films*, **2007**, J. Appl. Phys., 102, 8, 083704.
17. J.S Horwitz, D.B Chrisey, R.M Stroud, *Pulsed laser deposition as a materials research tool*, **1998**, App. Surf. Sci., 127, 507-513.
18. V. Bornard, S. Trolier-Mckinstry, *Phase development in pulsed laser deposited $\text{Pb}[\text{Yb}_{1/2}\text{Nb}_{1/2}]\text{O}_3\text{-PbTiO}_3$ thin films*, **2000**, Elsevier Science, 370, 70-77.

19. D.B Chrisey, G.K Hubler, *Pulsed laser deposition of thin films*, **1994**, Wiley, Newyork.
20. M. Mirsaneh, B.E. Hayden, S. Miao, J. Pokorny, S. Perini, E. Furman, M.T. Lanagan, R. Ubic, I.M. Reaney, *High throughput synthesis and characterization of $Pb_nNb_2O_5$ ($0.5 < n < 4.1$) system on a single chip*, **2011**, Acta Materialia, 59, (5), 2201-2209.
21. U. Sukkha, R. Muanghlua, S. Niemcharoen, B. Boonchoma and N. Vittayakorn, *Antiferroelectric-ferroelectric phase transition in lead zinc niobate modified lead zirconate ceramics: crystal studies, microstructure, thermal and electrical properties*, **2010**, Appl. Phys. A, 100, 551-559.
22. Q. Tan, J. Li and D. Viehland, *Role of lower valent substituent-oxygen vacancy complexes in polarization pinning in potassium-modified lead zirconate titanate*, 1999, App. Phys. Lett., 75, 418.

Chapter 8: Conclusions

The main objective of the project was to reduce the leakage current of RE-doped BFO-ceramics. It was postulated that the reduction of Fe^{3+} to Fe^{2+} accompanied by the formation of $\text{V}_\text{O}^{\cdot\cdot}$ was responsible for the high dielectric losses and large leakage currents measured in $\text{Bi}_{0.85}\text{Nd}_{0.15}\text{FeO}_3$. Consequently, a donor doping strategy was adopted in which Ti^{4+} substituted on the B-site according to the formula, $\text{Bi}_{0.85}\text{Nd}_{0.15}\text{Fe}_{1-y}\text{Ti}_y\text{O}_3$. No assumptions were made about ionic compensation mechanisms since they were not known at the start of the programme of research.

Raman spectroscopy and x-ray diffraction revealed that samples with $y = 0$ were a mixture of the R3c and PZ-like structures. Higher Ti (y) concentrations only revealed the presence of PZ-like phase. With substitution of 1% Ti for Fe, the bulk resistance increased sharply, as the activation energy for conduction (E_a) increased from ~ 0.3 to 1.1 eV, but remained relatively constant for higher concentrations. This demonstrates that Ti-doping was effective in suppressing the semi-conductivity associated with the mixed oxidation states of the Fe ions.

A non-linear relationship between T_C and Ti concentration was observed. The compensation mechanism for Ti-doping is still a matter of debate but one possibility is that for low concentrations (less than 3%), Ti^{4+} compensates for Fe^{2+} and eliminates the $\text{V}_\text{O}^{\cdot\cdot}$ present and is the origin of the large decrease in bulk conductivity. For higher Ti-doping levels, antipolar order is disrupted with the most probable compensation mechanism relating to the formation of $\text{V}_\text{Nd}^{\cdot\cdot\cdot}$.

Polarisation vs. electric field loops were attained for $\text{Bi}_{0.85}\text{Nd}_{0.15}\text{Fe}_{1-y}\text{Ti}_y\text{O}_3$ ($0 \leq y \leq 0.1$) samples. The high leakage current in undoped $\text{Bi}_{0.85}\text{Nd}_{0.15}\text{FeO}_3$ led to a malformed loop with no clear relationship between polarisation and field. In contrast, Ti-doped ceramics showed a linear dependence of polarisation with field, similar to that

obtained for PZ ceramics under equivalent experimental conditions. Large electric fields may be applied to these compounds but the absence of switching to a FE from the AFE state in the polarisation *vs.* field loops suggests the coercive field is high and to date bulk samples have broken down before a sufficiently large field could be applied.

The effect of 3% Ti-doping on the conductivity and phase assemblage of $\text{Bi}_{1-x}\text{Nd}_x\text{FeO}_3$ solid solution was also investigated. Samples with $x \leq 0.125$ were rhombohedral (R3c) FE, whereas compositions $0.15 \leq x \leq 0.2$ were best described by the antipolar PZ-like structure. Ceramics with $x = 0.25$, match well to the peak distribution and intensities for the paraelectric (PE) orthoferrite phase (Pnma). $x = 0.125$ ceramics revealed some weak reflections in XRD which are characteristic of the PZ phase (Pbam) that suggest the coexistence of R3c and Pbam, defining this composition as lying at the ferroelectric/antiferroelectric (FE/AFE) phase boundary.

Permittivity *vs.* temperature curves for Ti-doped $\text{Bi}_{1-x}\text{Nd}_x\text{FeO}_3$ samples at different frequencies revealed no peaks in $x = 0$ and 0.1 despite clear anomalies at 816°C and 520°C , respectively, in the DSC and dilatometry data, presumably due to the high level of conductivity at $> 500^\circ\text{C}$ despite Ti-doping. For samples with $x = 0.115$, a weak but sharp anomaly in permittivity is observed which is coincident with those in thermal analysis. For $x = 0.125$, a doublet peak is observed in the dielectric data at a temperature coincident with anomalies in the DSC and dilatometry traces. $x = 0.125$ remains mixed phase at ambient temperatures according to XRD and Raman data, implying that the FE phase does not transform directly to AFE. Consequently, the two anomalies for $x = 0.125$ are most likely PE-FE and PE-AFE transitions occurring in different regions of the sample. For samples with $0.15 \leq x \leq 0.2$ (Pbam, AFE), a step-like change in permittivity is observed, coincident in temperature with anomalies in DSC and dilatometry curves. Small impurity and defect concentrations result in a PE-FE transformation in PZ prior to a step-like dielectric anomaly to the AFE phase; therefore it is impossible to draw a direct comparison between RE-doped BiFeO_3 and pure PZ. Intuitively however, the transition from a non-polar PE to an antipolar AFE state would not be expected to give rise to a large peak in permittivity. For $x = 0.25$, the transition is potentially sub-ambient and could not be observed in any equipment utilised in this study.

Polycrystalline $\text{Bi}_{0.825}\text{Nd}_{0.175}\text{Fe}_{0.97}\text{Ti}_{0.03}\text{O}_3$ thin films deposited at 625 and 650 °C on Pt/Si substrate were predominantly PZ-like but contained regions composed of the R3c phase. After application of a bias voltage (46 V) in PFM studies, thin films showed some contrast related to a piezoresponse but since the effect was relatively weak it was considered most likely that only the low volume fraction of FE regions was responding to the bias field. The polarisation-field loops from thin films were initially linear at < 100 kV/cm but showed evidence of opening up accompanied by an increase in the gradient (dP/dE) as the field increased to ~200 kV/cm. Above ~400 kV/cm, an unsaturated hysteresis loop was obtained which showed evidence of a contribution from space-charge as well as dipole polarisation reversal. There is clear evidence of dipolar switching behaviour; although, space-charge clearly contributes to the P_{max} . The dominance of the PZ-like structure in addition to the huge coercive field (400 kV/cm) suggests that the large nominal remanent polarisation ($100 \mu\text{C}/\text{cm}^2$ for 650 °C substrate temperature) arises at least in some part from AFE-FE switching.

Overall, the project has achieved considerable success in improving and understanding structural phase transitions, phase assemblages and to a lesser degree the defect chemistry in RE-doped BiFeO_3 . The strategies adopted should in the long term lead to functional ceramics that could be commercially exploited.

Chapter 9: Future Work

The results obtained in this study of the Ti doped $\text{Bi}_{1-x}\text{Nd}_x\text{FeO}_3$ system revealed new avenues of potential research which could not be addressed due to time constraints.

Ti-doping reduced the leakage current which allowed the AFE/PE phase transition to be observed in dielectric as well as DSC measurements. Large fields may now be applied to these ceramics but to date AFE/FE switching has not been observed. Comparison with undoped PZ indicates that the coercive field for AFE/FE switching is at least 100-200 kV/cm and ceramics invariably breakdown before the coercive field is attained. Heavily doping PZ with e.g. Sn, Nb or La has been reported to reduce the free energy difference between the FE and AFE phases by creating an incommensurate mixed FE/AFE structure [1] A similar approach may be adopted for RE-doped BFO and incommensurate modulations of the AFE structure have already been reported by some authors [2].

The source of conductivity in BFO based ceramics is a point of controversy. It is proposed that the large permittivity and $\tan \delta$ of undoped $\text{Bi}_{1-x}\text{Nd}_x\text{FeO}_3$ ceramics arise from oxygen loss that results in the formation of $\text{V}_\text{O}^\bullet$ and reduction of Fe^{3+} ions to Fe^{2+} ions, according to the formula $\text{Bi}(\text{Fe}^{3+}_{1-x}\text{Fe}^{2+}_x)\text{O}_{3-x/2}$. This premise is supported by strong reduction in conductivity due to B-site donor doping. Extensive atmosphere impedance spectroscopy is underway to recognise both the source of high leakage current and doping compensation mechanisms in BFO based ceramics. In atmosphere impedance spectroscopy samples would be measured under oxidising and reducing atmospheres, consequently the change in resistivity will be measured and compared. These studies were not completed at the time of writing but will be finished shortly and it is hoped that they will shed light on the defect chemistry and compensation mechanisms in RE-doped BFO.

The dielectric relaxation in the vicinity of the T_N in BiFeO₃-based materials has been mostly attributed either to coupling of the orientation of the magnetization to the ferroelastic strain [3] or Maxwell-Wagner behaviour arising from space charge polarization [4]. The strong dielectric relaxation was analysed by Park *et al.* [5] for Bi₂Fe₄O₉ single crystals and discussed in terms of a Maxwell-Wagner relaxation, with the authors noting that it is peculiar why such behaviour would be observed only in a particular crystal direction. Considering that explanations presented above are applicable here, the polycrystalline nature of the samples does not allow us to distinguish between contributions from different crystallographic directions. Further study is essential in this field to understand the exact physical phenomena that generate dielectric relaxation in the vicinity of the T_N . Most importantly however, this relaxation must be eradicated or pushed to higher temperature as the dielectric loss in its vicinity rises to 20% which will prevent all high field piezoelectric applications.

Due to the limited time available for the collaboration with the group of Professor Susan Mckinstry at Pennsylvania State University, USA, conditions of pulsed laser deposition were only partially optimised to obtain preliminary results. Despite the limited time in the US, the results were extremely promising with switching behaviour demonstrated albeit unclear as to whether this is between FE states or AFE-FE. There is considerable margin to refine the deposition conditions and improve film quality. In particular, thicker films (400 nm) could lead to higher breakdown strength and fewer shorts and potentially more saturated field *vs.* polarization hysteresis loops.

At substrate deposition temperatures, 625 and 650 °C, Raman spectroscopy revealed FE as well as AFE regions in the thin films. The location of the FE regions however, is unknown as is their origin. FE is stabilised for compositions with < 14% Nd. This suggests that either there are Bi-rich perovskite regions in which Nd is < 14% or that local stress states have altered the phase assemblage. For future work therefore, it is important to know the composition and location of the FE phase within the film, *i.e.* inter-or intra-granular, at the film surface or at the film electrode interface. TEM is the only technique capable of resolving the composition and location of the FE phase but preparation in cross section of samples of the required quality is difficult and only feasible within the confines of a dedicated TEM study. Such a study is underway and

the results will be utilised in a forthcoming paper, which is in preparation, on the thin film studies performed at PSU.

References

1. D. Viehland, D. Forst and J.F. Li, *Compositional heterogeneity and the origins of the multicell cubic state in Sn-doped lead zirconate titanate ceramics*, **1994**, J. Appl. Phys., 75, 4137.
2. C.J. Cheng, D. Kan, S.H. Kan, S.H. Lim, W.R. Mckenzie, P.R. Munroe, L.G. Salamamanca, R.L. Withers, I. Takeuchi and V. Nagarajan, *Structural transitions and complex domain structures across a ferroelectric-to-antiferroelectric phase boundary in epitaxial Sm-doped BiFeO₃ thin films*, **2009**, Phys. Rev. B., 80, 014109.
3. Z. X. Cheng, A. H. Li, X. L. Wang, S. X. Dou, K. Ozawa, H. Kimura, S. J. Zhang, and T. R. ShROUT, *Enhancement of ferroelectricity and ferromagnetism in rare earth element doped BiFeO₃*, **2008**, J. Appl. Phys. 103, 07E507.
4. V. Goian, S. Kamba, S. Greicius, D. Nuzhnyy, S. Karimi, and I. M. Reaney, *Terahertz and infrared studies of antiferroelectric phase transition in multiferroic Bi_{0.85}Nd_{0.15}FeO₃*, **2011**, J. Appl. Phys. 110, 074112.
5. A. Park, K. M. Song, K. D. Lee, C. J. Won, and N. Hur, *Effect of antiferromagnetic order on the dielectric properties of Bi₂Fe₄O₉*, **2010**, Appl. Phys. Lett. 96, 092506.